UNIVERSITAT DE BARCELONA

Novel markers and targets of collective tumor cell invasion before and after anti-angiogenic therapies

Júlia Sallaberry Pinto

UNIVERSITAT DE BARCELONA

UNIVERSITAT DE BARCELONA

FACULTAT DE FARMÀCIA I CIÈNCIES DE L'ALIMENTACIÓ

PROGRAMA DE DOCTORAT EN BIOMEDICINA

NOVEL MARKERS AND TARGETS OF COLLECTIVE TUMOR CELL INVASION BEFORE AND AFTER ANTI-ANGIOGENIC THERAPIES

JÚLIA SALLABERRY PINTO

2019

UNIVERSITAT DE BARCELONA

FACULTAT DE FARMÀCIA I CIÈNCIES DE L'ALIMENTACIÓ

PROGRAMA DE DOCTORAT EN BIOMEDICINA

NOVEL MARKERS AND TARGETS OF COLLECTIVE TUMOR CELL INVASION BEFORE AND AFTER ANTI-ANGIOGENIC THERAPIES

JÚLIA SALLABERRY PINTO

2019

Memòria presentada per Júlia Sallaberry Pinto

per optar al grau de Doctora per la Universitat de Barcelona

Dr. Oriol Casanovas Casanovas	Dr. Francesc Vinyals Canals	Júlia Sallaberry Pinto
Director	Tutor	Autora

TABLE OF CONTENTS

LIST OF ABBREVIATIONS

µg	Microgram
µl	Microliter
µm	Micrometer
µM	Micromolar
2,5D	Two and half-dimensional
2D	Two-dimensional
3D	Three-dimensional
aa	Aminoacids
AAALAC	Association for Assessment and Accreditation Laboratory Animal Care
AJCC	American Joint Committee on Cancer
AMT	Amoeboid-mesenchymal migration
APS	Ammonium persulfate
BCA	Bicinchoninic acid
BM	Basement membrane
B-NHL	B-cell non-Hodgkin lymphoma
BSA	Bovine serum albumin
CDH1	E-cadherin
cDNA	Complementary DNA
c-KIT	stem cell factor receptor
CLDN1	Claudin-1
CLDN10	Claudin-10
CLDN11	Claudin-11
CLDN14	Claudin-14
CLDN18	Claudin-18
CLDN19	Claudin-19
CLDN2	Claudin-2
CLDN3	Claudin-3
CLDN4	Claudin-4
CLDN5	Claudin-5
CLDN6	Claudin-6
CLDN7	Claudin-7
CLDN8	Claudin-8
CLDN9	Claudin-9

cm	Centimeter
CO2	Carbon dioxide
Const	Constitutive
CPE	Clostridium perfringens enterotoxin
Cpm	Counts per million
CRC	Colorectal cancer
CSF-1	Type I receptor of colony stimulating factor
CSIC	Consell Superior d'Investigacions Científiques
Ct	Threshold cycle
CTNNB1	Catenin beta 1
DAB	3,3'-Diaminobenzidine
DAB	3,3'-Diaminobenzidine
DAPI	4',6-Diamidino-2-phenylindole dihydrochloride
DAPI	4',6-Diamidino-2-phenylindole dihydrochloride
DC101	Anti-VEGFR2 monoclonal antibody
ddH2O	Bi-distilled water
ddH2O	Bi-distilled water
ddNTP	2',3' dideoxynucleotides
ddNTP	2',3' dideoxynucleotides
dH2O	Distilled water
dH2O	Distilled water
DMEM	Dulbecco’s Modified Eagle’s Medium
DMEM	Dulbecco’s Modified Eagle’s Medium
DMSO	Dimethyl sulfoxide
DMSO	Dimethyl sulfoxide
DNA	Deoxyribonucleic acid
DNA	Deoxyribonucleic acid
DPX	Distyrene, plasticiser and xylene
DPX	Distyrene, plasticiser and xylene
ECL1	Extracellular loop 1
ECL2	Extracellular loop 2
ECM	Extracellular matrix
EDTA	Ethylenediaminetetraacetic acid
EGF	Epidermal growth factor (EGF),
EMT	Epithelial-mesenchymal transition

EMT	Epithelial-mesenquimal transition
EMT-TFs	Including inducing transcription factors (EMT-TFs)
ES	Enrichment Score
ESCRT	Endosomal Sorting Complex Required for Transport
FBS	Fetal bovine serum
FC	Fold change
FDA	Food and Drug Administration
FDR	Fold discovery rate
FGF	hepatocyte growth factor (HGF), fibroblast growth factor (FGF)
Fn1	Fibronectin
FTL3	(Fms-like tyrosine kinase 3)
GFP	Guanosine triphosphate
GSEA	Gene Set Enrichment Analysis
h	Hour
H&E	Hematoxylin and eosin
H2O2	Hydrogen peroxide
HCC	Hepatocellular Carcinoma
HCl	Chloridric acid
HEPES	4-(2-hydroxyethyl)-1-piperazineethanesulfonic acid
HIF	Hypoxia-inducible Factor
IC2	Invasive carcinoma type 1
IC2	Invasive carcinoma type 2
ICO	Institut Català d'Oncologia
IDIBELL	Institut d'Investigació Biomèdica de Bellvitge
IGF	Insulin growth factor (IGF)
IL-1β	Interleukin-1β
ISREC	Swiss Institute for Experimental Cancer Research
ISREC	Swiss Institute for Experimental Cancer Research
IT	Islet tumors
Itga5	Integrin Subunit Alpha 5
Kb	Kilobase
KDa	Kilodalton
Kg	Kilogram
L	Litre
LN	Lymph node

MAT	Mesenchymal-ameboid transition
MET	Mesenchymal–epithelial transition
mg	Milligram
min	Minute
miRNA	Micro ribonucleic acid
ml	Milliliter
mm	Millimeter
mM	Millimolar
mm2	Square millimeter
mm3	Cubic millimeter
MMP	Matrix metalloprotease
MolSigDB	Molecular Signatures DataBase
mRNA	Messenger ribonucleic acid
MVB	Mutivesicular bodies
Na2HPO4	Monosodium phosphate
NaCl	Sodium chloride
NCDB	National Cancer Data Base
NETs	Neuroendocrine tumors
ng	Nanogram
NIS	National Inpatient Sample
NK	Natural killer
nm	Nanometer
Non-met	Non-metastatic
O/N	Over night
OCT	Optimum Cutting Temperature compound
PAGE	Polyacrylamide gel electrophoresis
PanNETs	Pancreatic neuroendocrine tumors
PBS	Phosphate buffered saline
PCR	Polymerase chain reaction
PDGF	Platelet-derived growth factor (PDGF)
PDOX	Patient-derived orthoxenograft
PDX	Patient-derived xenograft
PEBC	Programa d'Epigenètica i Biologia del Càncer
PEI	Polyethylenimine
PES	Polyethersulfone

PFA	Paraformaldehyide
pg	Picogram
PIKfyve	Inhibitor of mammalian phosphatidylinositol phosphate kinase PIP5KIII
proCURE	Programa contra la Resistència Terapèutica del Càncer
Puro	Puromycin
RIP	Rat insulin gene promoter
RIPA	Radioimmunoprecipitation assay buffer
RNA	Ribonucleic acid
RNAseq	Ribonucleic acid sequencing
rpm	Revolutions per minute
RPMI	Roswell Park Memorial Institute
RSEM	Reservoir Sampling based Ensemble Method
RT	Room temperature
RT-qPCR	Real-time quantitative PCR
s	Second
SD	Standard deviation
Sdc1	Syndecan 1
SDS	Sodium dodecyl sulfate
SERPINE1	Serpin Family E Member 1
Snai1	Snail Transcriptional Repressor 1
SOC	Super optimal broth
SPF	Specific pathogen free
Src	SRC Proto-Oncogene, Non-Receptor Tyrosine Kinase
TAE	Tris-acetate-EDTA
Tag	SV-40 large T antigen
TBS	Tris-buffered Saline
TCA	Trichloroacetic acid
TCGA	The Cancer Genome Atlas
TEMED	Tetramethylethylenediamine
TER	Transepithelial resistance
Tgfb1	Transforming Growth Factor Beta 1
TGN	Transgolgi
TJs	Tight junctions TJs
TK	Tyrosine kinase
TNFα	tumour necrosis factor alpha

TPBS	Triton-phosphate buffered saline
Tris	Tris(hydroxymethyl)aminomethane
TTBS	Tween-tris-buffered saline
UV	Ultraviolet
V	Volt
VEGF	Vascular Endothelial Growth Factor
WHO	World Health Organization
Zeb2	Zinc Finger E-Box Binding 2
β	Beta
βTC	Pancreatic beta cells
Δ	Delta

LIST OF FIGURES

LIST OF TABLES

SUMMARY

Local invasion is a key cell-biological event in the metastatic cascade. In response to a changing microenvironment, cancer cells may act using two main strategies of invasion: single cell invasion and collective invasion. Determining how tumor cells initiate and sustain local invasive Behaviour might help to improve patient diagnosis and lead to the development of new intervention modalities. Therefore, the aim of this thesis is to elucidate which molecular mechanisms are involved in PanNETs invasion before and after anti-angiogenic therapies.

Results from our group have demonstrated an irreversible increase in the incidence of invasive tumors during anti-angiogenic treatment in the RIP1-Tag2 mouse model. The RIP1-Tag2 mouse model is a valuable prototype of stepwise progression of tumorigenesis, and for this reason represents an appropriate choice for studying invasion in PanNETs. In addition, three dimensional models were developed with the aim of verifying the collective cell invasion process in βTC4 spheroids from RIP1-Tag2 tumors.

First, the morphology of RIP1-Tag2 tumors was described as collective tumor cell invasion, both before and after anti-angiogenic treatment. In detail, CLDN4 expression was associated with a high invasion capacity, reflected in the barrier function stability and adhesion union between cells. Cells and spheroid βTC4 models, in turn, demonstrated the functional implication of CLDN1 in the invasion of cancer cells. Finally, in clinical samples of PanNETs patients, CLDN1 was directly associated with tumor progression.

In summary, we identified a new link between barrier claudins, specifically 1 and 4, and the collective cell invasion process. In the future, through further validations, these markers could be used as tumor progression biomarkers for PanNETs tumors, as well as potential targets to intervene in collective invasion.

RESUMEN

La invasión local es un evento biológico celular clave en la cascada metastásica. En respuesta al microambiente tumoral, las células pueden actuar utilizando dos estrategias principales de invasión: la invasión de células individuales y la invasión colectiva. Determinar cómo las células tumorales inician y mantienen el comportamiento invasivo local podría contribuir en la mejora del diagnóstico del paciente y conducir al desarrollo de nuevas modalidades de intervención. Por lo tanto, el objetivo de esta tesis es determinar cuáles son los mecanismos moleculares involucrados en la invasión de PanNETs antes y después de las terapias anti angiogénicas.

Resultados previos de nuestro grupo demostraron un aumento irreversible en la incidencia de tumores invasivos durante el tratamiento anti angiogénico en RIP1-Tag2. Los ratones transgénicos RIP1-Tag2 son un prototipo detallado de la progresión gradual en la tumorigénesis, por ello representan un modelo animal ideal para estudiar el proceso de invasión *in vivo*. Además, se desarrollaron modelos tridimensionales buscando verificar el proceso de invasión colectiva en esferoides βTC4 derivados de tumores RIP1-Tag2.

En primer lugar, la morfología de los tumores RIP1-Tag2 se ha descrito como colectiva tanto antes y como después de la inhibición farmacológica de la angiogénesis. En detalle, la expresión de CLDN4 ha sido asociada a la capacidad de invasión colectiva, reflejada en la estabilidad de la función barrera y la integridad de la adhesión entre las células. Las células y esferoides βTC4, por su parte han demostrado la implicación funcional de CLDN1 en la invasión de células cancerosas. Finalmente, una asociación directa entre la expresión de CLDN1 y la progresión tumoral ha sido observada en las muestras clínicas de pacientes PanNETs.

En resumen, hemos descrito una nueva conexión entre las claudinas de barrera, especialmente las CLDN1/4 y el movimiento colectivo de invasión tumoral. En el futuro, a través de validaciones adicionales, estos marcadores podrían ser aplicados como biomarcadores de progresión tumoral de PanNETs, así como potenciales dianas para la modulación de la invasión colectiva.

INTRODUCTION

1. Metastasis cascade

According to the World Health Organization (WHO), cancer represents the second leading cause of mortality globally, and was cause for an estimated 9.6 million deaths in 2018. Nowadays, about 1 in 6 deaths is due to cancer. Metastasis is a hallmark of cancer, being responsible for as much as 90% of cancer-associated mortality (World Health Organization, 2018).

A complex sequence of cell-biological events are involved in the metastatic spread of cancer cells from primary tumors to distant parts of the body. During metastasis cascade, epithelial cells from primary tumors undergo the following steps: (1) invasion of surrounding tissue through extracellular matrix (ECM) and stromal cell layers (local invasion), (2) penetration into microvasculature of the blood vessels and lymph (intravasation), (3) survival in rigorous conditions of translocation through the bloodstream to microvessels into the parenchyma of distant tissue (survival in the circulation), (4) extravasation from the bloodstream (extravasation) (5) adaptation to foreign microenvironment of distant tissues, facilitating cell proliferation and micrometastases formation, and (6) finally once in metastatic sites, activation of their proliferative program to promote macroscopic, clinically detectable neoplastic growths (metastatic colonization) (**Figure 1**) (C. Chaffer and Weinberg 2011; Valastyan & Weinberg 2011).

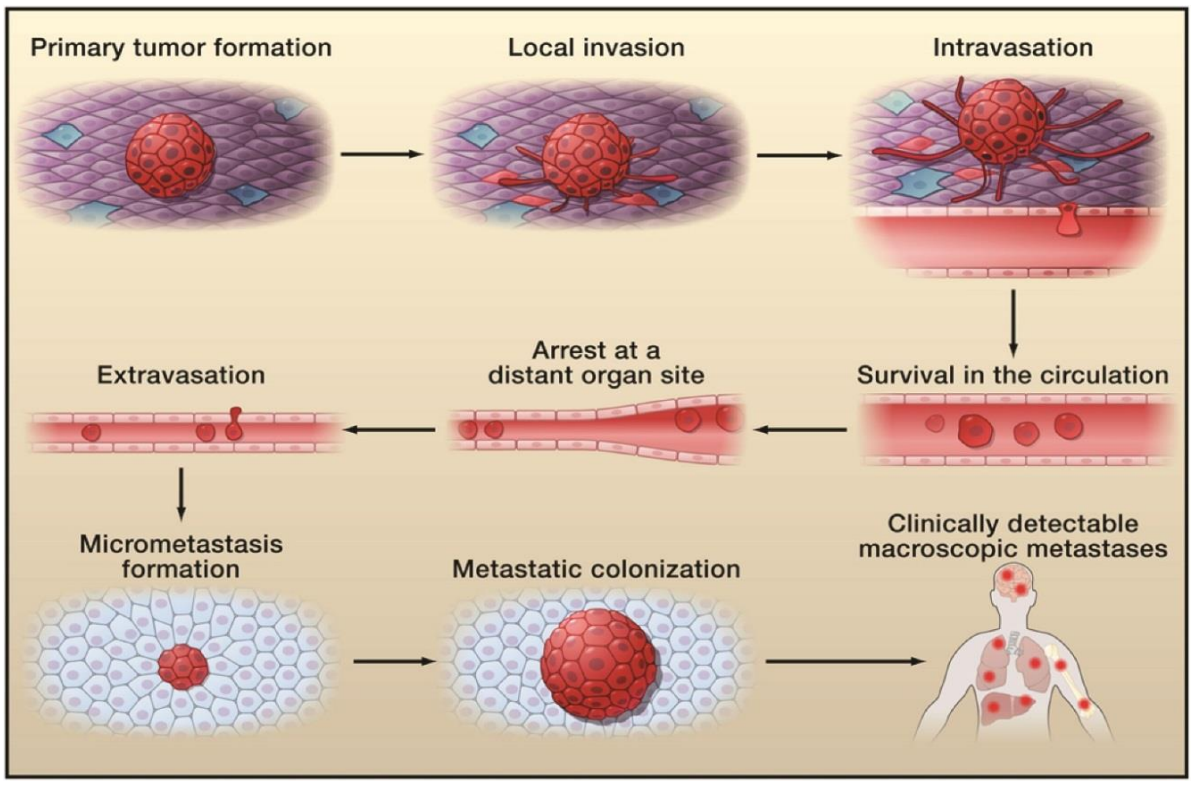

Figure 1. Steps of metastasis cascade. Tumor cells locally invade the surrounding tissue, enter and survive in microvasculature during the translocation to distant tissues, and finally adapt to the foreign microenvironment and colonize a second distant organ forming metastasis. Extracted from (Valastyan & Weinberg 2011).

2. Local invasion

Local invasion is an essential step of the metastatic cascade, given that, without it, none of the following metastatic steps may occur. In this sense, tumor microenvironment modifications play an important role in initiating the cell invasion process.

The basement membrane (BM) is a layer of specialized ECM composed of several glycoproteins and proteoglycans. Normally, the BM membrane supports the structure on which epithelial and endothelial cell layers grow, thus acting in epithelial tissue organization. The BM acts by preventing invasion into the subjacent stroma of tumors at early stages. Nevertheless, in malignant tumors, cancer cells disrupt regulatory mechanisms and induce proteolytic activities on

the BM and the interstitial ECM, favoring the cell invasion process (Lu, Weaver, and Werb 2012; Valastyan & Weinberg 2011).

In this way, at the 'carcinoma in situ' stage, cancer cells are still encapsulated by the BM and during local invasion cancer cells must first cross the BM. Due to BM degradation, the stroma becomes reactive with the cross-talk between tumor cells and stromal cells. Reactive stroma is characterized by an increased presence of immune cells and fibroblasts, which can help to deposit ECM and reorganize the stromal network. Consequently, stromal network fibers which before were well organized appear 'curly' and later increase in density and stiffness. In addition, the mixing of cancer and stroma cell types may further the disorganization of the tissue. Therefore, cancer cells from invasive tumors take advantage of a dysfunctional BM to migrate locally and invade toward the blood stream (**Figure 2**) (Clark and Vignjevic 2015). Thus, reciprocally, tumor cells influence the stroma and vice versa, together driving cancer progression (Peter Friedl and Alexander 2011).

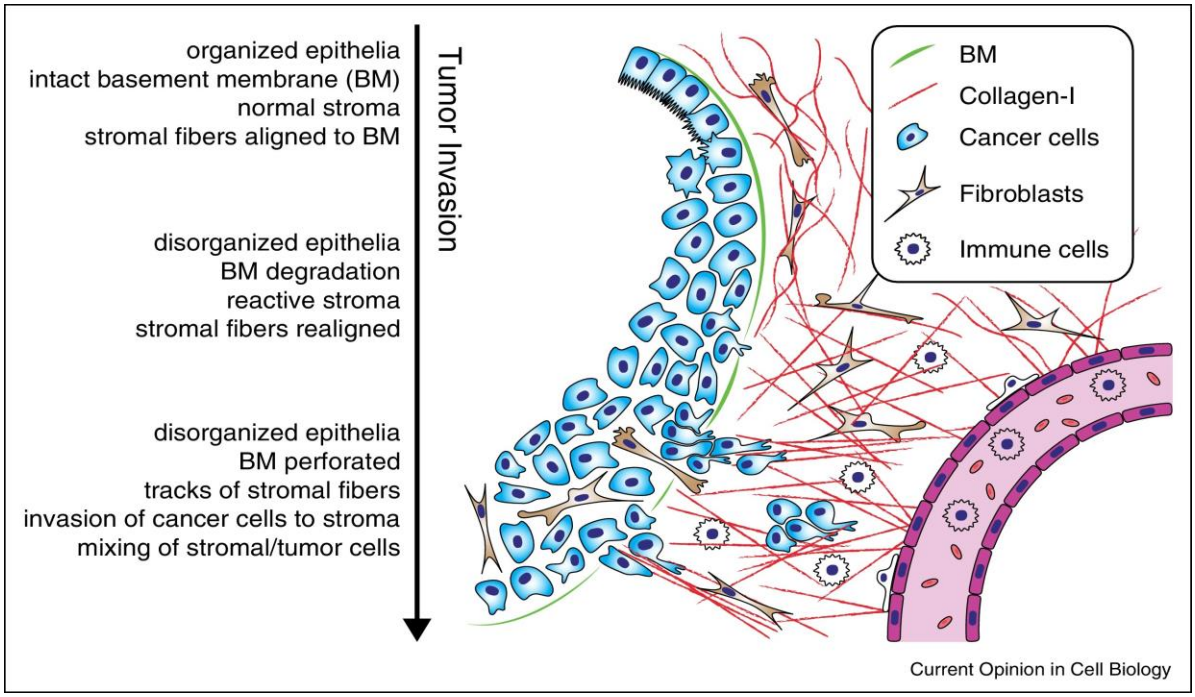

Figure 2. Tumor invasion microenvironment. Sequential microenvironment alterations that influence tumors cells and vice versa. Extracted from (Clark and Vignjevic 2015).

Despite the fact that tumor biologists have identified different mechanisms involved in malignant cell invasion, the attempts to define limiting mechanisms that govern invasive and metastatic cancer cell migration have largely failed. This is due to the fact that cancer cell invasion is a heterogeneous and adaptive process depending mainly on microenvironmental and diverse structural and molecular conditions (Peter Friedl and Alexander 2011). According to the cell type and tissue environment, cells may migrate using two major strategies—individually, when cell-cell junctions are absent, or, in solid cell strands, sheets, files or clusters, called 'collective migration', when cell-cell adhesions are maintained (**Figure 3**) (Peter Friedl and Wolf 2010).

Single cell and collective migration strategies are simultaneously present in many tumors. While leukemias, lymphomas and most solid stromal tumors such as sarcomas disseminate via individual cells, epithelial tumors commonly migrate by collective mechanisms. Generally, the lower the cell differentiation stage, the more likely the tumor is to migrate via single cell. Logically, the molecular repertoire in each migratory strategy is different according to the different movement pattern (Peter Friedl and Wolf 2003).

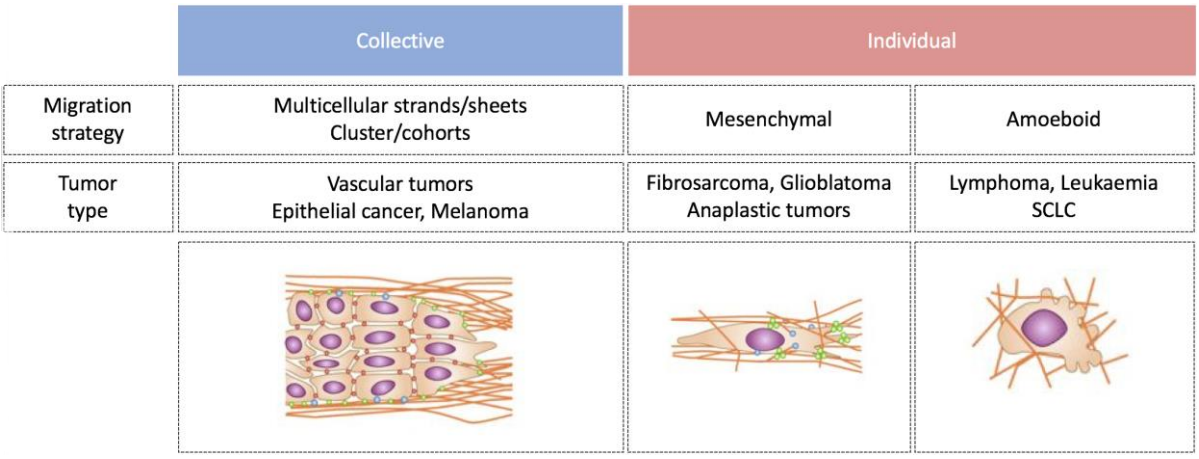

Figure 3. Individual cells and collective migration strategy. Variations of cell migration method and the most incident tumors of each type. Cell drawings have been extracted from (Van Helvert, Storm, and Friedl 2018).

2.1 Cancer cell migration

Many years ago the full EMT was considered crucial for cell movement, as it was believed that only cells with a mesenchymal phenotype, rather than epithelial cells, were able to migrate. Nonetheless, EMT has since been described as a process of intermediary phases, ranging from full EMT to partial, or even subtle states of EMT with very irregular Behaviours as to migration type and cell mobility (C. L. Chaffer et al. 2016). Nowadays, well-established examples of collective cell migration and invasion are known in many types of human malignant tumors (Wang et al. 2016).

Specifically, if monitored in a time-resolved manner, invasion programs are a continuous range of stages rather than discrete states, from stringently collective, to partial to complete but temporary individualization. The mechanisms of cell migration and invasion are plastic and allow the rapid adaptation to environmental changes and challenges; these adaptations often result in transitions between different modes of migration (Peter Friedl and Wolf 2010; Sanz-Moreno and Marshall 2010). Such plasticity likely originates in response to changing microenvironmental conditions and to therapeutic challenge. Further, the diversity of invasion is promoted by the rewiring of signaling networks and cell survival during therapy and tissue damage (Peter Friedl and Alexander 2011).

In particular, it has been identified that ECM parameters such as stiffness or density are able to regulate the transition between amoeboid-mesenchymal migration (AMT) and mesenchymal-ameboid transition (MAT) (Figure 5B-CD), which is a dynamic process in which cells display properties of both migratory phenotypes (Talkenberger et al. 2017). This same plasticity between different invasion states occurs in epithelial–mesenchymal transition (EMT), and in the mesenchymal–epithelial transition (MET) process (**Figure 4A-B**) (Peter Friedl and Gilmour 2009).

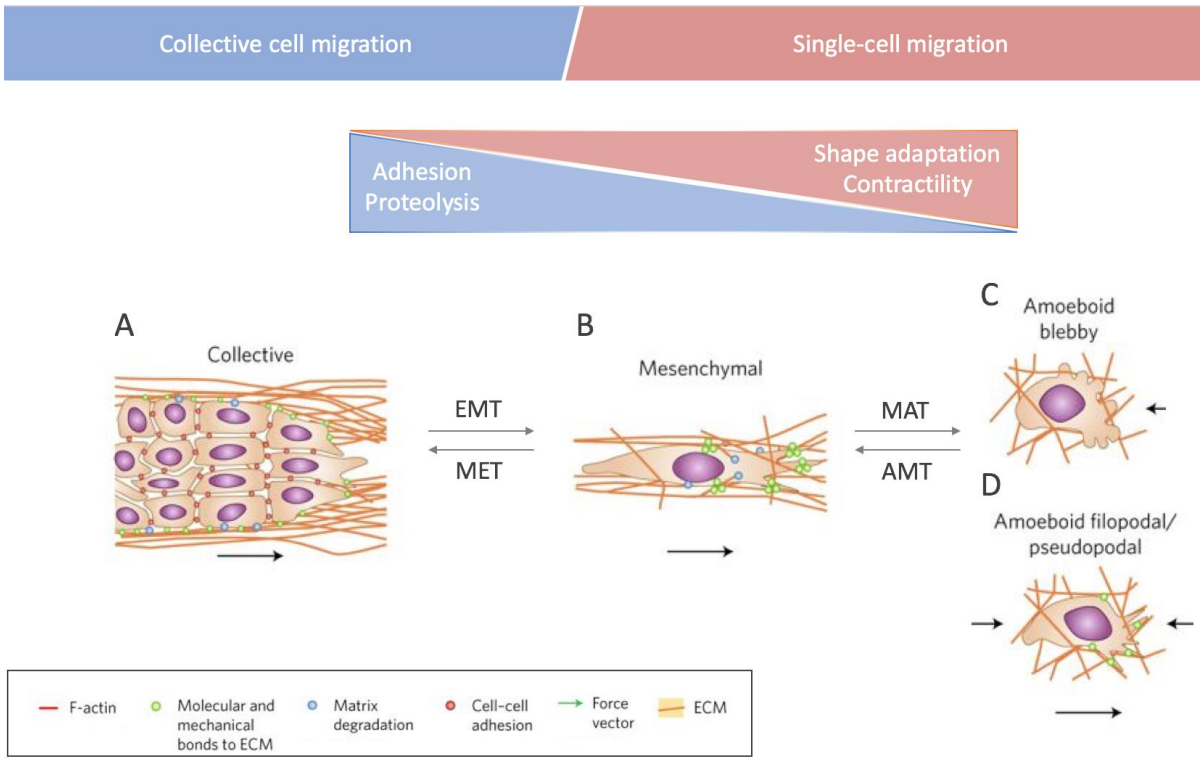

Figure 4. Plasticity among invasion and migration transition strategies. (A) Collective migration. **(B)** Mesenchymal migration. **(C)** Amoeboid blebby migration. **(D)** Amoeboid filopodal migration. Cell drawings have been extracted from (Van Helvert, Storm, and Friedl 2018).

Briefly, taking into account mainly migration features, the movement strategies are divided into: (i) collective cell migration, characterized by high levels of proteins responsible for cell adhesion, ECM degradation and union; the invasive cells from collective mode may undergo EMT transition (**Figure 4A**). (ii) mesenchymal migration, in which cells maintain ECM contact and degradation, and are thus able to pass by MAT and MET transition (**Figure 4B**), (iii) amoeboid migration, which is also distinguished by cellular adhesion to the substrate, in which 'amoeboid filopodal' cells maintain bonds to ECM, whereas 'ameboid blebby' cells not, these cells may suffer AMT transition (**Figure 4C-D**).

The role of each strategy of invasion will be further discussed in the following sections of this thesis.

2.1.1 Individual migration

Nowadays two types of individual migrating tumor cells are recognized: mesenchymal (fibroblast-like) and amoeboid.

2.1.1.1 Amoeboid/ Rounded

The term ‘amoeboid migration’ refers to the fact that amoeba *Dictyostelium discoideum* are known to migrate by this mechanism. During amoeboid movement, cells are characterized by migrating with low adhesion force, adopting spherical shapes or high contractility mediated by actomyosin. (P Friedl, Borgmann, and Bröcker 2001). Amoeboid tumors are frequently derived from hematopoietic or neuro-ectodermal tissue, including leukemias, lymphomas, and small cell lung carcinoma. Nonetheless, amoeboid movements are also found in cell subgroups of most other tumor types (Peter Friedl and Alexander 2011).

Amoeboid migration characteristics allow rapid adaptation to a given environment, as cells are highly deformable, their adhesion to the ECM is relatively weak, and proteolytic action is reduced or absent. Cells develop high migration velocities due to low adhesion among other cells, moving faster than cells in mesenchymal migration mode (Talkenberger et al. 2017). These migration characteristics allow rapid adaptation to a given environment, development of high migration velocities, and contact with other cells in a dynamic yet reversible manner (P Friedl, Borgmann, and Bröcker 2001).

The morphological shape, type of cell protrusions and cytoskeletal flexibility are regulated by two GTPase proteins RhoA and Rac. Cell direction, determined by polarization and retraction, are controlled by cortical actomyosin contractility which is regulated by RhoA via Rho kinase (ROCK) signaling and myosin II activity (Boekhorst and Friedl, 2016).

However, amoeboid movement may be classified according to cellular adhesion to the substrate. Blebby ameboid migration is mediated by contractile Rho-directed actomyosin and lacks defined adhesions, cell translocation is mediated by propulsion using either blebs or lateral intercalation (Figure 6C).

Filopodal ameboid migration already uses Rac-dependent filopodia (Figure 6D). Thus, cells present small or diffusely organized adhesion sites that generate weak to negligible adhesion force toward the substrate (Lorentzen *et al.*, 2011; Poincloux *et al.*, 2011; Boekhorst and Friedl, 2016).

In particular, amoeboid cells follow the trend of migrating in the absence of proteolytic ECM breakdown, in this sense cancer cells use actomyosin-based mechanical forces to physically displace matrix fibrils. In fact, clinical trials that demonstrated MMP inhibitors failure to prevent cancer progression confirm this hypothesis and suggests protease-independent mechanisms of invasion as a potential mechanism relevant *in vivo* (Peter Friedl and Alexander 2011; Sabeh, Shimizu-Hirota, and Weiss 2009).

2.1.1.2 Mesenchymal

The mesenchymal migration mode is often observed in sarcomas, gliomas, and epithelial cancer cells after undergoing epithelial-to-mesenchymal transition (EMT) (Chanrion et al. 2014). The EMT process represents a cell biological program that concomitantly suppresses epithelial markers whereas upregulating mesenchymal ones (C. L. Chaffer et al. 2016). Briefly, mesenchymal tumor cells often express EMT markers, including inducing transcription factors (EMT-TFs) Oct-4, Twist, Snail/Slug, Zeb1/2 and cytoplasmic vimentin, which allow their detection in tissue samples in infiltrating remodeled tissue (**Figure 5**) (A. Smith, Teknos, and Pan 2013; Zeisberg and Neilson 2009; Lamouille, Xu, and Derynck 2014).

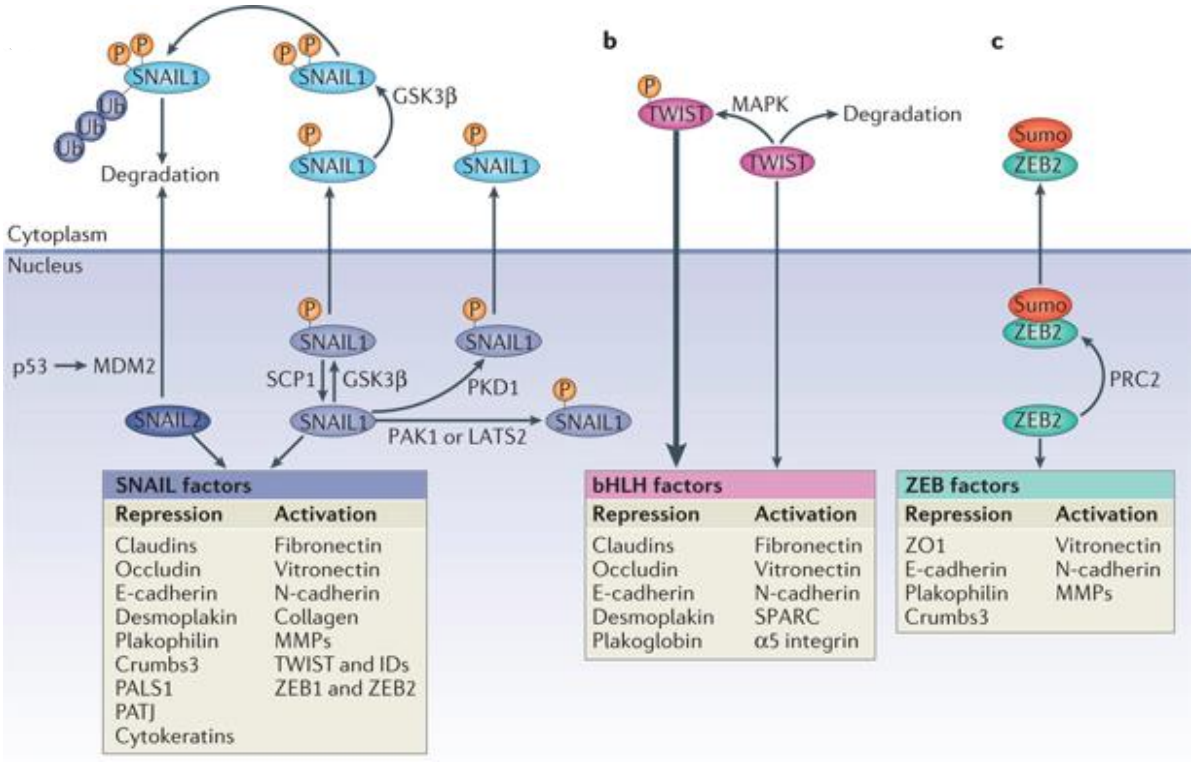

Figure 5. Roles of major EMT transcription factors. Epithelial–mesenchymal transition (EMT) is driven by SNAIL, zinc-finger E-box-binding (ZEB) and basic helix–loop–helix (bHLH) transcription factors that repress epithelial marker genes and activate genes associated with the mesenchymal phenotype. Extracted from (Lamouille, Xu, and Derynck 2014).

In particular, EMT-TF genes when combined and activated may confer an increase of migratory and invasive capacity on cells, facilitating, in consequence, EMT-responsive cells movement out of primary tumor sites and into the circulation, thereby enabling their metastatic potential (**Figure 6**). In relation, tumor microenvironment influence on the epithelial cancer cells is intermediated via heterotypic cell-cell signaling molecules, among which are Wnt, TGFβ and Notch. Overall, as research increases and the connections between EMT and carcinomas are elucidated, the signaling player numbers implicated in driving the EMT keeps growing (C. L. Chaffer et al. 2016).

In relation to canonical molecules contribution to EMT process, a wide range of growth factors including the epidermal growth factor (EGF), insulin growth factor (IGF), hepatocyte growth factor (HGF), fibroblast growth factor (FGF) and platelet-derived growth factor (PDGF) have also been described as an

EMT program trigger. As well as hypoxia-inducible signals involving the transcription factor HIF1-α, as well as, inflammatory signals (NF-κB) and cytokines, such as interleukin-1β (IL-1β) and the tumour necrosis factor alpha (TNFα), showed to cooperate in the complex network of signals involved with EMT activation within carcinoma cells (Lamouille, Xu, and Derynck 2014; B. Smith and Bhowmick 2016).

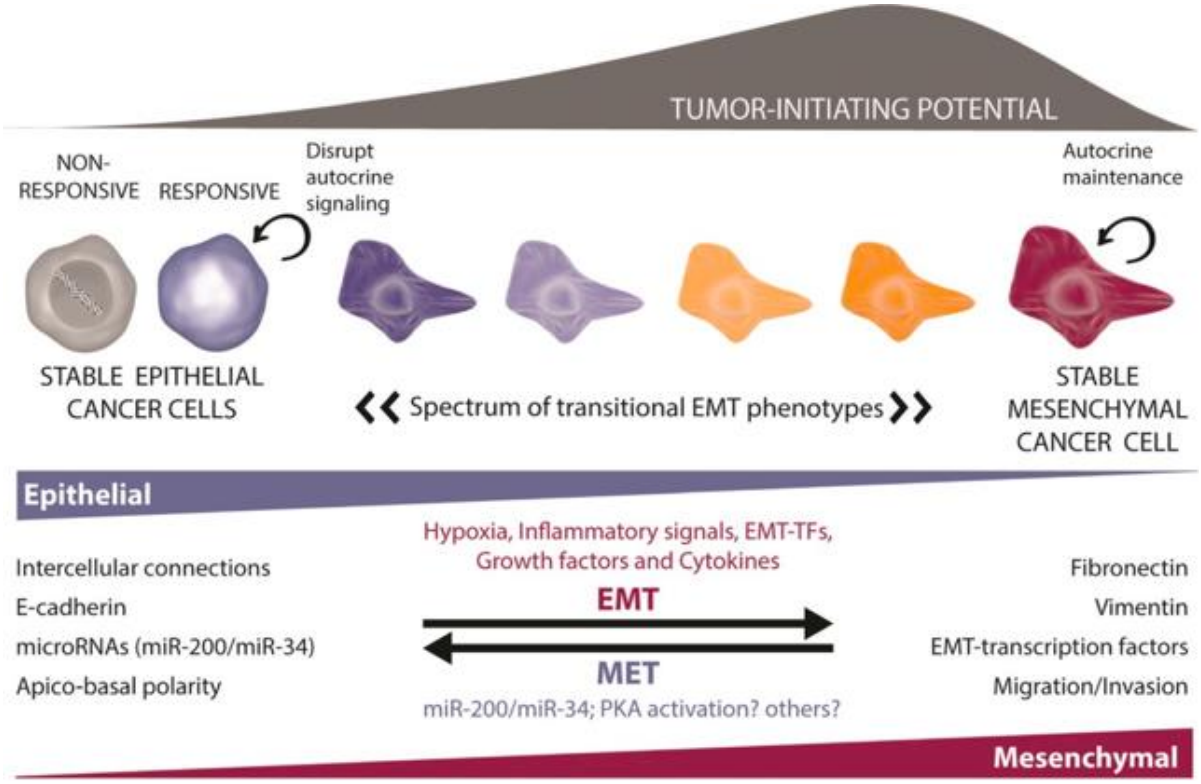

Figure 6. States of EMT phenotypes in cancer. The mesenchymal tumor cell morphology is determined by an elongated cell shape with an oval nuclear and a protruding pseudopod and/or multiple filopods, which are responsible for determining the direction of migration by adherence to and pull on ECM substrate. In the cell edge, Rac-induced actin assembly and integrin binding to the substrate induce cell polarization and protrusion. At the same time as integrin, also FAK and Src kinases induce maturation of focal ECM adhesion, determining thus a contractile tension and pulling forces toward ECM structures. On the other hand, at the rear, actomyosin contractility induced by RhoA reduces anchorage of the cell rear and leads to forward sliding of the cell body(Boekhorst and Friedl, 2016).

The mesenchymal tumor cell morphology is determined by an elongated cell shape with an oval nuclear and a protruding pseudopod and/or multiple filopods, which are responsible for determining the direction of migration by

adherence to and pull on ECM substrate. In the cell edge, Rac-induced actin assembly and integrin binding to the substrate induce cell polarization and protrusion. At the same time as integrin, also FAK and Src kinases induce maturation of focal ECM adhesion, determining thus a contractile tension and pulling forces toward ECM structures. On the other hand, at the rear, actomyosin contractility induced by RhoA reduces anchorage of the cell rear and leads to forward sliding of the cell body (Boekhorst and Friedl, 2016).

Therefore, Rac-mediated cell elongation at the leading edge and Rho-induced rear contraction allows cycles of cell-matrix adhesion, pulling and relaxation on cell structure, thus, promoting cell movement. In addition, concomitant with this process, surface matrix metalloproteases (MMPs) remove ECM structures and barriers, promoting tissue remodeling and generating a tissue along the spatially widened migration path (**Figure 4B**) (Boekhorst and Friedl, 2016).

2.1.2 Collective migration

In the ecosystem innumerable birds, fish, arthropods and land animals live and migrate in groups. This Behaviour is a manner that protects them and increases the probability of reaching their final destination. Similarly, coordinated cohesive groups or nests are formed to migrate toward their destination during multicellular organisms development and the progression of human diseases (Peter Friedl and Mayor 2017). In this way, the collective migration is determined by three main cell Behaviours (Peter Friedl and Gilmour 2009):

i) Cells remain physically and functionally connected such that the cohesion of cell–cell junctions is maintained during movement.

ii) Traction and protrusion force for migration and maintain cell–cell junctions is determined by multicellular polarity and 'supracellular' organization of the actin cytoskeleton.

iii) Moving cell groups change the tissue along the migration path, either by clearing the track or by causing secondary ECM modifications.

The neural crest cells and neuroblasts migrate in an organized manner and retain intercellular adhesion to go through long distances and form discrete tissues and organs. Angiogenic events also showed cells migrating in groups during retina development and inflammatory diseases (**Figure 7A**) (Wang et al. 2016). In cancer, it has been described that collective invasion is an important strategy for local tissue infiltration, as well as metastatic evasion in epithelial tumors such as breast cancer, squamous cell carcinoma, pancreatic cancer, colon cancer, and others (**Figure 7B**), as well as, in mesenchymal tumors (Peter Friedl and Mayor 2017).

Collectivity of migrating cancer cells shows innumerable advantages for surviving the metastatic cascade in comparison to individual-cell migration, including: (i) a highly promigratory and prosurvival environment between connected cells by secretion of growth factors, chemokines and proteases; (ii) the passive displacement of otherwise poorly mobile or even immobile but highly proliferative cells inside the strands by highly mobile neighbor or leader cells; and (iii) safety of cells located in inner regions of groups, such as reduced immune cell attack or lower shear stress and nuclear damage in the tissue or vasculature (Boekhorst and Friedl, 2016).

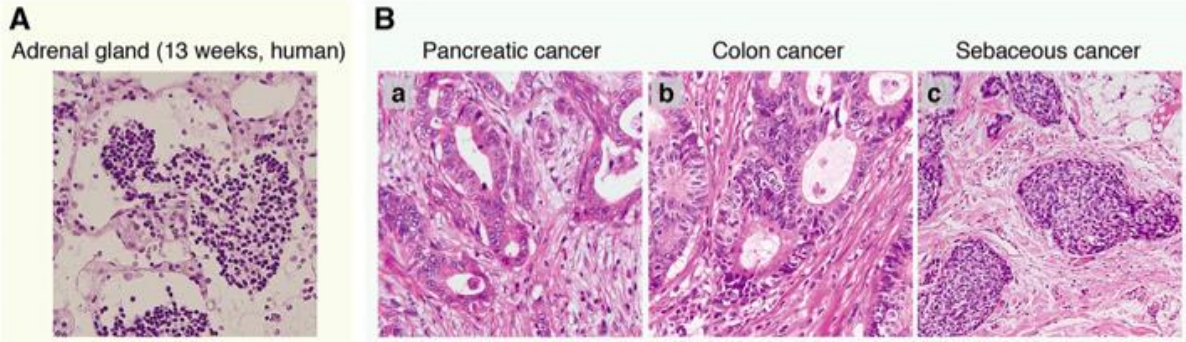

Figure 7. Collective cell migration verified in the body development and human cancer. (A) Developing adrenal gland in 13-week human embryo, showing the groups of neural crest-derived cells. Hematoxylin and eosin stain. **(B)** Representative images for different human cancers: (a)

adenocarcinoma in the pancreas, (b) adenocarcinoma in the colon, (c) sebaceous carcinoma in the skin. Image has been adapted from (Wang et al. 2016).

Overall, collective movement may vary depending on the context. Thus, collective cell movement can happen across a tissue surface by two-dimensional migration monolayers, when cells move across tissues to form a single-layered or multilayered epithelium (**Figure 8A**) or by multicellular strands through a three-dimensional tissue scaffold (**Figure 8B–F**). In this case, multicellular 3D strands cells can generate of an inner lumen (and therefore a tube structure), such as in gland formation (**Figure 8B**) or vascular sprouting during angiogenesis (**Figure 8**C), or they may move as mass poorly organized (strands), such as in invasive cancer (**Figure 8D**). Also, isolated groups can move through tissue if they detach from their origins; such as border cells in the *Drosophila melanogaster* egg chamber (**Figure 8E**) and metastatic cancer cell clusters that penetrate the tissue stroma (**Figure 8F**) (Peter Friedl and Gilmour 2009).

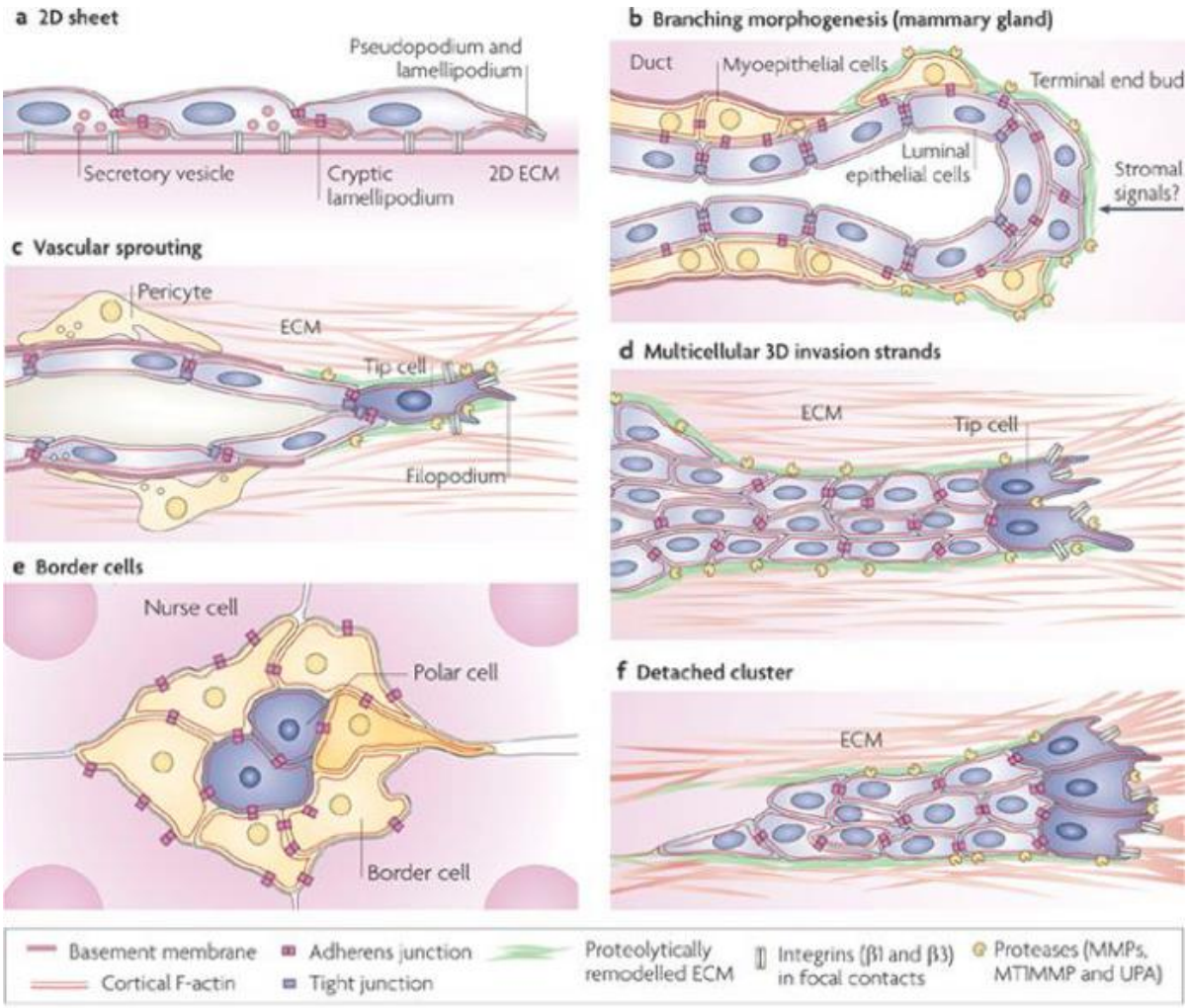

Figure 8. Patterns of collective cell migration depending on the context. (A) two-dimensional migration monolayers **(B-F)** multicellular strands migration through a three-dimensional tissue scaffold. Extracted from (Peter Friedl and Gilmour 2009).

In the context of cancer cell invasion, all types of collective movements may be adopted by tumor cells. According to histological samples from both patient lesions and mouse models *in vivo*, it was verified that collective invasion patterns present a striking morphological and molecular variability depending on tumor type and the tissue that is invaded (Boekhorst and Friedl, 2016; Friedl and Mayor, 2017).

Mechanically, cell-cell contacts coordinate and polarize collective migratory cells into a multicellular functional single system (Peter Friedl et al. 2012). Different levels of actin dynamics, substrate interaction and remodeling of ECM

define leader and follower cell Behaviours. At the invasive front, leader cells through Rac-guided filopodia protrusions and integrin-mediated substrate adhesion connect with surrounding tissue structures (Yamaguchi et al. 2015). Rho molecule has highest activity towards the cell front, generating actomyosin-mediated contractility and pulling force between the substrate and follower cells. In this context specially, follower cells depend on stable cell-cell adhesion to withstand the drag forces generated by the leader cells and Rho-mediated actin contraction. cell-cell junctions are maintained by cadherins (especially by E-cadherin in epithelial tumors) and their connection with cortical actin mediates the stability of the adherent junctions. Also, proteolytic remodeling of the matrix, particularly through MMPs, to generate a path of least resistance over from which the cells advance (Figure 9D) (Haeger *et al.*, 2014; Boekhorst and Friedl, 2016)

Other cell-cell adhesion systems include members of the immunoglobulin superfamily and adhesions of ephrins/EpH receptors that mediate slower or transient cell-cell interactions, as well as connexins, which allow communication through communicating junctions and signal transduction between connected tumor cells (Boekhorst and Friedl, 2016). Finally, it is important to emphasize that proteins responsible for coordinating the collective movement are still poorly understood, changing depending on the type of cancer tissue and the overall contexts. Furthermore, neither is it clear yet whether leading cells exist in all types of cancers or not (Wang et al. 2016).

2.1.2.1 Collective migration/invasion models

Studying collective invasion in vitro

2D assays: Scratch/wound assays analyse cell migration across a flat surface. Benefits involve the technical simplicity and suitability for large-scale assays. As disadvantages are restriction to 2D substrates. Time-lapse imaging may evaluate cell-cell junction stability, cell–neighbor relationships and traction-force generation (Peter Friedl et al. 2012).

3D ECM-based assays/3D ECM spheroid invasion assay: Multicellular clusters or aggregates seeded into 3D ECM (such as collagen I or Matrigel®), with or without presence of another type of cell, favoring radial invasion of individual cells and multicellular strands. Aggregate size and shape, and cell–cell adhesion junction immunostaining, may differentiate between individual and collective invasion. The level of collective and individual cell invasion is measured through number of invasive strands or cell and vertical penetration depth (Peter Friedl et al. 2012).

Studying collective invasion in vivo

Animal models: Studies can be performed in mice that develop tumors spontaneously, or with heterotopic and orthotopic tumor implants. Mutant mice mimic natural tumor progression, but their unpredictable progression requires careful early stage tracking. Heterotopic sites are ideal for direct imaging, whereas orthotopic injection into the tissue of origin most accurately recapitulates the tumor microenvironment (Peter Friedl et al. 2012).

Histological studies: Typical histological and immunohistochemical analysis should determine the extent of invasion, whether invading cells are cohesive maintaining intact cell–cell junctions, and the connection with human pathology information (Peter Friedl et al. 2012).

Intravital imaging: Intravital microscopy of tumor cells may characterize the type of invasion (collective and individual), their speed and localization In addition, time-lapse 3D monitoring of cell dynamics can provide cellular and subcellular resolution to characterize both single-cell and collective invasion.

Multiple imaging session studies: The transparent imaging windows are recommended for serial imaging of a tumor area to long-term for days or weeks. This method allows an accurate assessment of slow cell and tissue dynamics, including collective invasion and tumor growth (Peter Friedl et al. 2012).

Challenges of in vivo imaging: Some technical problems that can confound collective invasion analysis such as passive drift of cells or tissue regions, tissue compaction or artefacts due to surgery. These difficulties may be overcome by optimizing sample positioning through custom tissue holders; using long-term window chambers to prevent impact on the tissue structure before or during imaging; monitoring collective invasion over days and weeks (Peter Friedl et al. 2012).

3. Claudin family

3.1 Structure function of claudins

Claudins are part of tight junctions (TJs) adhesion complexes, in which plasma membranes of neighbor cells become closely united, forming an impermeable barrier between cells within the tissue (Figure 11A) (Peter Friedl and Mayor 2017). There are thought to be around 26 human claudins with physiological role. Claudins have between 207 and 305 amino acids and possess molecular masses of 21–34 kDa (Günzel and Yu 2013).

General structure of claudins is determined by an intracellular NH2 terminus together with a longer intracellular COOH terminus, two extracellular loops (ECL1, which is larger, and a smaller ECL2), and one short intracellular loop (Günzel and Yu 2013). The larger first loop is responsible for specific paracellular tightening ion permeability, whereas the shorter second extracellular loop seems determinant to adhesive function between the opposing cell membranes (Figure 10B) (Scarpa et al. 2017; Günzel and Yu 2013; Markov, Aschenbach, and Amasheh 2015).

In addition, the claudin family possesses a COOH-terminal PDZ-binding motif, through which the majority of claudins, are able to connect with PDZ domains from scaffolding/adapter proteins such as ZO1, ZO2, ZO3. In turn, this interaction also control a several signaling pathways involved in actin organization, cell polarity, as well as transcriptional regulation (González-Mariscal et al. 2014).

As to interactions between the claudins within one tight junction which can be considered: homo- and heteromeric interactions that may happen in cis or in trans. Recent evidence demonstrated that claudin-1 is able to trans-interact with -3, but not with claudin-2 or claudin-4. However, the claudins ability to trans-interact between themselves is a matter of debate (**Figure 9C**) (Günzel and Yu 2013).

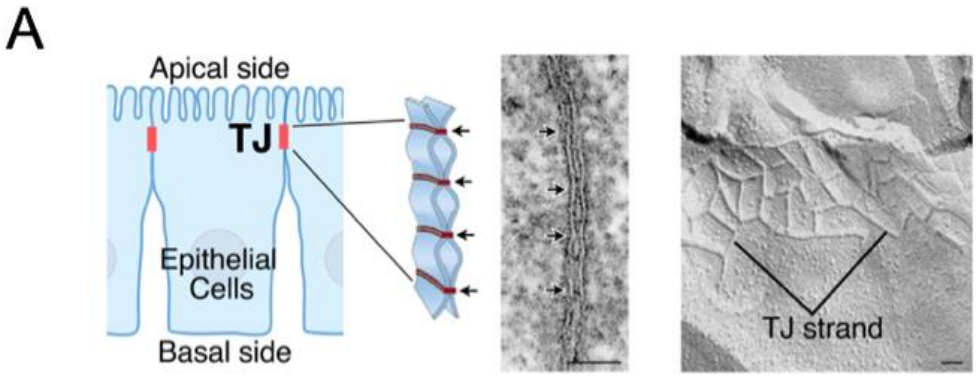
A
Apical side
TJ
Epithelial Cells
Basal side
TJ strand

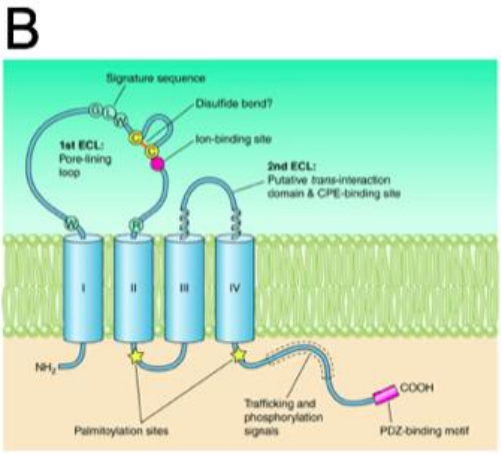
B
Signature sequence
Disulfide bend?
Ion-binding site
1st ECL:
Pore-lining loop
2nd ECL:
Putative trans-interaction domain & CPE-binding site
I
II
III
IV
NH2
COOH
Palmitoylation sites
Trafficking and phosphorylation signals
PDZ-binding motif

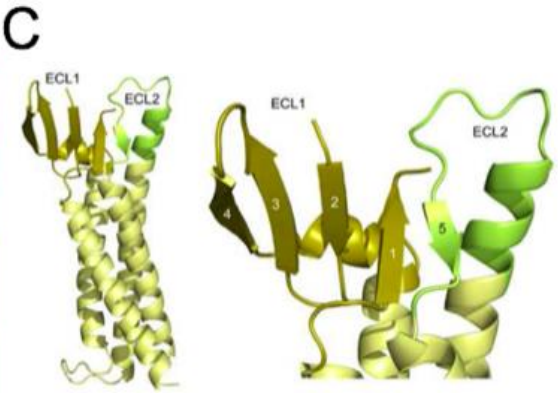
C
ECL1
ECL2
ECL1
ECL2

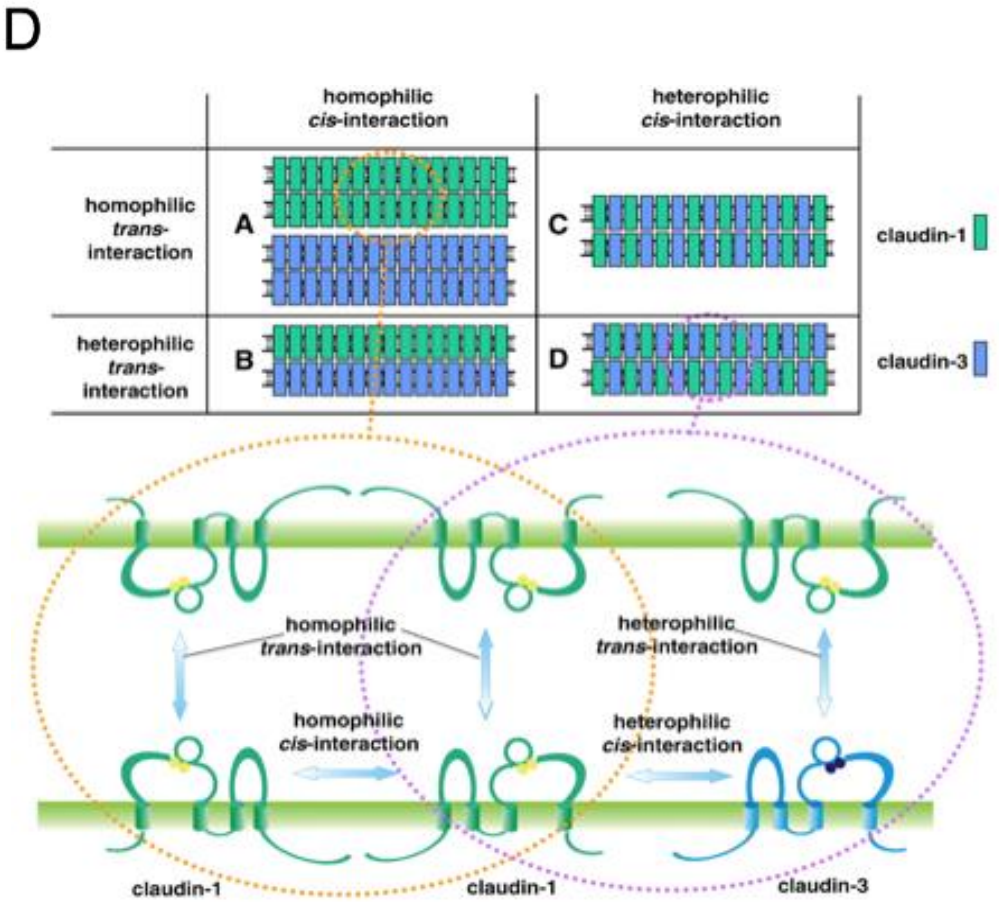
D
homophilic cis-interaction
heterophilic cis-interaction
homophilic trans-interaction
A
C
claudin-1
heterophilic trans-interaction
B
D
claudin-3
homophilic trans-interaction
heterophilic trans-interaction
homophilic cis-interaction
heterophilic cis-interaction
claudin-1
claudin-1
claudin-3

Figure 9. Claudins structure and function. (A) Location of TJs between epithelial cells and schematic drawing of a TJ membrane. **(B)** Secondary structure of claudin protein (**C)** Crystal structure of Cldn15 **(D)** Interaction possibilities between claudins such as, reported for claudin-1 and -3. Images have been adapted from (Günzel and Yu 2013; Gerd Krause et al. 2008; G. Krause, Protze, and Piontek 2015; Tamura and Tsukita 2014).

A general property of claudins in the TJ is the paracellular sealing function, which is tissue-, size- and charge-selective. Thus, it was defined that claudins operate predominantly as barriers or pores that are selective to cations and ions. Barrier forming claudins are those claudins that increase in transepithelial resistance (TER) sealing the cells, whereas pore-forming claudins decrease TER, increasing paracellular permeability (Günzel and Yu 2013; Gerd Krause et al. 2008). Claudins that unequivocally are qualified as pore-forming claudins are: claudin-2, -10b, and -15 as cation pores and claudin-10a and -17 as anion pores, being that claudin-2 acts as the only paracellular water channel known until now. The barrier-forming claudins that decrease a permeability to cations are: claudin-1, -3, -4, -5, -6, -8, -9, -11, -14, -18, and, finally claudin-19 acts decreasing permeability to anions (Günzel and Yu 2013; Gerd Krause et al. 2008; Tamura and Tsukita 2014; Markov, Aschenbach, and Amasheh 2015; Rosenthal et al. 2017).

3.2 Claudin family and its role in cancer

Accumulated data has demonstrated that some claudins expression are decreased or increased in human tumors in a tissue-specific mode, indicating a possible specific mechanism in targeting cells during carcinogenesis (**Figure 10**). Specifically, claudin expression alterations have been shown to be significantly correlated with different steps of prognosis, such as patient survival and recurrence in some cancers, suggesting the claudin family as prognostic markers in some cancers (Osanai et al. 2017).

Table 1 Dysregulated claudin expression in cancers originating from various organs

Cancer origin	Claudin subtype									
	Claudin-1	Claudin-2	Claudin-3	Claudin-4	Claudin-5	Claudin-7	Claudin-10	Claudin-16	Claudin-18	Claudin-23
Breast	↑↓		↑↓	↑↓		↓				
Lung, adenocarcinoma	↓				↑					
Lung, squamous cell carcinoma	↑				↓					
Esophagus, squamous neoplasia	↑↓		↑	↑		↑↓				
Stomach	↑		↑	↑↓		↑			↑↓	↓
Large intestine	↑↓	↑	↑	↑↓	↑	↑↓				
Liver, hepatocellular carcinoma	↑↓	↑		↓		↑↓	↑			
Biliary tract				↑		↑			↑	
Pancreas	↓		↑	↑	↑				↑	
Bladder				↑↓						
Kidney	↑		↑	↑		↑				
Prostate	↑		↑	↑	↓	↑				
Ovary, epithelial carcinoma	↓		↓	↑	↑	↑		↑		
Uterine cervix	↓	↓		↓		↓				
Uterine corpus			↑	↑		↓				

"↑" increased, "↓" decreased expression in tissue of interest

Figure 10. Claudin expression dysregulated in cancers from various organs. Image has been adapted from (Osanai et al. 2017).

In detail, as to collective invasion, until now among all claudin family components, only claudin-1 was related to collective migration/invasion in *in vitro* studies. According to these results, claudin-1 is a key protein that facilitates the collective invasion in mammary and cervical carcinoma cells (Fortier, Asselin, and Cadrin 2013; Giampieri et al. 2009). In the case of rat mammary cells, single cell migration was found under high TGFβ expression, leading to metastases. Nonetheless, with TGFβ inhibition, high claudin-1 expression levels were verified and, led to cancer cells moving collectively, resulting in the lymphatic invasion of these cells (Giampieri et al. 2009). In addition, in cervical carcinoma cells, once again, the capacity of claudin-1 to induce collective migration was demonstrated. This time, as a consequence of knockdown of keratin (K8/18), higher collective migration was shown and invasion capacity of the tumor cells through claudin-1 protein and independently of EMT markers. Through this knowledge, it was

suggested that claudin-1 increases cell cohesion and consequently, facilites and promotes the collective cell migration (Fortier, Asselin, and Cadrin 2013).

4. Pancreatic neuroendocrine tumors

Neuroendocrine tumors (NETs) are epithelial tumors with essentially neuroendocrine differentiation which have the same phenotype in common. Although at different levels, these tumors have propensity to metastasize to the liver, independently of the primary tumor origin (Lewis et al., 2017). It has been calculated that the incidence of NETs could represent 7 cases per 100,000 people. In fact, this rate significantly increased in recent years, being in part a relative true increase in incidence, and, on the other hand, this increase may reflect better detection and improved diagnosis observed in the recent years (Yao et al. 2008).

Pancreatic neuroendocrine tumors (PanNETs) form in hormone-making cells (islet cells) of the pancreas. The PanNETs annual incidence has approximately 1 per 100,000 individuals per year (**Figure 11**), thus, representing the second most common epithelial neoplasm from pancreas. Further, these tumors show a discouraging mortality rate of 60% of diagnosed cases (Lewis et al., 2017)

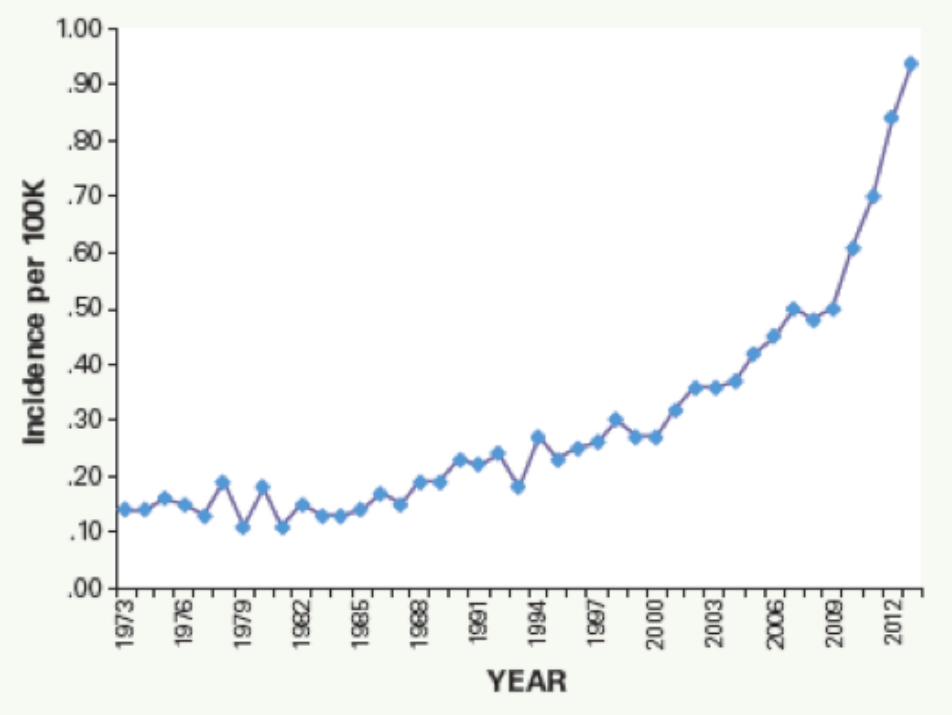

Figure 11. Incidence of PanNETS annually in the period from 1973 to 2013. PanNETs incidence by year of diagnosis. Extracted from (Lewis et al., 2017).

The classification for PanNETs was performed to organize tumors according to their associated-function to hormones secretion in two groups: non-functional and functional types. Among functional and secreting tumors are insulinoma, glucagonoma, and others. Already, non-functional PanNETs do not result in syndromes of hormonal excess, but, on the other hand, invade normal tissue and metastasize causing higher mortality rates (Ehehalt et al. 2009). It is known that most PanNETs are non-functional, and 85% will develop metastases during their life (Lawrence et al. 2011). Overall, metastasis in PanNETs independently of functional classification, represent 4 years less mean duration in survival in relation to small intestine NETs, both patients diagnosed within 1 year with metastatic disease (**Figure 12**) (Ter-Minassian et al. 2013).

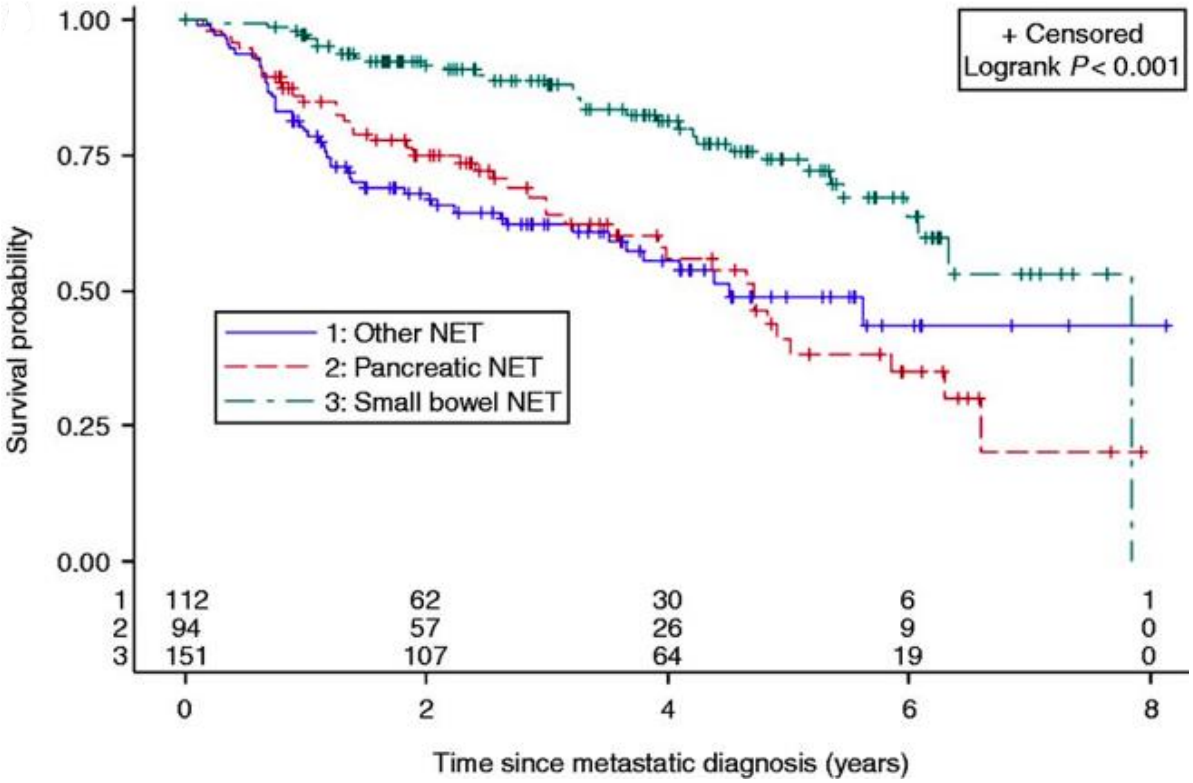

Figure 12. Survival for patients with metastatic disease according to PanNETS tumor subtype. Through Kaplan–Meier method, it has been verified that the median survival duration was of 5.2 years for the cohort overall, 7.9 years for small bowel NET, 3.9 years for PanNET, and 3.7 years for other NET. Extracted from (Ter-Minassian et al. 2013).

It is now well established that surgery is the standard recommendation for PanNETs treatment, since surgical resection procedure stands as the only potential cure. As to metastatic approach, recent evidence reports that the median survival of patients that developed metastatic focus undergoing resection of the primary site to be 65 months versus 10 months for those without resection (Kelgiorgi and Dervenis 2017). Aside from this, choice of treatment is determined by tumor heterogenous nature and consists in a politherapeutical scheme involving a combination of targeted therapies, systematic chemotherapy and octreotide analogs (Lewis et al., 2017).

In recent times, novel targets contributed to the discovery of new treatment possibilities for patients and also broadened our knowledge about the biology of PanNETs. The PanNETs biomarkers identification help us to predict the response to targeted therapy and to develop more effective targeted therapy itself, thus,

improves future expectations, because it brings us closer to a personalized, patient-tailored treatment (Kelgiorgi and Dervenis 2017). In this way, in order to determine new biomarkers, increasing research with a focus on PanNETs for which preclinical model usage is crucial, is needed.

5. RIP1-Tag2 as a pancreatic neuroendocrine tumor mouse model

The RIP1-Tag2 is the transgenic animal model of pancreatic β-cell carcinogenesis, that has been used to identify several mechanisms involved with cancerous disease. The expression of insulin-producing islet β cells promotes PanNETs induction. Specifically, SV-40 large T antigen (Tag) is expressed in all islet cells from RIP1-Tag2 at birth under the control of the rat insulin gene promoter (RIP) (**Figure 13**). This T-antigen expression abrogates p53 and RB tumor suppressors in in β-cells, which elicits the sequential development of tumors in the islets over a period of 12–14 weeks, reaching a maximum degree of aggressiveness at 16 weeks of age.

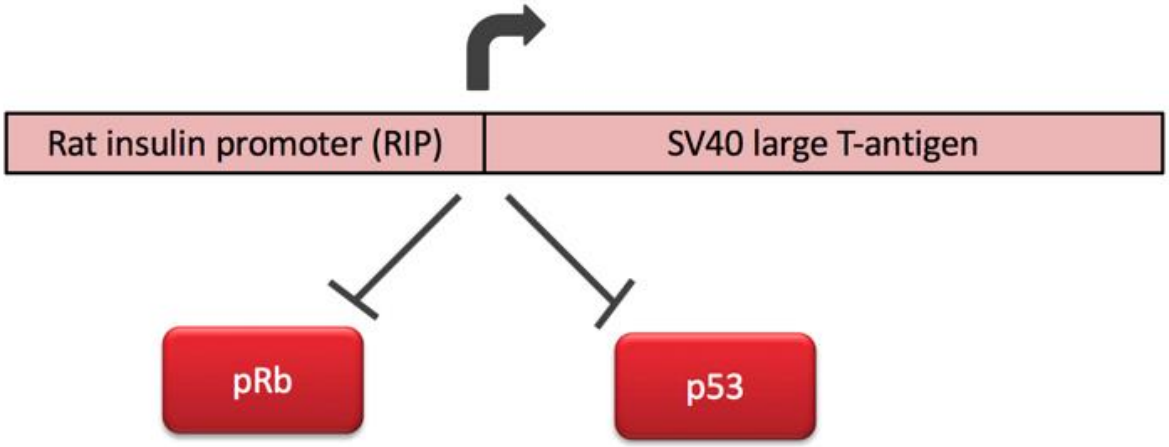

Figure 13. Gene construct from RIP-Tag2 animal model. The rat insulin promoter (RIP) fusion with the large T antigen of simian virus 40 (SV40) promotes perturbation in the p53 and pRb pathways, favoring the appearance of tumors in the pancreatic islets over a period of 12-14 weeks.

Among all islets that express T-antigen oncogene about half the 400 islets become hyperproliferates (Folkman et al. 1989), and, 15–20% of these angiogenic islets turn on into benign tumors, encapsulated lesions and invasive

carcinomas (Lopez and Hanahan 2002). Tumor evolution occurs by stages (**Figure 14A**), in this way, hyperplastic/dysplastic islets start appearing at 3 weeks of age. Then, 25% of hyperplastic islets switch on angiogenic signaling between 6 to 9 weeks (Folkman et al. 1989). The switch is determined by vascular dilation, microhemorrhaging, and, endothelial proliferation. At the last steps of 14-16 weeks 2 to 10 PanNETs to each animal are found (Efrat et al. 1988). In this point, islet tumors in RIP1-Tag2 tumors may finally lead to liver metastasis, similar to what occurs in human PanNET patients.

RIP1-Tag2 mice may develop PanNETs of different malignancy level, from islet tumors to invasive carcinomas. Islet tumors (IT) are tumors with well-defined margins, encapsulated and surrounded (**Figure 14B**). Malignant RIP1-Tag2 tumors are classified according to their invasion of the adjacent tissue. Invasive carcinoma type 1 (IC1) shows focal regions of invasion with adjacent margins (**Figure 14C**), with tumor cells intercalated into exocrine tissue; whereas invasive carcinoma type 2 (IC2) presents widespread invasion with no evidence of margins, with extensive intercalation of tumor cells into exocrine pancreas (Figure 15D) (Lopez and Hanahan 2002).

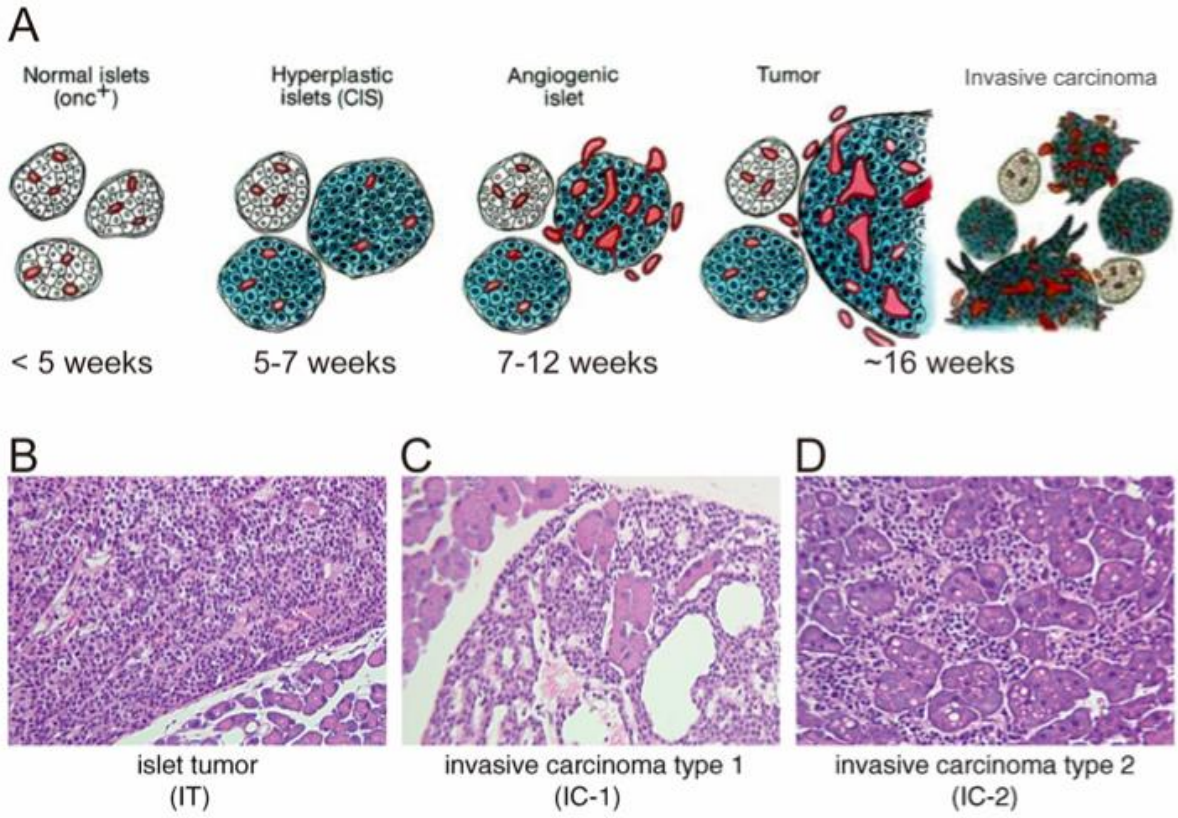

Figure 14. RIP1-Tag2 tumor progression. (A) Multistage cancer progression in RIP1-Tag2 mouse including: normal, oncogene-expressing islets; hyperplastic islets, populated by proliferating cells; angiogenic islets, in which new blood vessel growth has been activated; and solid tumors, which are islet cell carcinomas. Modified figure from (Hanahan and Folkman, 1996). **(B-D)** Malignant RIP1-Tag2 tumors classification. Hematoxylin and eosin stain of representative examples of IT (B), IC1 **(C)**, and IC2 **(D).** Modified figure from (Du et al. 2007).

6. Anti-angiogenic therapies

Tumor angiogenesis is thus defined as the process of blood vessel creation, penetration and growth in the tumor microenvironment. This process is critical to tumor growth beyond a limited size, granting oxygen, nutrients, and waste disposal, to thereby sustain the deregulated proliferation of tumor cells. Besides serving as nutrient, oxygen, and waste transport providers, vessels also facilitate dissemination of tumor cells to distant sites, promoting metastasis (Zuazo-Gaztelu and Casanovas 2018). Tumor angiogenesis is controlled by a balance of pro-and anti-angiogenic molecules and when the balance shifts in favor of angiogenesis inducers, an angiogenic switch activates the normally quiescent vasculature to develop new blood vessels (Hanahan and Folkman,

1996), often concomitant with enlargement (dilation and microhemorrhaging) of the preexisting vasculature (Ganss et al. 2002).

Despite the fact that PanNETs are highly heterogenous, the high vascularization is a characteristic common in all of these neoplasms. Thus, one of the approaches developed and tested for the treatment of well-differentiated NET tumors are anti-angiogenic strategies, in which the focus is to block some angiogenic factors and their receptors. In this anti-angiogenic context, vascular trimming occurs, and as consequence lack of nutrients, thus, leading to tumor cell death. Considering the quantity of mechanisms involved in tumor angiogenesis, blood vessel formation may be inhibited at different levels. Nowadays, growth factors and tyrosine kinase (TK) receptors are the main promising targets in angiogenesis inhibition, and, in fact, many drugs have been developed using these strategies (Zuazo-Gaztelu and Casanovas 2018).

It is important to mention that many anti-angiogenic drugs, such as bevacizumab and sunitinib, have been already approved by the US Food and Drug Administration (FDA) for the treatment of some of NET tumor types (Capozzi et al. 2016). Between them, sunitinib (Sutent®, Pfizer) promotes the inhibition of tyrosine kinase receptors involved in angiogenesis and expressed by endothelial and mural cells, such as VEGFR2, VEGFR3, PDGFR-α and PDGFR-β (Mendel et al. 2003). On the other hand, this drug also inhibits a set of receptors involved in proliferation and cell survival expressed in tumor cells, such as c-KIT (stem cell factor receptor), FLT3 (Fms-like tyrosine kinase 3) and CSF-1 (type I receptor of colony stimulating factor) (O'Farrell et al. 2003).

Sunitinib in RIP1-Tag2 tumors increases lifespan and delays tumor growth by reducing endothelial cell density and pericyte coverage of tumor vessels (**Figure 15**) (Pàez-ribes et al. 2010; Pietras and Hanahan 2005).

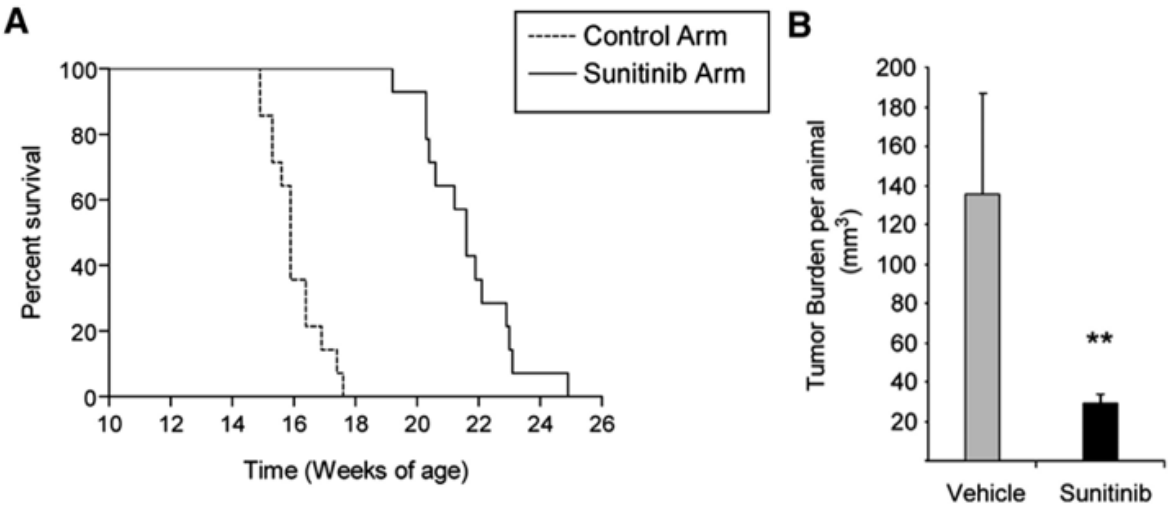

Figure 15. Increased lifespan and tumor reduction in sunitinib-treated RIP1-Tag2 animals. (A) Kaplan-Meier survival curves in tumor-bearing RIP1-Tag2 mice treated continuously with vehicle control or sunitinib starting at 12 weeks. While vehicle-treated mice showed a median lifespan of 15.2 weeks, mice receiving continuous sunitinib treatment demonstrated a survival benefit of 7 additional weeks. **(B)** Total tumor burden analysis of RIP1-Tag2 mice in 5-week treatment trials with sunitinib or vehicle control starting therapy at 10 weeks of age. **p < 0.01 by Mann-Whitney test. Error bars indicate ± SEM. Image has been adapted from (Pàez-ribes et al. 2010).

Sunitinib's effectivity in patients with advanced PanNETs was proved with a phase 3 clinical trial. As result the median progression-free survival in the sunitinib group increase to 11.4 months in relation to 5.5 months in the placebo group. In addition, enhancement in overall survival and the objective response rate improved 9% versus 0% in the placebo group (**Figure 16**) (Raymond et al. 2011). This data was especially important since there is a low number of effective treatments known for advanced PanNETs.

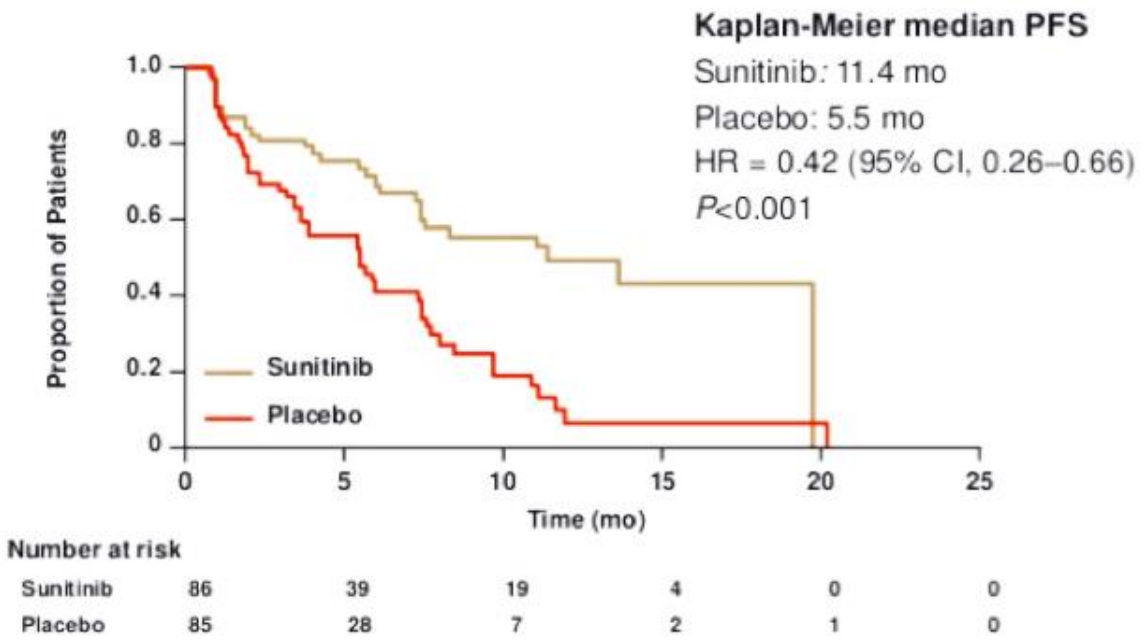

Figure 16. Progression-free survival by Kaplan-Meier analysis of in sunitinib Vs. placebo in treated advanced PanNET patients. Among 171 (86 patients who received sunitinib and 85 patients who received placebo), the median progression-free survival was 11.4 months in the sunitinib group versus 5.5 months in the placebo group. Image has been adapted from (Raymond et al. 2011).

6.1 Effects of anti-angiogenic therapies

Until now, many angiogenesis inhibitors have been described, nonetheless only a small part of them have been approved and applied in the clinic. The critical point is that antiangiogenics produce a progression delay with a limited period of clinical benefit, rather than providing enduring efficacy in tumor shrinkage or dormancy (Hanahan and Bergers 2008). Specifically, the clinical benefit of antiangiogenic drugs remains limited due to the acquisition of tumor drug resistance, and progression to stages of greater malignancy. Therefore, this strategy need to be improved to development of enduring antiangiogenic therapies, and thus, guarantee patient's long-term response (Zuazo-Gaztelu and Casanovas 2018).

Some years ago, the failure of anti-angiogenic therapy in RIP1-Tag2 model preclinical study was described. The initial efficacy revealed an initial response through of vascular dropout and tumor stasis, however tumors then adapt, acquiring resistance and begin regrowing via a process denominated to as

"evasive resistance", as demonstrated by tumor revascularization, regrowth and invasiveness (Casanovas et al. 2005). A time later, our group demonstrated that besides the phenotypic resistance to antiangiogenic therapies, an increase of the invasive phenotype in tumors also occurs under anti-VEGFR2 antibody (DC101) (**Figure 17A**) and angiogenic kinase inhibitor (sunitinib) (**Figure 17B**) treatments in RIP1-Tag2 tumors (Pàez-ribes et al. 2010).

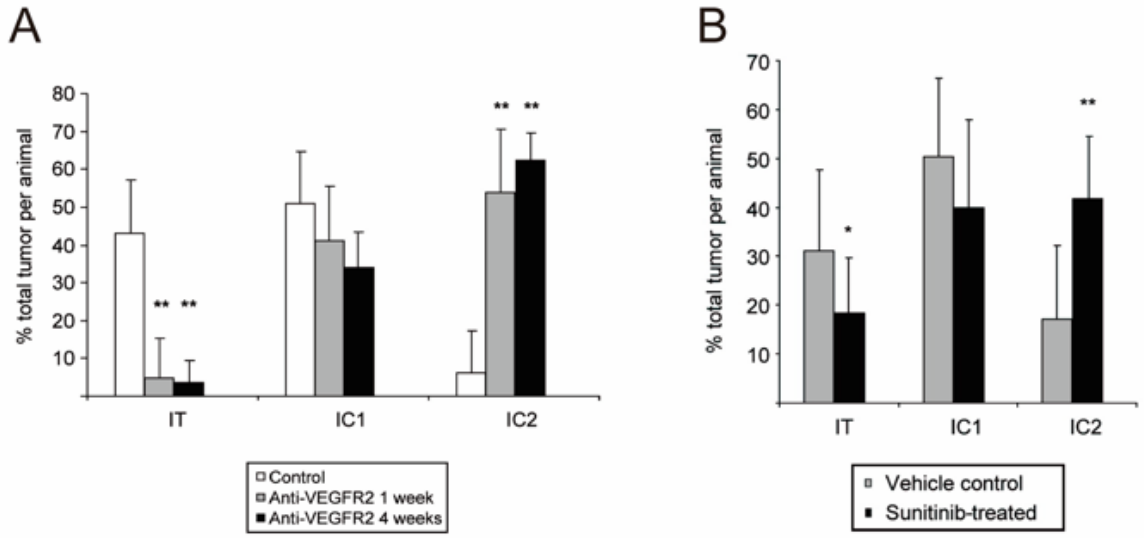

Figure 17. Increased invasive phenotype after anti-angiogenic therapy. Quantification of histological analysis of tumor invasiveness represented as the percentage of encapsulated islet tumors (IT), microinvasive carcinomas (IC1), and fully invasive carcinomas (IC2) for control, DC101 **(A)** and sunitinib **(B)** treated RIP1-Tag2 mice. **(A)** Both anti-VEGFR2 treatments show a statistically significant decrease in the percentage of IT and a significant increase in IC2 tumors ($**p < 0.01$ by Kruskal-Wallis test). **(B)** Sunitinib treatment shows statistically significant decrease in IT and increase IC2 tumors by Mann-Whitney test ($*p < 0.01$; $**p < 0.01$). Error bars indicate $\pm$ SD. Image has been adapted from (Pàez-ribes et al. 2010).

In order to verify other tumor malignization effects that could be identified after short-term treatment (2 weeks), histological analysis of lymph node (LN) was performed and liver metastasis after anti-angiogenic therapy. In this way, our group described that besides local invasion observed at acinar tissue, tumor cell invasion occurs into blood and lymphatic vessels, which consequently lead to an

increase in the incidence of lymphatic and hepatic metastases (Figure 18).

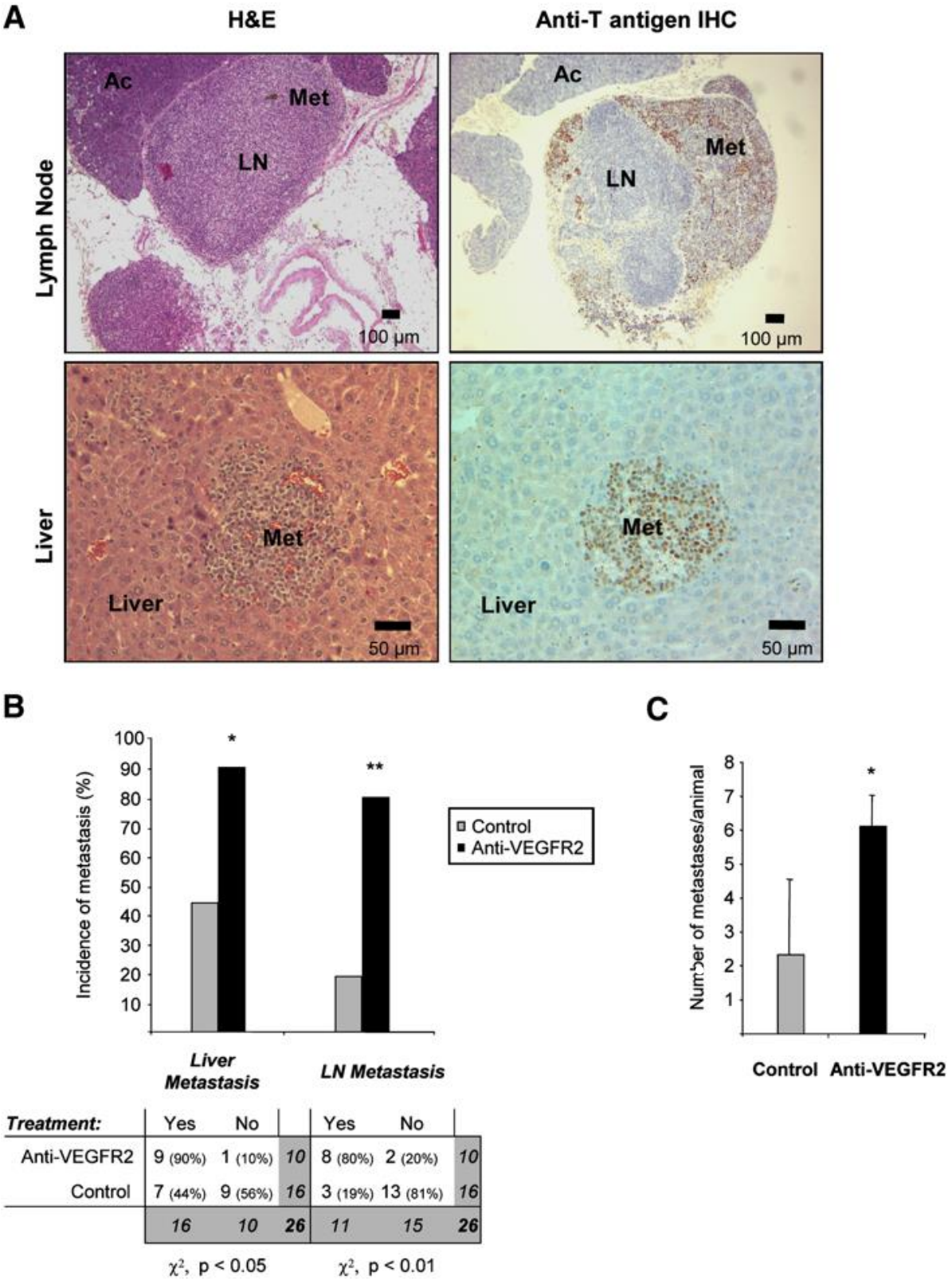

Treatment:	Yes	No		Yes	No	
Anti-VEGFR2	9 (90%)	1 (10%)	10	8 (80%)	2 (20%)	10
Control	7 (44%)	9 (56%)	16	3 (19%)	13 (81%)	16
	16	10	26	11	15	26
	χ^2, $p < 0.05$			χ^2, $p < 0.01$		

Figure 18. Increased incidence of lymph node and liver metastasis in DC101 treated animals. Histological analysis of lymph node (LN) and liver metastasis in RIP1-Tag2 animals treated with DC101 for 10 days starting at 10 weeks of age and then left untreated until 16 weeks of age. **(A)** LN

and Met observed by histological H&E staining of tissue sections from DC101-treated animals appear as enlarged hemorrhaging LNs infiltrated with tumor cells and a small tumor nodule in the liver parenchyma (left panels). Immunohistochemical staining for the tumor marker SV40 T antigen (brown) reveals the presence of tumor cells infiltrated into a LN or in the midst of the liver parenchyma (right panels). **(B)** Top: quantification of the incidence of animals with microscopic liver micrometastasis and macroscopic LN metastasis in the control (gray bars) and anti-VEGFR2-treated (black bars) treatment arms. Bottom: contingency table relating the number and percentage of animals in each treatment/metastasis case. Treated animals show a statistically significant increase in the incidence of liver micrometastasis and LN metastasis by the chi-square test ($*p < 0.05$; $**p < 0.01$). **(C)** Quantification of the number of microscopic liver metastasis in the anti-VEGFR2 treated (black bars) and control (gray bars) treatment arms. Treated animals show a statistically significant increase in the number of liver micrometastases per animal by the Mann-Whitney test ($*p < 0.05$). Error bars indicate $\pm$ SEM. (Pàez-ribes et al. 2010).

Knowing that there has been a demonstrated high correlation between tumor hypoxia, increased invasion, metastasis and poor patient outcome (Schindl et al., 2002; Semenza, 2002) was verified hypoxic levels in RIP1-Tag2 tumors treated with anti-angiogenics. As a result, the vascular trimming increased incidence of the hypoxic tumors in both anti-VEGFR2-treated and sunitinib-treated animals. Thus, confirming evidences that indicates tumor cells escape from lack of nutrients tumor environment to better nourished locations, using hypoxia as a positive stimulus for invasion (**Figure 19**) (Pennacchietti et al. 2003).

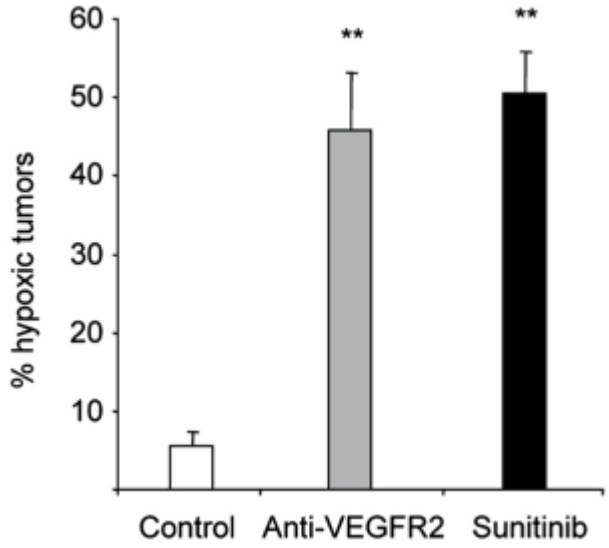

Figure 19. Increase of hypoxia in tumors as a consequence of anti-angiogenic treatment. Hypoxia in islet tumors was detected by immunofluorescence staining of pimonidazole adducts in sections of pancreas from control untreated animals, anti-VEGFR2 and sunitinib treatment. Quantitation of the incidence of hypoxic tumors was performed in long-term anti-VEGFR2-treated and sunitinib-treated animals and plotted as the percentage of pimonidazole-positive tumors per animal compared to control animals. $**p < 0.01$ by Mann-Whitney test. Error bars indicate $\pm$ SEM. Modified from (Pàez-ribes et al. 2010).

Taken together these results elucidate a tumor adaptive effect of VEGF/VEGFR inhibitors. Thus, tumors respond to VEGF/VEGFR pathway inhibition with tumor regression or stasis and a loss of blood vessels. However, processes of evasive resistance to the antiangiogenic treatment are then induced that can enable revascularization via alternative proangiogenic signals, increased local invasiveness, and/or enhanced distant metastasis (**Figure 20**).

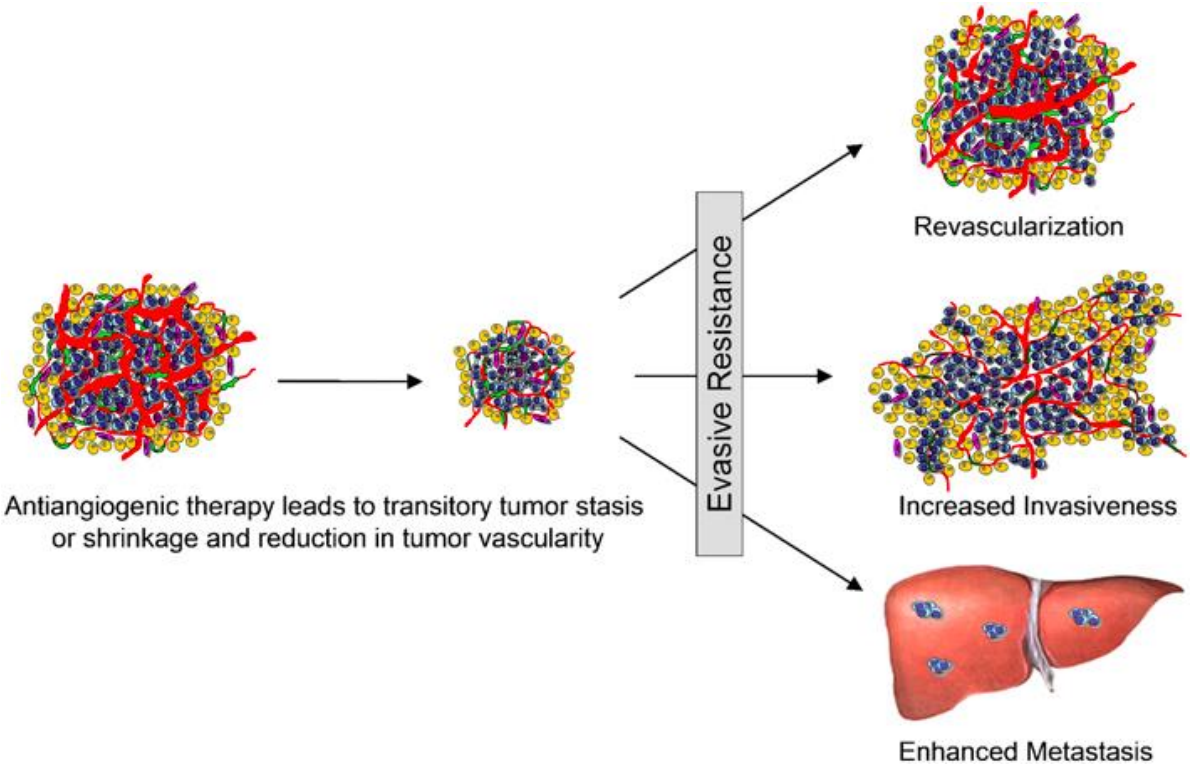

Figure 20. Adaptive-evasive responses by tumors to anti-angiogenic therapies. Image from (Pàez-ribes et al. 2010).

7. Previous results of the group

7.1 Invasion cancer cell mechanism after anti-angiogenic treatment

With the aim of clarifying which mechanisms are involved in invasion processes after anti-angiogenic therapy, the expression of some molecules that could act in the metastatic cascade step have been verified.

As detailed in the introduction (section 2.1) there are many invasion models in cancer. Among them, the most studied is the mesenchymal invasive phenotype, where cells increase their ability to invade by the EMT process. Molecularly, mesenchymal cell invasion is characterized mainly by loss of the E-cadherin protein, one of the main adhesion molecules and epithelial markers (Pàez-ribes et al. 2010). Also forming part of the adherent junctions is β-catenin, a protein that is generally sequestered in the cell membrane by E-cadherin, but in

the absence of E-cadherin, β-catenin remains free in the cytoplasm and able to be translocated to the nucleus and activate transcription factors that will ultimately favor the transcription of genes involved in survival, invasion and metastasis (Bienz and Clevers 2000).

Thus, E-cadherin and β-catenin expression levels were analysed after treatment with anti-VEGFR2 by immunofluorescence on frozen tissue (**Figure 21**). Surprisingly, it was observed that both proteins increased their expression after the anti-angiogenic therapy agents. This fact confirmed that there was no expected cadherin switch, since both proteins increased their expression.

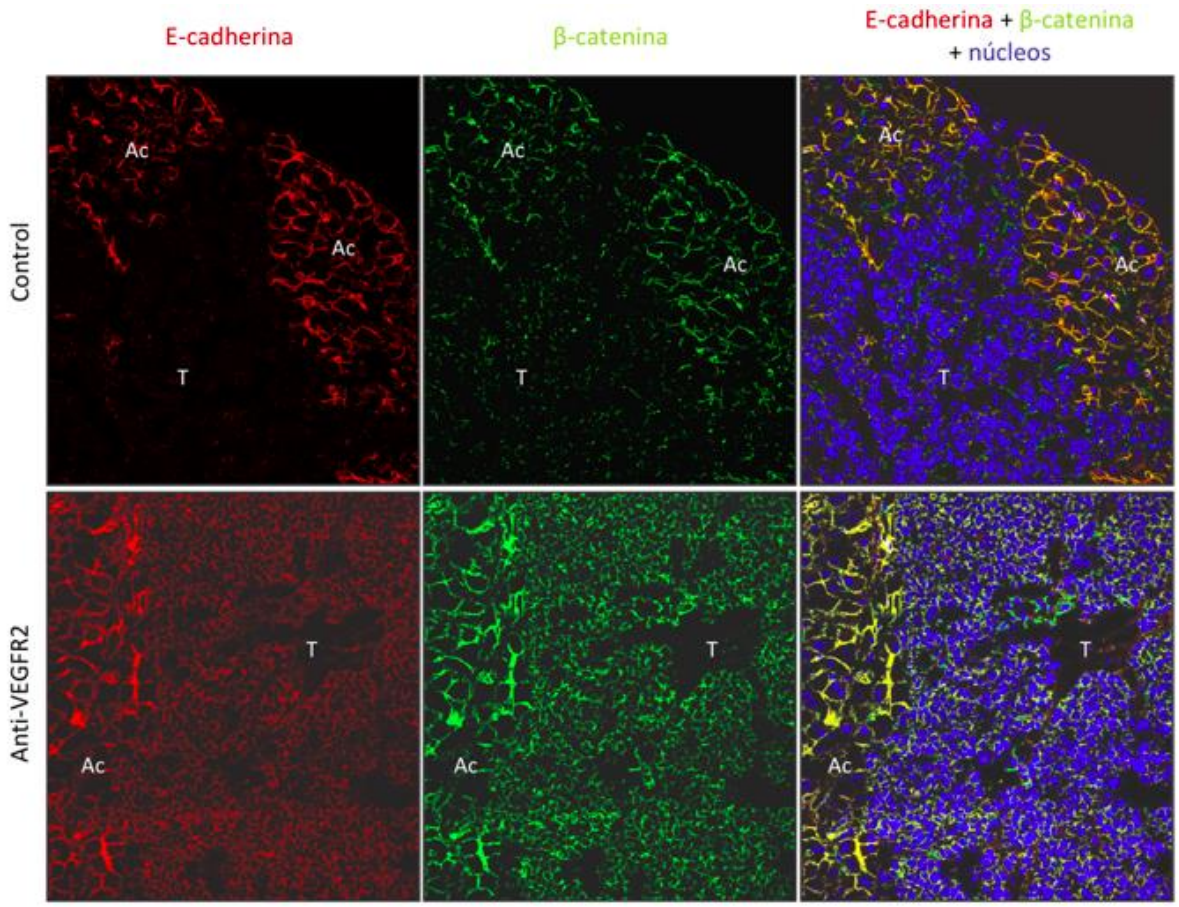

Figure 21. Increase of E-cadherin and β-catenin in treated tumors. Immunofluorescence showing an increase of E-cadherin and β-catenin proteins in tumors treated with DC101 for 4 weeks. The zones with the most intense marking correspond to acinar tissue, positive control of immunostaining. Ac = Acinar tissue; T = Tumor. Red marking: E-cadherin; green: β-catenin; blue: cores. Modified from Pàez-Ribes, 2010.

Since cell-cell junctions molecules remain intact or increase their expression in RIP1-Tag2 tumors after anti-angiogenic treatment, tumor invasion in this model does not seem to follow a classic EMT, however it seems to implicate mechanisms of collective tumor cell invasion. As described in detail in the first part of introduction (section 2.1.2), this is an alternative mechanism for tumor invasion in certain types of cancer, in which the cell-cell junctions are not lost.

In addition, the increase of E-cadherin described in RIP1-Tag2 tumors following treatment with anti-VEGFR2 was confirmed in tumors treated with sunitinib. In conclusion, it appears that the inhibition of angiogenesis promotes the same Behaviour and molecular changes in non-hemorrhagic phenotype tumors, either through an inhibitor via the VEGF pathway as DC101, or through a potent tyrosine kinase inhibitor such as sunitinib.

OBJECTIVES

Given the crucial role of tumor cell invasion in metastatic cascade, it is key to establish how alterations to the tumor cell-autonomous signaling circuitry promote invasive behaviour. Determining how tumor cells initiate and sustain invasive behaviour might help improve patient diagnosis and lead to the development of new intervention modalities. Previous results from our group demonstrated a significant increase in tumor invasion as an effect of pharmacological inhibition of VEGF/VEGFR2 in RIP1-Tag2 mouse model. In addition, these results indicate that pancreatic islet tumor cells treated with anti-angiogenic drugs invade collectively. However, collective cell invasion mechanisms have not yet been fully described.

The general objective of this thesis is to characterize and validate collective invasion mechanisms of PanNETs tumors before and after anti-angiogenic pharmacological effects.

To achieve this goal, our specific objectives are:

1) To characterize morphologically and molecularly collective invasive behaviour in RIP1-Tag2 tumors and βTC4 spheroids before and after anti-angiogenic treatment.

2) *To select potential candidate genes involved in RIP1-Tag2 tumor cell collective invasion before and after anti-angiogenic therapy.*

3) *To functionally validate our potential candidates in βTC4 cells and spheroids.*

4) *To validate our potential candidates identified in RIP1-Tag2 tumors and βTC4 spheroids in clinical samples of neuroendocrine cancer patients.*

1. Project design

Local invasion is a key cell-biological event in the metastatic cascade. In response to a changing microenvironment, cancer cells may act using two main strategies of invasion: single cell invasion and collective invasion. To elucidate which molecular mechanisms are involved in PanNETs invasion, we designed an experimental approach in which four steps are key to guiding this workflow (**i**) *in vitro* and *in vivo* PanNETs models identification, (**ii**) morphological and molecular PanNETs invasion characterization, (**iii**) selection of possible targets gene and (**iv**) target validation. Thus, in this section, I will summarize the experimental design applied at all stages of the project, whereas in the following sections the results will be described in detail (**Figure 22**).

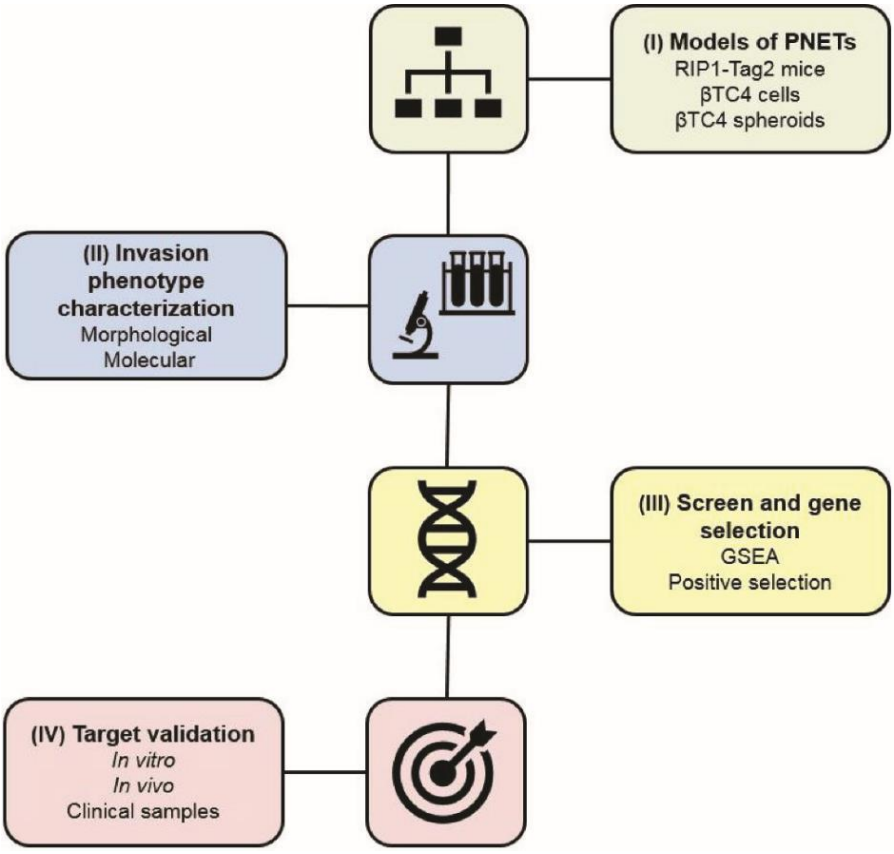

Figure 22. Project overview. Experimental workflow consisted in four main steps. **(i)** *in vitro* and *in vivo* PanNETs of models determination, **(ii)** morphological and molecular PanNETs invasion characterization, **(iii)** selection of possible targets gene and **(iv)** target validation.

Mouse models of human cancer are an indispensable tool for studying tumor initiation, maintenance, progression, and response to treatment. Among these, previous studies demonstrated that RIP1-Tag2 mouse model is a valuable prototype for verifying the stepwise progression of multistage tumorigenesis (Hanahan, 2015). For this reason, the RIP1-Tag2 mouse proved to be the most accurate choice for studying invasion in PanNETs. In the same way, we will use the βTC4 cell line derived from RIP1-Tag2 as *in vitro* model. Besides 2D βTC4 cells, other kinds of models like 2,5D and 3D models for verifying in detail the cell migration and invasion process will be developed.

Due to the different types of invasion observed in cancer, in the next step the malignancy observed in our models from PanNETs will be characterized morphologically and molecularly. To this end, *in vitro*, *in vivo* and clinical samples will be analysed by different techniques. For example, Transwell® and 3D invasion assay will be used for analyzing *in vitro* invasion, HE staining for verifying invasion *in vivo*. To identify the molecular mechanisms involved in this process will apply different protein and RNA detection methodologies.

In the screening step, the main goal will be to select genes involved with mechanisms of RIP1-Tag2 invasion before and after the therapy, in order to describe how tumor cells, initiate and sustain invasive Behaviour. For this, we will use GSEA analysis to compare samples from RIP1-Tag2 controls and highly invasive anti-angiogenic treated tumors. GSEA is a robust computational method that determines whether an a-priori defined set of genes shows statistically significant, concordant differences between both groups. GSEA analysis will thereby perform an association of functional profile of gene set collections pre-established with the input gene set from samples phenotypically characterized by tumor malignancy increase after anti-angiogenic treatment. Through a statistical test, it will be possible to observe an enriched functional gene set among the input genes.

In the last step, we will validate the targets relevance in the malignancy of PanNETs. We will perform a functional validation in *in vitro* and *in vivo* models

through protein and RNA levels using different techniques, and in clinical samples by omics analysis. Different treatments we will be used to functional induction and inhibition of our target. Finally, invasion assays will be used to confirm a role of our candidates in PanNETs malignancy.

MATERIALS AND METHODS

1. Animal procedures

Ethics Committee approved all animal studies realized in this work for Animal Experimentation from the Biomedical Research Institute of Bellvitge (IDIBELL) and Generalitat de Catalunya. Mice were maintained in Specific Patogen Free conditions, in constant temperature (20-22ºC) in ventilated racks and manipulated in vertical laminar flow hoods in IDIBELL- Hospital Duran I Reynals (AAALAC accreditation number 1155). The European directives on ethical usage of rodents for animal research (approval DARP #4899) were met in all animal experiments.

Mice were supplied of food and water ad libitum. Besides that, taking into consideration that β pancreatic tumor cells secrete high level of insulin was added sucrose to mice water to alleviate the severe hypoglycaemia that some animals can present. Animals were sacrificed by cervical dislocation or in case that physiological serum perfusion was required an overdose of the anesthetic Dolethal (pentobarbital sodium) was proceed.

1.1 Animal model

All experiments in this study were performed using RIP1-Tag2 of the C57Bl/6J strain. RIP1-Tag2 model have been used in several studies involving angiogenesis, tumoral progression and pharmacological effects. The generation and characterization of the transgenic RIP1-Tag2 mice (Hanahan, 1985) have been previously reported (detailed description in Introduction section 5).

1.1.1 Mice genotyping

RIP-Tag2 mice were obtained after crossing non-transgenic (wild type) females with RIP-Tag2 males. Weaning was performed at 3 weeks of age, in this moment all animals were sexed and marked for their subsequent identification. The remaining ear fragments were used to perform the genotyping. Pieces of the ear were immersed in digestion solution (50 mM Tris-HCl, pH 8; 20 mM NaCl; 1

mM EDTA, pH 8; 1% SDS; 2 mg/mL proteinase K (Sigma) and they were incubated at 65ºC during 4-12 hours. 300 µL of water were added and incubated at 95ºC for 10 minutes in order to inactivate proteinase K. For the PCR, in order to ensure optimal reaction, two pairs of oligos were used, one pair for the T antigen (Tag) and another pair for the endogenous control β2-globulin (**Table 1**).

Sequence of the oligos:

Table 1. Primers for RIP1-Tag2 mice genotyping and used in PCR reaction

Tag:	5' GCTCAAAGTTCAGCCTGTCC
	5' GGTGGGTTAAAGGAGCATGA
β2-globulina:	5' ATTCACCCCCACTGAGACTG
	5' TGGAGGAAGCTCAGGAAAGA

Reagents used for the PCR:
10X PCR buffer: 100mM Tris-HCL; 500mM KCl; 15 mM MgCl2
2mM dNTPs
Oligos (Tag and β2-globulin) 2.5 pmol/µl
Taq polymerase

Subsequently, the loading buffer is added to the samples and run in a 2% agarose gel stained with SYBR Safe. To rule out contaminations possibility in our PCR reaction is important to include a negative control water (H2O). Finally, samples with 2 bands pattern will correspond to transgenic RIP1-Tag2 mice (RIP1-TAG2) and those showing only one band (WT) will represent wild type mice (**Figure 23**).

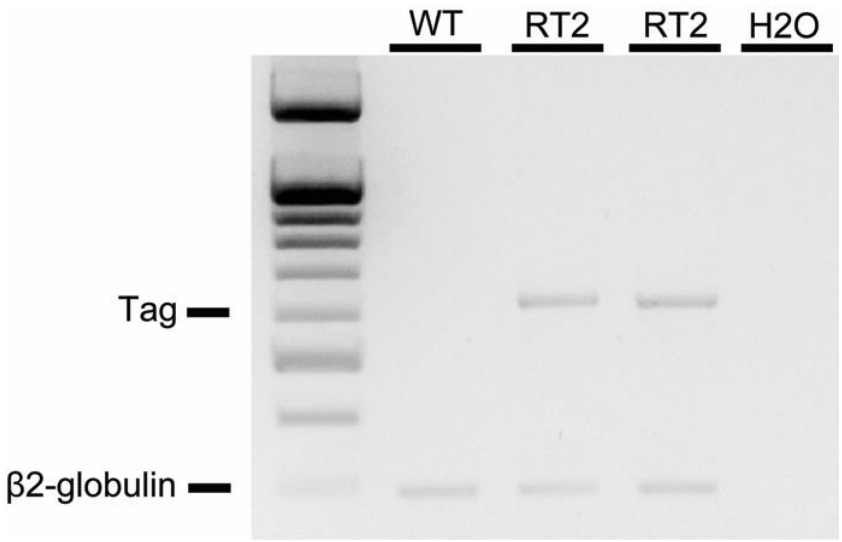

Figure 23. Agarose gel for RIP1-Tag2 mice genotyping. Double band pattern relative a RIP1-Tag2 transgenic mouse (RIP1-TAG2), a single band pattern from wild type mouse (WT) and a negative control of water (H2O).

1.2 Anti-angiogenic treatments

RIP1-Tag2 mice were treated with two different antiangiogenic drugs: sunitinib and DC101. Sunitinib was provided by Pfizer and dissolved in a solution of carboxymethylcellulose (CMC): 0.5% CMC, 1.8% NaCl, 0.4% Tween 80 and 0.9% benzyl alcohol (the pH was adjusted to 6). Mice were treated with 40 mg/kg of sunitinib daily orally for 4 weeks. DC101 is a anti-VEGFR2 blocking antibody that was obtained in bulk by purification from the supernatant of a hybridoma culture (DC101) available from *American Type Culture Collection* (ATCC). DC101 was administered at 1 mg/animal, twice a week through intraperitoneal injection, was performed a long (4 weeks) term treatment.

1.2.1 DC101 production and purification

DC101 was acquired from a cell culture of rat hybridoma seeded in bioreactors (CELLine CL 1000, IBS Integra Biosciences) using serum free medium Hybridoma-SFM (Gibco) mmented with glutamine 2 mM, 50 U/mL streptomicine, 1% nonessential aminoacids and 0,4% of glucose. The supernatant of the hybridoma, once per week, was collected and centrifuged at 3000 rpm for 15 minutes and filtered at 0,22 µm. BCA kit (Pierce) was used for

the protein quantification. To determine the quality of the antibody an electrophoresis with a 7,5% poliacrilamide gel was performed due to the fact that DC101 antibody has a high molecular weight (145 kDa). To preserve the disulfide bonds and be able to correctly evaluate the integrity of the DC101 obtained it is important once the sample buffer is added to the samples not to boil them or add β-mercaptoethanol. Finally, in order to check the quality of DC101 obtained by us, a known concentration of purified antibody was loaded, as weel as, a reference DC101 sample (commercial DC101 supplied by ImClone) and the gel was stained with Comassie Brilliant Blue.

1.2.2 Determination of the antiangiogenic effects

To establish the potency of anti-angiogenic treatment administered, was performed a tumor recount in lesions which presented antiangiogenic switch. In this way, all those lesions are classified in relation on hemorragic aspect observed, being tumors are classified in hemorrhagic (red color), partial hemorrhagic (pink color) and non hemorrhagic (white color).

1.3 Determination of survival time

The RIP1-Tag2 mice of the colony were distributed randomly in the different treatment groups starting at 12 weeks of age. Mice were sacrificed when they shown severe hypothermia or hypomobility.

1.4 Invasion determination

Paraffin embedded samples were H&E stained and used for the invasion morphological determinations because only formalin fixed, and paraffin embedded tissues preserve their morphology and allow studding the architecture of the tissue. The RIP1-Tag2 tumors were classified into encapsulated tumors, microinvasive tumors or highly invasive tumors (**Figure 24**) (Lopez and Hanahan, 2002).

A

Stage {Symbol}	Nucleus/cytoplasm ratio	Lesional size (compared to normal wt islets)	Vascular morphology	Margins with exocrine tissue
"Normal" Tag+ {N*}	Similar to wt β cells	Similar (<0.2 mm diameter)	Similar to wt islet capillaries	Well-defined, similar to wt islets
Hyperplastic/dysplastic islet {H/DI}	Increased relative to wt β cells	Variably larger (0.2–0.5 mm diameter)	Similar to wt islet capillaries	Well-defined, similar to wt islets
Angiogenic islet {AI}	Increased relative to wt β cells	Variably larger (<1 mm diameter)	Abnormal vessels appearing dilated and/or torturous; blood islands often evident	Well-defined similar to wt islets
Islet tumor or insulinoma {Tum}	Increased relative to wt β cells	Much larger (1–10 mm diameter)	Abnormal vessels appearing dilated and/or torturous; blood islands may be evident	Well-defined with no invasive regions; may or may not have a fibrous capsule and/or enveloped acinar islands or single cells
Invasive carcinoma type 1 {IC-1}	Increased relative to wt β cells	Much larger (1–10 mm diameter)	Abnormal vessels appearing dilated and/or torturous; blood islands may be evident	Focal regions of invasion with adjacent margins; tumor cells intercalated into exocrine tissue, and/or present as fronds projecting into normal tissue
Invasive carcinoma type 2 {IC-2}	Increased relative to wt β cells	Variable, from similar to normal islets up to large tumors, as above	Variable, from normal in small lesions to dilated and torturous in larger lesions	Widespread invasion with no evidence of margins; extensive intercalation of tumor cells into exocrine pancreas

B

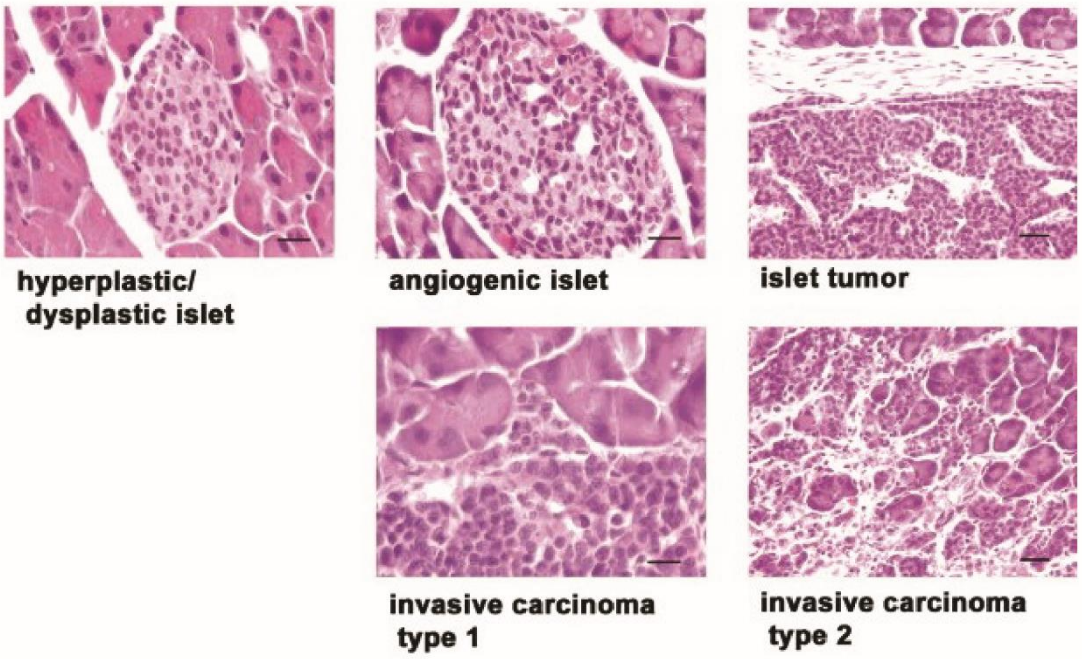

Figure 24. Morphology of the distinctive stages in islet carcinogenesis. (A) Staging criteria for H&E-stained pancreatic sections in mouse models of islet carcinogenesis. **(B)** Typical examples of the stages evident in the pathways to islet carcinogenesis are shown for standard RIP1-Tag2 mice. Scale bars represent 20µm on all micrographs except the islet tumor and invasive carcinoma type 2 in A, where the scale is 40 µm. From (Lopez and Hanahan, 2002).

1.5 Tumor and organ collection

After animals sacrificed tumor and other organs were washed with sterile water. One part of RIP1-Tag2 tumors was fixed in formaldehyde 4% O/N to be included in a cassette for paraffin embedding and in sequence these were washed with water and dehydrated (70% ethanol, 96% ethanol, absolute ethanol and xylol) and submerged in liquid paraffin at 60ºC. Then, remaining tumoral tissues were included in OCT (Tissue-TEK® Sakura) embedding medium at 80ºC for further analyses of frozen tissue. Some tumors originating from different animals were carefully isolated from the exocrine pancreas and frozen at 80ºC in order to perform RNA or protein extraction.

1.6 Histological studies

Paraffin embedded samples were hematoxylin and eosin (H&E) stained and used for morphological analysis, invasion quantification and specific immunostaining because only formalin fixed and paraffin embedded tissues preserve their morphology and allow studding the architecture of the tissue.

Paraffin sections (3-5µm) deposited into poly-L-lysine pre-treated slides and cut by microtome were subjected them to a deparaffinization battery (**Table 2**).

Table 2. Sequence of deparaffinization battery

Quantity	Reagent	Minutes
4	Xylene	10
3	Absolute ethanol	5
3	Ethanol (96%)	5
1	Ethanol (70%)	5
1	Ethanol (50%)	5
1	dH2O	10

Then, samples were stained with H&E. Slides were submerged for 10min in Hematoxilyn and rinsed in tap water. Following, they were submerged in HCL 1% until the tissue color shifted to red and then in ammonia water solution (200ml

of dH2O with 1ml of ammonia 30%) until it turned back into blue. Sections were counterstained in eosin (2.5 g of eosin in 1L of ethanol 50%) for some seconds.

At the end, slides were covered with coverslips and mounted using DPX (Merck). All tissues were visualized and photographed using the Nikon Eclipse 80i microscope and a Nikon DS-Ri1 digital camera by NIS-Elements BR 3.2 (64-bit) Software. Afterwards, images were optimized and analysed with Image J Software.

2. Protein analysis of tumor samples

2.1 Immunohistochemistry

Besides H&E stained were also performed immunohistochemistry to detect CDH1, CLDN4, fibronectin, cadherin-7 following the same protocol. Firstly, paraffin-embedded tumor samples were deparaffinised in xylene and rehydrated in graded alcohols (section 1.6). Subsequently antigen retrieval was performed with in sodium citrate solution (0.38mg/ml) pH=6 and heating for 15min. Then, samples were cooled down inside the citrate solution for 20-30min and washed with dH2O for 5min.

The endogenous peroxidases were activity blocked with double incubation with 3% hydrogen peroxide for 15min. Later samples were washed with dH2O for 5min and cell membranes were permeabilized with PBS 0.1% triton (PBST) for 5min. Afterwards, in order to reduce the unspecific unions slices were incubated during 1h at RT with a protein-blocking solution (normal goat serum diluted 1:5 in PBS) and primary antibodies (**Table 3**) were used for specific tissue immunostaining and the incubation of all of them was an o/n incubation at 4ºC.

Table 3. List of antibodies used for immunohistochemistry

Antigen	Reference	Species	Dilution	Supplier
E-cadherin	3195	Rabbit	1/100	Cell Signaling
Claudin-4	NB100-91712	Rabbit	1/500	Novus Biologicals

In the next day, sections were placed at RT for 20-30min and were washed three times with PBS 1X for 10min. After that, samples were incubated with secondary antibodies anti-mouse or anti-rabbit Envision+-System-HRP (Dako) during 1 hour at RT. Finally, slices were revealed with the chromogenic substrate DAB+ (EnVision™ Kit, Dako), from 30s to 10min, depending on the antibody and the samples used, until a brown precipitate appeared. The reaction was stopped by rinsing the slides with tap water for 10min. After, sections were counterstained with haematoxylin and dehydrated in graded alcohols. Then slices were mounted using DPX (Merck) and were covered with cover slips. The subsequent analyses were realized with method describe in the section 1.6.

2.1.1 CLDN4 and CDH1 immunohistochemistry quantification

First of all, different tumoral zones were determined in three levels, tumor center, invasive front and encapsulated front. Following, was determined CLDN4 staining intensity by scoring from 0 to 2 for each tumoral zone. The values were plotted using tumor zone data relating with their intensities. In the second methodology applied, were determined the percentage of global tumor invasion and these levels were correlated with the CLDN4 average intensity observed in all tumoral zones.

In order to determine CDH1 intensity the same method to CLDN4 quantification was used. However, the only difference between both was that in CDH1 quantification were considered just periphery zones, being classified in invasive front and encapsulated front. The relations posteriorly applied were the same used in CLDN4 intensity determination.

2.2 Preparation of protein lysates from tumor tissues

Tumor tissue was unfrozen on ice to prevent degradation by proteases and was placed in Tissue Grinder Potter-Elvehjem (TGPE) to further homogenization. The TGPE is graduated glass tube and a finely machined pestle, in which the pestle is attached to a stainless-steel shaft and homogenization occurs as the sample and buffer are forced through the cylindrical portion of the mortar as the pestle rotates downward. Thus, sample was homogenizing using TGPE with 400µl RIPA lysis buffer (**Table 4**, pH 7.4) same minutes and the lysate was transferred into a 1.5ml Eppendorf. It was incubated in rotation during 30-40min at 4ºC. At the end, sample lysate was centrifuged at 14000rpm for 15min at 4ºC and supernatants were stored at -20ºC.

Table 4. RIPA lysis buffer composition

RIPA lysis buffer
0.1% SDS
1% NP-40
0.5% sodium deoxycholate
50mM NeF
5mM EDTA
40mM β-glycerolphosphate
200µM sodium orthovanadate
100µM phenylmethylsulfonyl fluoride
1µg/ml leupeptin
4µg/ml aproptin in PBS

2.3 Protein quantification

Protein concentration of protein supernatants was determined using Pierce™ BCA Protein Assay Kit (Thermo Scientific). For acquire a stand curve was diluted Bovine Serum Albumin (BSA) in a set of diluted standards ranging from 0 to 2mg/ml and samples were diluted (1:10). Afterwards, was prepared a BCA Working Reagent, it was diluited (50:1, Reagent A: B) and loaded onto a 96-well plate. Then, of the known diluted concentrations of BSA or diluted samples (10µl) were loaded on plate. It was incubated at 37ºC for 20-30mins and then

absorbance was measured at 560nm by spectrophotometry (Power Wave XS, BIO-TEK) using the KCJr Win Software.In this way, protein concentration was calculated by extrapolation in the BSA standard curve.

Finally, lysates were mixt with loading buffer (**Table 5**) at a final concentration of 1:4 and were incubated 5min at 95°C to contribute with denaturalisation already started for the presence of SDS and β-Mercaptoethanol. The final blend was stored at -20ºC.

Table 5. Loading buffer elements

Loading buffer
300mM Tris-HCl pH 6.8
600mM DTT
12% SDS
0,6% bromophenol blue
60% glycerol
5% β-Mercaptoethanol

2.4 Western blotting

In order to separate proteins by size was applied Sodium dodecyl sulphate polyacrylamide gels (SDS-PAGE) technique. To meet its goal SDS-PAGE technique has two-phase gels: the stacking and the resolving gel (**Table 6**). The stacking gel is responsible to stacks the proteins to enter into the resolving gel. On the other hand, the resolving gel is responsible for separating proteins by their molecular weight. Thus, depending on the molecular weight of the protein of interest the acrylamide percentage is variable (from 7.5 to 12%).

Table 6. Western blotting gels composition

Stacking gel	Resolving gel
125mM Tris-HCl pH 6.8	9,4M Tris-HCl pH 8.8
4% acrylamide	variable % acrylamide
0,1% SDS	0,1% SDS
1% ammonium persulfate (APS)	1% ammonium persulfate (APS)
0,1%Temed	0,1%Temed

The wells of SDS-PAGE were carefully loaded with 30µg of protein into gel along with a molecular weight marker (Page RulerTM prestained, Thermo Scientific) into running buffer 1X (**Table 7**). After that, protein samples were submitted to electrophoresis at 100V for 60min to 120min. Then, the acrylamide gels were transferred to a nitrocellulose membrane (Immobilon-P, Merck Millipore) at 100V for 120min that was previously activated with methanol.

Table 7. Running buffer compounds

Running buffer 1X
25mM Tris-HCl pH 8.3
192mM Glicin
17 mM SDS

The membrane was blocked with 5% skimmed milk in TBS (Tris 50mM, NaCl 150mM) for avoiding unspecific bindings. Then, membrane was incubated with primary antibodies in TBST 1% skimmed milk in appropriate dilutions (**Table 8**) O/N at 4°C.

Table 8. List of primary antibodies used for western blotting

Antigen	Reference	Species	Dilution	Supplier
E-cadherin	3195	Rabbit	1/1000	Cell Signaling
Fibronectin	ab2413	Rabbit	1/150	Abcam
Vimentin	180052	Mouse	1/2000	Invitrogen
Claudin-1	sc-166338	Mouse	1/250	Santa Cruz Biotechnology
Claudin-1	sc-81796	Mouse	1/250	Santa Cruz Biotechnology
Claudin-4	NB100-91712	Rabbit	1/250	Novus Biologicals
Claudin-4	36-4800	Rabbit	1/1000	Thermo Fisher Scientific
Claudin-5	sc-374221	Mouse	1/250	Santa Cruz Biotechnology
Claudin-9	sc-398836	Mouse	1/250	Santa Cruz Biotechnology
Claudin-11	sc-271232	Mouse	1/250	Santa Cruz Biotechnology
Claudin-19	sc-365967	Mouse	1/250	Santa Cruz Biotechnology

The following day, membranes were washed three times, 10 min each, shacking with TBS- 0.1% Tween 20 (TTBS) and then, blots were incubated with secondary antibodies (**Table 9**) in 1% skimmed milk in TBS for 1 hour at RT and more one-time blots was washed thrice with TBST.

Table 9. List of secondary antibodies used for western blotting

Antibody	Species	Dilution	Supplier
Rabbit HRP	Goat	1/5000	GE Healthcare
Mouse HRP	Goat	1/5000	GE Healthcare

In order to verify if the antibody was hybridized to the protein of study, the membrane was incubated with an Amersham ECL Select™ Western blotting detection reagent (GE Healthcare Life Sciences) according to manufacturer's instructions and exposed ChemiDoc System (Bio-Rad). Finally, protein quantification was performed through densitometry analysis of bands intensity was performed using Image Lab software (Bio-Rad).

3. Molecular analysis of tumor samples

3.1 RNA extraction

Once mice sacrificed the tumors were collected and the surrounding acinar tissue was carefully removed. Afterwards, tumors were placed in Eppendorfs, homogenized manually and RNA was extracted with RNeasy Plus kit (Qiagen) following the manufacturer's instructions. Obtained RNA was quantified in the

spectrophotometer NanoDrop TM1000 (Thermo Scientific). To validate the RNA obtained was loaded a 500ng of RNA in a 1% agarose gel using a 1Kb Plus DNA ladder (Invitrogen). Contaminated with samples gDNA were treated with DNA-freeTM DNA removal kit (ThermoFisher Scientific), following manufacturer's instructions. Finally, the RNA obtained was quantified in the espectophotometer NanoDrop TM 1000 (Thermo Scientific).

3.2 Obtention of cDNA from mRNA

The mRNA samples with 20µl mix composed of 2µg of RNA together with Mix RT-PCR were converted into cDNA using the High Capacity cDNA Reverse Transcription kit (Applied Biosystems). For this, 10µl of this Mix RT-PCR was added to each cDNA sample and the reverse transcription reaction was performed with the following conditions (**Table 10**)

Table 10. Mix RT-PCR components and PCR conditions for convert cDNA in mRNA

Mix RT-PCR
3µl RT buffer
3µl Random primers
1,2µl dNTPs
1µl Reverse Transcriptase
0.8µl Sterile water
1µl RNAse inhibitor

Thermocycler program	
25ºC	10min
37ºC	120min
85ºC	5min

Obtained cDNA was stored at -20ºC until use.

3.3 Real-Time Quantitative PCR (RT-qPCR)

In order to determine an expression level of our interest genes we performed a Real-Time PCR technique. RT-qPCR is a PCR in which amplification products number are known. First of all, plate was loaded with 5µl of TaqMan® Universal PCR Master Mix (Applied Biosystems), 25ng cDNA obtained from different tumor tissues, 0.5µl of the Taqman® Probe of interest (table W) and ddH20 to a final volume of 10µl. The plate was read on a HT7900 Real-Time PCR System (Applied Biosystems) following the program (**Table 11**):

Table 11. Real-Time PCR conditions

Stage	Temperature	Time
1	50ºC	2min
2	95ºC	10min
3	95ºC	15sec
	60ºC	1min

Obtained results were visualized analysed by RQ Manager and SDS 2.4 softwares (Applied Biosystems).

Results from amplification curves are calculate by the Ct (threshold cycle). Ct is the cycle in which the fluorescence over the background is significant, being inversely proportional to the copy number. In this way, the final number of cycles detected for fluorescent signal for each gene was normalized against the same value of the housekeeping gene, being in this thesis the *ACTB* gene. To calculate a final value of RNA expression was applied the following formula:

$$2^{-\Delta Ct} = 2^{-(Ctgene\ A - Ct\ housekeeping\ gene)}$$

4. Cell culture techniques

In this work, βeta Tumor Cell 4 (βTC4) cell line was used in all *in vitro* experiments. βTC4 cell line was isolated from RIP1-Tag2 tumors in Hanahan laboratory and maintained in DMEM (Lonza), 15% FBS supplemented with 1% nonessential aminoacids, 1% piruvate and 100 µg/mL penicillin-streptomycin (all from Life Technologies). SN12C and Ren13 cell lines were also used as protein positive controls markers when it is needed (**Table 12**).

Table 12. List of cell lines used in this thesis

Cell line	Disease	Medium
βTC4	Pancreatic Neuroendocrine Tumor	DMEM (15% FBS)
SN12C	Renal Cell Carcinoma	DMEM (10% FBS)
Ren13	Renal Cell Carcinoma	RPMI 1640 (10% FBS)

SN12C and Ren13 cell lines have human kidney tissue origin. SN12C was provided F. Setién and Manel Esteller from the cell culture facility of the Cancer Epigenetics and Biology Program (PEBC) and was cultivated in DMEM (Lonza),

10% FBS with 50U/ml of penicillin, 50µg/ml of streptomycin sulfate, 2mM of L-glutamine, 10mM of HEPES, 1% pyruvate and 1% of non-essential aminoacids (**Table 13**) (all from Gibco, Life technologies). Ren13 renal cell carcinoma is a primary cell line previously established in our group maintened in RPMI 1640 (Gibco), 10% FBS, 10ng/ml EGF (Bionova), 0,72 ug/ml insulin (Lilly) and supplemented as SN12C.

Table 13. Media used for cell culture

Medium	Reference	Manufacturer
RPMI Medium 1640	31870-025	Gibco (Thermo Fisher Scientific)
Dulbecco's Modified Eagle Medium (DMEM)	BE12614F	Lanza

4.1 Mycoplasma test

In order to check mycoplasma contamination was performed routinely PCR in all cell lines using the oligonucleotides (**Table 14**). As a template for the PCR, media from cells, which had been in overconfluence and absence of antibiotics for, at least 5 days were used. If the result was positive, cells were treated with PlasmocinTM at 25µg/ml for 2 weeks, and then cells were tested again for contamination.

Table 14. Primers for the detection of mycoplama

Oligonucleotide	Sequence
MICO-1	5'- GGCGAATGGGTGAGTAACACG-3'
MICO-2	5'-CGGATAACGCTTGCGACTATG-3'

4.2 Cell freezing and cryopreservation

βTC4 cells were washed with PBS, resuspended in culture medium and transfer into a 50 mL falcon tube, in other cell lines we performed the trypsinization in this moment. After, cells were centrifuged for 5 min at 1,250 rpm at room temperature and was removed the supernatant and loosed the pellet gently. Cells of a p100 plate were resuspended in cold freezing medium (90% FBS plus 10% DMSO (Sigma) without dilution, already renal cells were diluted in ½ or ⅓, depending on the cell line.

Cell suspension was transferred in cryovials at 1ml/tube and put into a -80°C freezer. In this process, we used a container that will ensure that the temperature decreases steadily by 1°C/minute. After 24h, we transferred the cryovial into liquid nitrogen for long-term storage.

To cell thawing, the cryovial containing the frozen cells was removed from liquid nitrogen and quickly place it into 37°C water bath (< 1 minute). After, cells were diluted in prewarmed medium, trespassed to a 15ml falcon tube and cells were centrifuged for 5 min at 1,250 rpm at room temperature. Finally, cells were gently resuspended in complete fresh medium and transferred them into the p100 plate with recommended culture environment.

4.3 βTC4 spheroids

Cellular aggregates from βTC4 spheroids were spontaneously generated during the 2D in vitro culture of βTC4 cells, these aggregates were denominated βTC4 spheroids. βTC4 spheroids were cultivated in the same conditions that βTC4 cells with DMEM (Lonza), 15% FBS supplemented with 1% nonessential aminoacids, 1% piruvate and 100 µg/mL penicillin-streptomycin (all from Life Technologies) onto a p100 plate. To select spheroids by size, spheroids plates were washed with PBS and after spheroids were resuspended in culture medium and filtered with cell strainer (Corning) of 40um and 70um depending on the goal of the assay.

4.3.1 2,5D *in vitro* model

In order to obtain 2,5D *in vitro* model, plate of 24 wells were coated with Collagen I (Corning), Gelatin (Life Technologies), Laminin (Corning), Collagen IV (Corning) and Matrigel® (Corning) and the plate was incubated at 37ºC for 1 hour. After, wells were washed with PBS, then βTC4 spheroids suspension was seeded into plate and βTC4 spheroids seeded were covered with 1ml of culture medium.

4.3.2 3D *in vitro* model

A 3D model of βTC4 spheroids was established by using Matrigel® matrix Growth Factor Reduced (Matrigel® GFR, Corning) so as to better mimic the *in vivo* conditions in RIP1-Tag2 tumors. Matrigel® GFR is primarily composed by laminin, followed by collagen IV and heparan sulfate proteoglycans. Thus, it effectively mimics the extracellular matrix of most tumors. Regarding 3D model generation, a βTC4 overconfluent p100 plate is equally handled, using a 70 μm nylon cell strainer (Falcon Corning) to exclude smaller spheroids. Retained spheroids are collected in a 15 ml Falcon tube and allowed for physical decantation for 2-4 minutes. Spheroids at the bottom are placed in an Eppendorf, diluted 1:10 in fresh βTC4 media, and they are ready to use.

When growing the isolated spheroids within a 3D matrix, 30 μl of cool liquid Matrigel®® were placed in each well of a 24 well plate. Importantly, at this time heat a little bit under the plate, to prevent the spheroids falling to the bottom of the drop. Then, 5 μl of previously filtered spheroids were added to the gel in a drop and were gently mixed, avoiding bubble formation. We repeated this process once more and when we got a correct confluence the plate was incubated at 37°C during 30min. Finally, was added 1ml of medium cell culture in each well and renewed every 3-4 days. Finally using an inverted microscope (Leica DMi1), was verified a correct spheroids confluence and position into Matrigel®.

4.3.3 Spheroid harvesting procedure

In 3D model, in order to allow for harvesting of intact spheroids for protein analyses was applied Trevigen's Cultrex® Organoid Harvesting Solution. This solution provides a non-enzymatic method for depolymerizing extracellular matrix proteins.

Thus, on ice were aspirated the cell culture media and spheroids plates were washed with cold PBS (4ºC) carefully for not to disrupt basement membrane matrix containing organoids. After, 100μl for each 10ul of Matrigel® of Organoid Harvesting Solution were added in the plate. Subsequently, the plate was

incubated at 4 °C for 30 – 90 minutes with moderate shaking. This incubation was complete when the basement membrane matrix dome was no longer visible at the bottom of the well and the organoids may be seen floating at the bottom of the well.

Once the gel depolymerizes, contents were transferred to 15 ml or 50 ml conical tube and spheroids were centrifuged 600RPM for 15 minutes at 4 °C. After centrifugation, was aspirated the supernatant and was reserved the pellet contained isolated organoids. Using this pellet from *in vitro* 3D model of βTC4 spheroids is possible to cryopreserve spheroids, as well as, develop processes for biochemical analysis (such as RT-PCR, MS-PCR, sequencing, Western Blot, ELISA, or IHC).

4.4 Cell treatments

4.4.1 Hypoxia and nutrient deprivation

βTC4 cells and spheroids were routinely maintained in normoxia at 21% O_2, 5% CO_2, 37°C a full medium (100% nutrients). Furthermore, in order to mimic *in vitro* the anti-angiogenic treatment, cells and spheroids were cultured under the following conditions: hypoxia at 3% or 10% O_2, 5% CO_2, 37°C, different levels of dilution media in PBS1X or variable percentage of FBS (**Table 15**) all for 24 hours.

Table 15. βTC4 cell treatment

Nutrient deprivation conditions
Normoxia; 5% FBS
Normoxia; 0% FBS
Normoxia; 25% nutrients
Normoxia; 50% nutrients
Hypoxia 10%; 25% nutrients
Hypoxia 10%; 50% nutrients
Hypoxia 10%; 75% nutrients
Hypoxia 3%; 15% FBS
Hypoxia 3%; 50% nutrients

4.4.2 Y201636 treatment

βTC4 cells and spheroid were treated with YM201636 inhibitor in order to block CLDN1 functionally. YM201636 inhibit constant recycling of claudin-1, that as a consequence it to accumulate intracellularly. YM201636 is a potent inhibitor of mammalian phosphatidylinositol phosphate kinase PIP5KIII (PIKfyve). PIKfyve is the sole enzyme for PtdIns(3,5)P2 biosynthesis that regulates a number of intracellular membrane trafficking pathways.

This drug has been demonstrated effectively to block CLDN1 *in vitro* at 400nM, in both 2D and 3D model the concentration of Y201636 was of 400nM (one dosis). To verify cell morphology and viability, cells were treated and analised 24 hours after, respectively, by photos taken using an inverted microscope (Leica DMi1) and trypan blue assay.

4.5 Migration assay in 2,5D model

βTC4 spheroids were seeded in the coatings using the protocol described above (section 4.3). Then, for the spheroid adhesion to the coating, plate was placed was at 37°C for 3h. After these hours, using a microscope, spheroids to be studied were manually marked and photos were taken using an inverted microscope (Leica DMi1), spheroids were manually counted. In order to observe cell migration movement, photos of marked spheroids were also taken at 24h and 48h.

In the time-lapse experiment using a 2,5D model, the spheroids were seeded in 24 wells plate previously coated with Matrigel®, laminin. After two hours, the plate was positioned to take photos each 20 minutes during eight hours of spheroids selected. All time-lapse assay was using the objective 10X and Zeiss Apotome microscope.

4.6 Invasion assays

4.6.1 Transwell® invasion assay

To compare an invasion capacity of βTC4 cells we performed a Transwell® assay βTC4 cells (5.0 x 10^5 cells/mL) in 250ul of βTC4 DMEM medium were placed in in the 6.5 mm inserts of the Transwell®® Permeable Supports (Corning) containing a 8 µm polycarbonate membrane. At the bottom of the well, also 750 µl of pre-warmed βTC4 DMEM medium. Cells were maintained in normoxia at 21% O_2, 5% CO_2, 37°C.

βTC4 cells were treated according the objective in detail described in Results section. However, the last part is the same in all assays. Thus, after Transwell® chamber be incubated for 24h/48h, for the purpose of analysis remove non-invading cells the inserts were removed, wiped with a cotton swab on the lower part of the chamber. The membrane was fixed with methanol, washed with PBS 1X and stained with hematoxylin (0.1% Hematoxylin, Merck Millipore, in ethanol 96%) all steps for 2 minutes.

At the end, the membrane from inserts was removed and mounted with water on a slide. Using a Nikon 80i microscope and Nikon DS-Ri1 digital camera were taken some 20-25 representative fields at 20x magnification. Photos were processed and analysed with NIS-Elements BR 3.2 (64-bit) Software and Image J Software. All control and experimental groups performed in parallel and in duplicates or triplicates

4.6.2 3D spheroid invasion assay

A major advantage of 3D spheroid invasion assay is that we can verify the collective invasion capacity of a deeply manner contemplating all its aspects. For this, first of all was necessary to establish an *in vitro* 3D model as described above (section 4.3.2). After 24h of the spheroids already in Matrigel® manually using the microscope an inverted microscope (Leica DMi1), spheroids were manually counted and marked. In this moment, the protrusions resulting from the collective

invasion were quantified by each spheroid under analysis, was made a mean among all spheroids analysed by condition.

The analysed spheroids have a *n* of 25-90 spheroids per condition. This quantification process was repeated every day of the assay. In the last day of the experiment, (day 7) spheroids already have an extreme invasion increasing the risk of the incorrect quantification of the protrusions. Thus, the quantifications analysed were until the three or sixth day of experiment.

4.6.2.1 YM201636 treatment in 3D model

To verify CLDN1 block effect in 3D model, we performed a 3D model methodology described in the section 4.3.2. Then, in the day 0, βTC4 spheroids were treated with YM201636 at 400nM. The strand per spheroid quantification was performed at day 0, 1 and 3.

5. *In vitro* protein detection

5.1 Immunocytofluorescence

5.1.1 2D model

The first step realized was to treat coverslips with ultraviolet radiation during 1-2 hours to sterilization and after placing it in a 24 well plate. βTC4 cells were resuspended in 5ml of full medium and 150ul of this suspension was seeded on a plate. The plate was maintained in normoxia at 21% O2, 5% CO2, 37°C a full DMEM medium (15% of FBS) during 24-72h until reached a correct confluence (80%).

Then, wells were washed with PBS and fixed for 8min with 4% Paraformaldehyide (PFA). Subsequently, cells were washed three times with PBS and permeabilized during 15min with PBS-0.1% Triton (TPBS). In order to prevent unspecific binding of primary antibody, cells were blocked with 20% serum of the species of secondary antibody (normally goat serum) in PBS for 30min at RT.

Afterwards, cells were incubated with primary antibodies at the corresponding dilution (**Table 16**) in blocking solution for 1h at RT and were washed twice with PBS. Then, secondary antibodies diluted 1/200 also with blocking solution for 1h at RT was applied. Furthermore, all incubations were performed in a humidity chamber and was used parafilm for tighten the coverslips over the drops.

Finally, cells were washed with PBS thrice more and incubated for 10min in RT with DAPI to perform nuclear staining. Slides were mounted using FluoromountTM Aqueous Mounting Medium (Sigma)and Cells were observed using Nikon Eclipse 80i microscope, images were taken by Nikon DS-Ri1 digital camera using NIS-Elements BR 3.2 (64-bit) Software and were analysed using Image J Software.

Table 16. List of primary antibodies used for immunocytofluorescence

Antigen	Reference	Species	Dilution	Supplier
E-cadherin	610404	Mouse	1/100	BDBiosciences
Ki67	RM-9106-s1	Rabbit	1/100	Thermo Fisher Scientific
Claudin-1	sc-81796	Mouse	1/100	Santa Cruz Biotechnology
Claudin-4	36-4800	Rabbit	1/100	Thermo Fisher Scientific

5.1.2 3D model

This method is particularly useful in verifying protein expression in 3D spheroid invasion assay in different zones of spheroids as the necrotic center, the peripheral zone and protrusions from invasion. After the established 3D spheroid invasion assay, were waited approximately three days for the spheroids invasion into Matrigel®. At this moment, when the spheroids had significant levels of invasion the immunofluorescence technique was applied. Due to the presence of the extracellular matrix where the spheroids were submerged, a few steps were performed to facilitate penetration of the antibodies into the Matrigel®.

Thus, the spheroids in Matrigel® were washed with PBS carefully and were fixated using PFA 4%. After spheroids has been washed thrice with PBS, were permeabilized for 30min with PBS-0.4% Triton and washed one more time. Then,

the spheroids were blocked with 4% of serum of the species of the secondary antibody (normally goat serum) in PBS-0.2% Triton for 45min at RT.

Following a blocking step, spheroids were incubated with primary antibodies at the corresponding dilution (**Table 16**) in 1% serum in PBS-0.075% Triton for over weekend (72h) at 4°C covered for aluminium foil. Afterwards, wells were washed thrice with PBS and were applied secondary antibodies diluted 1/200 in 2% of serum in PBS together with DAPI during 2h at RT. Additionally, all incubations during thi protocol were performed in shaker.

Lastly, wells were washed thrice more and slides were gently mounted using a Mowiol® (Sigma-Aldrich) mounting media, after 12 hours drying the spheroids were already ready for analysis. To obtain a high 3D resolution of spheroid staining, images were taken by Leica TCS SP5 of confocal microscopy using the Leica LAS AF software and images were analysed by Image J Software.

5.2 Western blotting

To verify protein levels in *in vitro* samples western blotting technique was performed. Almost all steps during the western blot procedure from *in vitro* samples share the same *in vivo* tissue protocol that was previously described in the section 2.2, 2.3, 2.4. However, only the step of protein extraction differs from the protocol previously described and so will be detailed below. Protein lysates from 2D and 3D model was performed respectively from p100 plates of βTC4 cells with 90-100% of confluency and pellets from spheroids βTC4 obtained though spheroid harvesting procedure described in section 4.3.3.

In 2D model, the cells were washed twice with PBS and 300µl-500µl of RIPA lysis buffer were added into the plate. After 5min in ice, cells were scraped using a cell scraper (Sarstedt) and place to an Eppendorf. In the other hand, in 3D model a pellet from βTC4 spheroid was mixed with 200µl of RIPA and incubated during 5min in ice. Finally, both kind of samples were incubated in rotation during 30-40min at 4ºC. At the end, samples lysates were centrifuged at 14000rpm for 15min at 4ºC and supernatants were stored at -20ºC.

6. *In vitro* molecular analysis

βTC4 cells and pellets from spheroids βTC4 (section 4.3.3) obtained through spheroid harvesting procedure were homogenized manually and RNA was extracted with RNeasy Plus kit (Qiagen) following the manufacturer's instructions. RNA extraction, quantification, cDNA obtention and RT-qPCR were performed using the same procedure detailed for tissues (section 3.1, 3.2, 3.3).

7. *In silico* clinical samples analysis

Clinical data from PanNETs was obtained from independent gene expression study of a set of mRNA transcriptomes of PNET patients from the public database Gene Expression Omnibus (GEO) in which the Genome of reference is GSE73338 (Missiaglia et al., 2009; Sadanandam et al., 2015). Dataset analysed comprised 90 samples of a PNET study containing normal pancreas, normal pancreas islets, primary non-functional tumors, primary functional tumors (insulinomas), and metastases from non-functional primary tumors.

In order to compare our candidate genes in three tumoral progression stages, we grouped clinical data from PanNETs in: primary non-malignant tumors, primary malignant tumors and metastasis. Thus, our analysis was performed using 63 non-functional primary tumors, in which 31 had synchronic metastasis and were determined as malignant primary tumors. In this group of 31 patients, 7 samples were from liver or lymph node metastases. Finally, the 26 non-functional primary tumor patients did not have metastasis were classified as non-malignant primary tumors (Missiaglia et al., 2009; Sadanandam et al., 2015).

8. Statistical analysis

In order to compare small samples size that in fact not were normally distributed, a non-parametric suitable test for each case was used (Mann-Whitney).Two-sided and unpaired tests were used for data analysis. Differences were considered statistically significant at $p<0.05$. Statistic coding: *$p<0.05$, **$p<0.01$, ***$p<0.001$, ****$p<0.0001$. GraphPad Prism v6 software

(GraphPadsoftware, Inc. USA) was used to plot data in graphs and to do statistic tests.

RESULTS

1. Invasion morphological delineation

To characterize the phenotype of cancer cell invasion on PanNETs before and after the therapy, first of all, we needed to determine which types of invasion morphologies are found in our *in vivo, in vitro* models.

1.1 RIP1-Tag2 mouse model

RIP1-Tag2 is a transgenic animal model of PanNETs that at tenth weeks of its life begin to present solid tumors, in which after 12-13 weeks of age progress to larger adenomas or invasive carcinomas. In addition, as described in Introduction section 6.1 (**Figure 18**), results from our group demonstrated an irreversible increase in the incidence of invasive tumors during anti-angiogenic treatment in the RIP1-Tag2 mouse model. For this, to describe the invasive morphology from RIP1-Tag2 we chose controls and anti-angiogenic treated tumors at 16 weeks.

First, in relation to treatment applied, sunitinib-treated tumors showed a higher invasive capacity. However, this invasion increasing does not change the invasion morphology observed. Thus, control and sunitinib-treated tumors, in terms of morphology, share the same type of invasion as can be seen in Figure 4.

The histo-morphological characteristics of invasion in these tumors revealed a very distinct invasion pattern, not resembling single cell invasion (ameboid or mesenchymal) but rather a collective type of invasiveness, in which overall features from individual invasion are lost. Tumor cell movement from pancreatic islet seems to be organized, which allows invasive cells to maintain high levels of cell-cell junctions molecules and communication between cells during the invasion process.

To determine the cancer cell collective invasion in RIP1-Tag2 control and treated tumors, the three hallmarks that characterize collective movement were confirmed: (i) the cells remained physically and functionally connected during the movement, (ii) the force for migration was maintained by supracellular organization and, (iii) moving cell groups modified the tissue along the migration path (**Figure 25**). As for morphology, we classified the invasion in RIP1-Tag2 as a coordinated collective invasion, when more than 10 cells invade connect across a tissue surface and remaining attached to a large tumor mass.

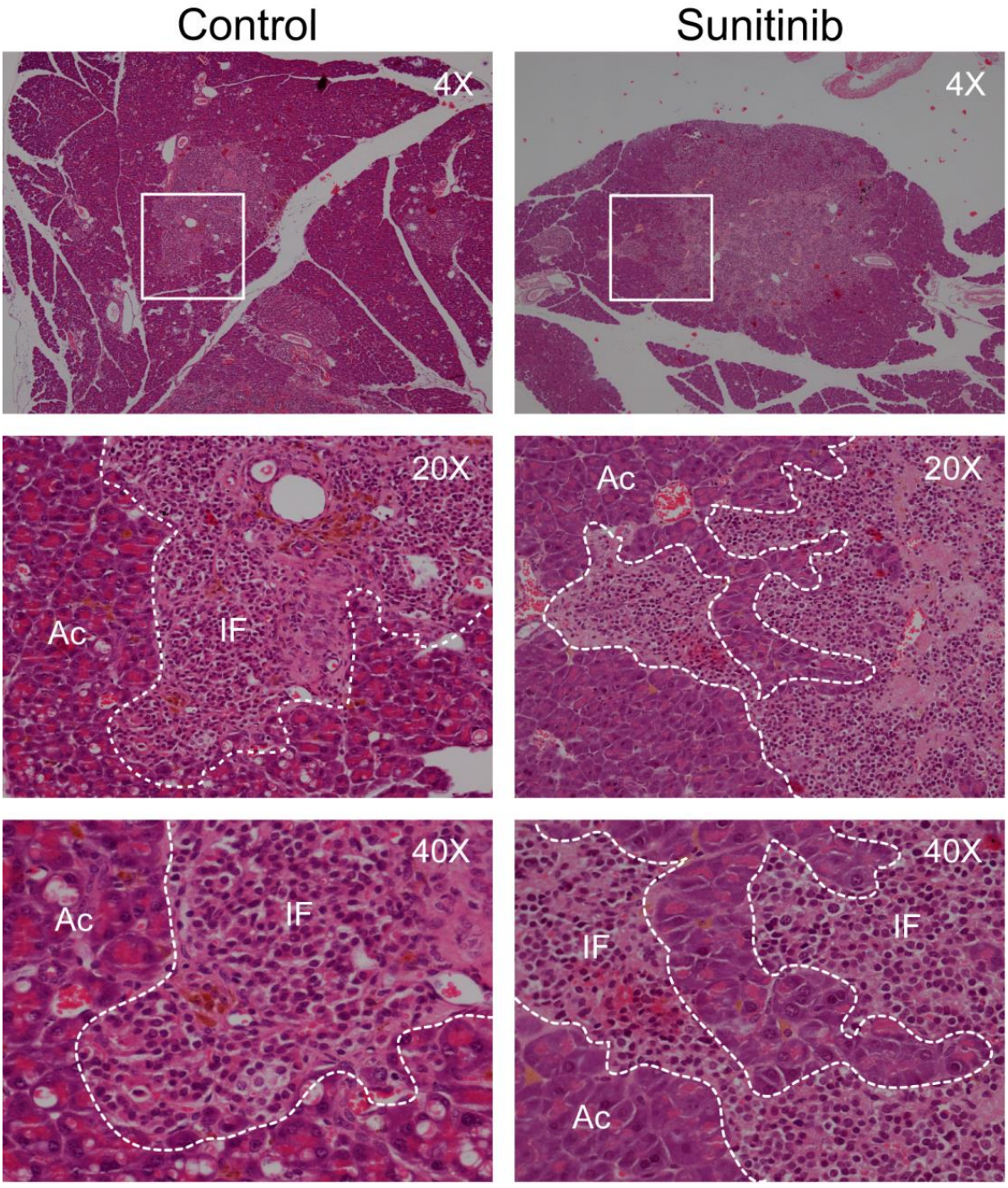

Figure 25. Morphologically RIP1-Tag2 tumors presented coordinated collective invasion before and after anti-angiogenic treatment. Hematoxylin and eosin staining was performed on tumor tissue (paraffin embedded samples) before and after sunitinib treatment (4 weeks). Front tumor invasion was highlighted with a white dotted line (T = Tumor; Ac = Acinar Tissue; IF = Invasive Front). Images at 4X, 20X and 40X.

1.2 βTC4 *in vitro* 2D, 2,5D and 3D model

The βTC4 cancer cell line was derived from PanNETs tumors from RIP1-TAG2 mouse. Interestingly, during βTC4 cells *in vitro* culture maintenance, we verified specific adhesion characteristics in these cells. For example, as previously described by Hanahan (Efrat et al. 1988), βTC4 cells must be cultured at high confluency, being essential a cell-cell contact for the maintenance and growth of these cells. In addition, we observed the spontaneous appearance of cellular aggregates during βTC4 cells maintenance that can be defined as βTC4 spheroids (**Figure 26A**).

βTC4 spheroids are formed by a necrotic core with an intermediate layer of quiescent cells and another outer layer of proliferating cells, thus, simulating an *in vivo* tumor structure (**Figure 26B**). In this context, we hypothesized that inserting the spheroids into structures that favor invasion and migration steps should be a useful method to verify the morphology of βTC4 cells in these processes. To be able to confirm this hypothesis, we set up an *in vitro* two- and three-dimensions assay using βTC4 spheroids. To determine which extracellular matrix was able to maintain the βTC4 cellular adhesions morphology, the βTC4 spheroids Behaviour was verified in the following coatings: Matrigel®, Collagen I, Gelatin, Laminin and Collagen IV (**Figure 26C**).

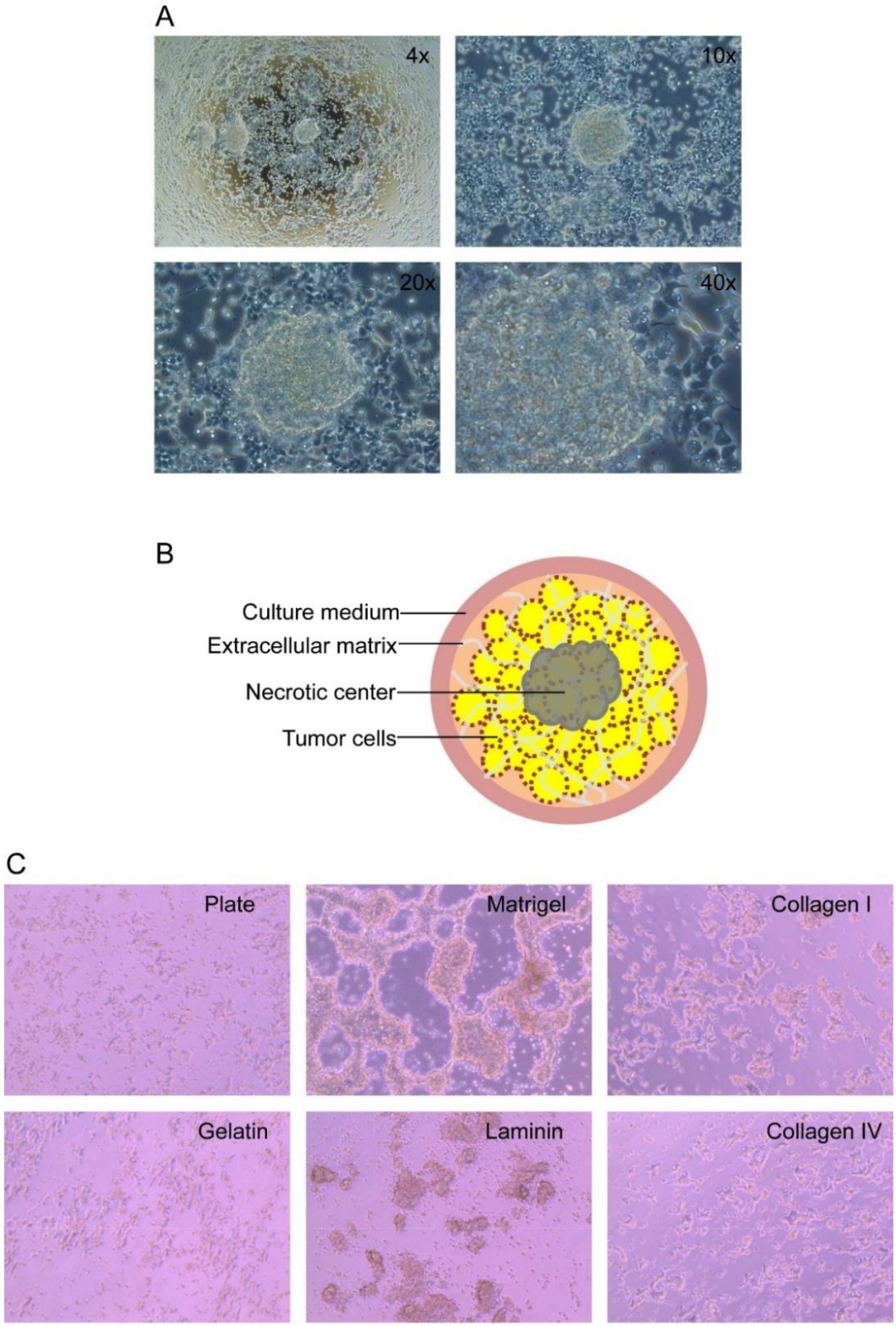

Figure 26. βTC4 spheroid characterization. **(A)** Spheroids spontaneously generated during βTC4 cell culture. βTC4 cell and spheroids cultured in DMEM 15%FBS medium, images at 4X, 10X, 20X, 40X. **(B)** βTC4 spheroid structure. **(C)** βTC4 cells during 24 hours on different coatings, Matrigel®, collagen I, gelatin, laminin and collagen IV, images at 10X.

As shown in **Figure 26C**, the spheroid structure network was only maintained in Matrigel® and laminin coating. In compositional aspects, besides laminin, the Matrigel® is composed of collagen IV, heparin sulfate proteoglycans, entactin/nidogen, and several growth factors. Matrigel® is a complex natural cell matrix derived from mouse sarcoma basement membrane and the more complete scaffold to mimic *in vivo* environments for 2,5D and 3D βTC4 spheroids applications.

As mentioned before, during this thesis were used *in vitro* 2D, 2,5D and 3D models (**Figure 27**). The terms '2D model' and '2,5 model' are used here unchangeably to mean: Matrigel® coating presence or absence, and single cells and spheroids selection or not. In 2D model cells are placed in a no coating plate and may contain spheroids in its composition or not (**Figure 27A-D**). Both models, 2,5D and 3D, were designed only with βTC4 spheroids. In the 3D invasion assay, βTC4 spheroids were embedded in Matrigel® and βTC4 cells invade the surrounding 3D extracellular matrix generating strands (**Figure 27I-J**). On the other hand, 2,5D migration assay was thought to verify migration process in the absence of the physical constraints imposed by the extracellular matrix, for this, only βTC4 spheroids were seeded on a Matrigel® coating and were observed during 24h-36h (**Figure 27E-H**). Then, through *in vitro* βTC4 spheroid models that mimic a tumor micro-region from RIP1-Tag2, it was possible to study both the invasion and migration patterns by 2,5D and 3D assays set-up in this project.

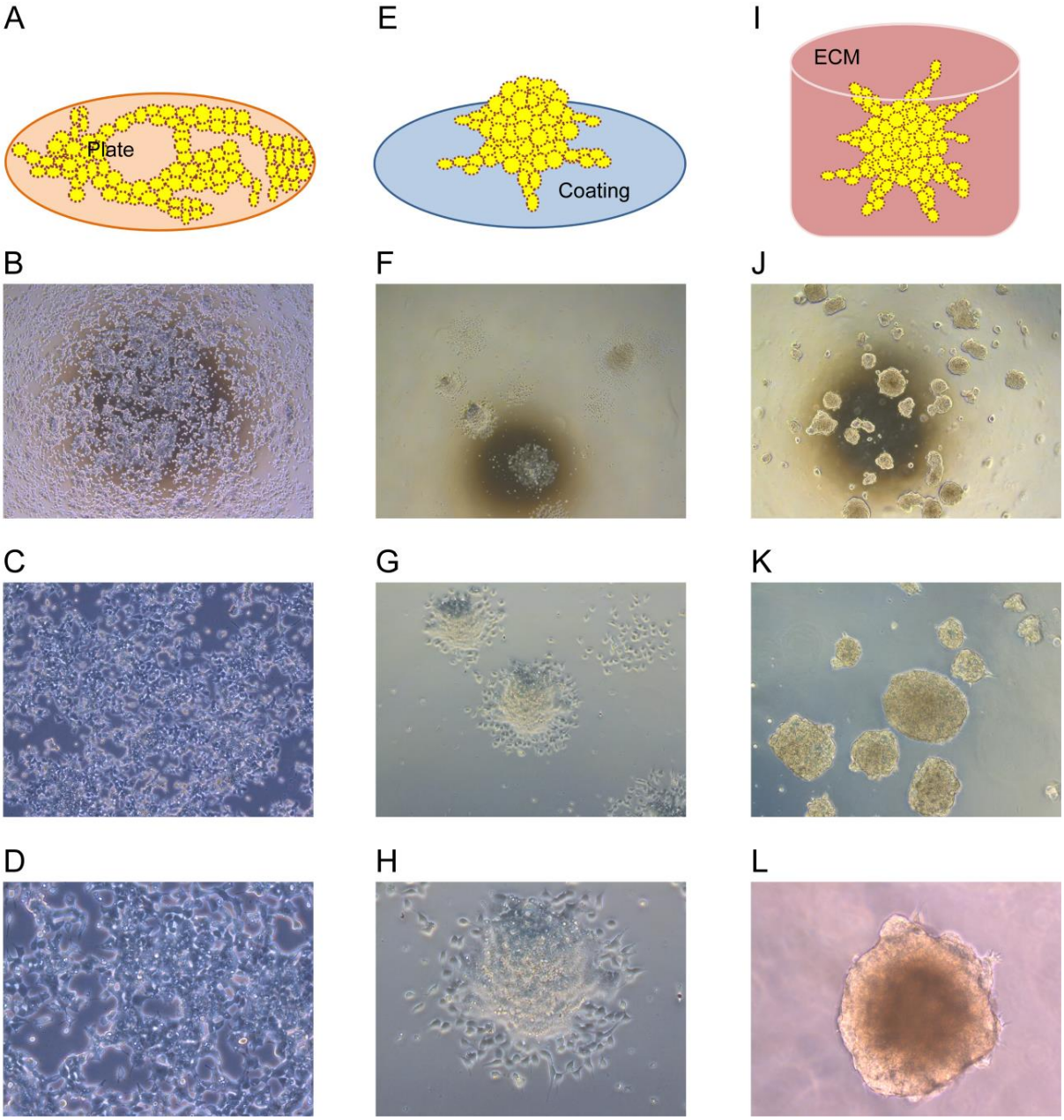

Figure 27. βTC4 *in vitro* 2D, 2,5D and 3D models. (A) Illustration of the 2D model. **(B-D)** 2D model from βTC4 cells/spheroids in plate. Images at 4X, 10X, 20X. **(E)** Illustration of the 2,5D migration assay. **(F-H)** 2,5D model containing βTC4 spheroids in Matrigel® coating for 24 hours. Images at 4X, 10X, 20X. **(I)** Illustration of the 3D invasion assay. **(J-L)** 3D invasion model formed by βTC4 spheroids embedded in Matrigel® after 48 hours of invasion. Images at images at 4X, 10X, 20X.

Next, we focused our attention on the *in vitro* models in detail and their invasion/migration behaviour. On the first day, spheroids from 2,5D assay presented migrating cells (**Figure 28B**), revealing differences in comparison to 2D model, where spheroids directly planted on the plate did not initiate the cellular

migration (**Figure 28A**). As we can see in **Figure 28B**, migrating cells from spheroids appear to move in concert, without completely disrupting their cell-cell contacts and without dispersing by the Matrigel®.

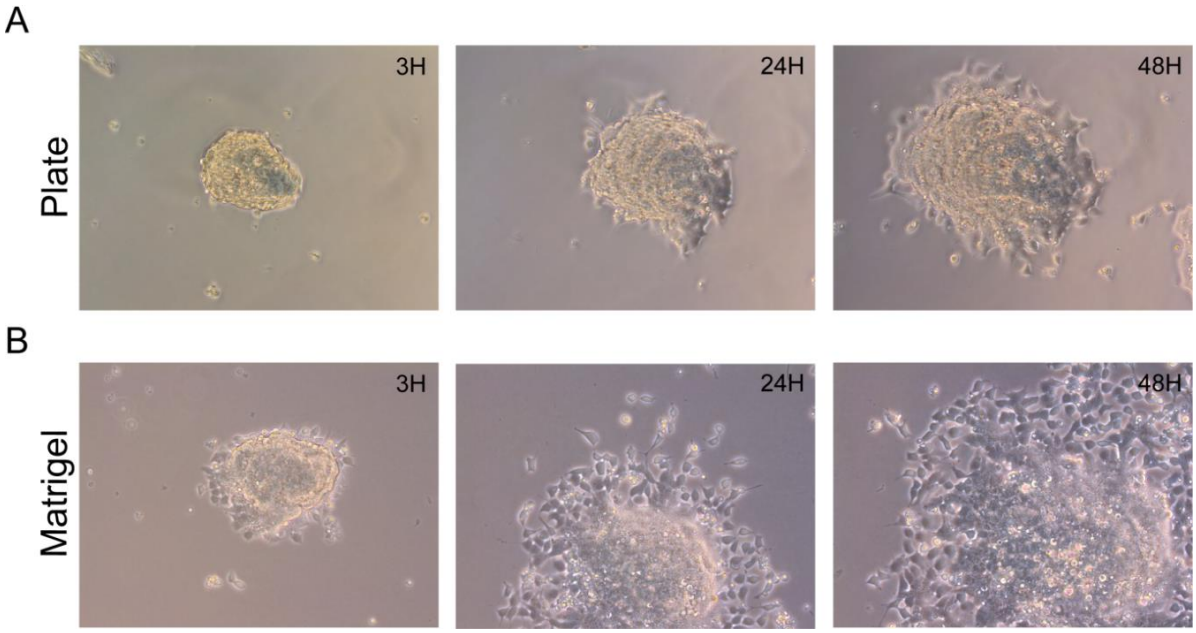

Figure 28. βTC4 migrating cells in 2D and 2,5D model. **(A)** βTC4 spheroids without coating placed directly on plate after 3, 24 and 48 hours. **(B)** βTC4 spheroids in Matrigel® coating after 3, 24 and 48 hours of migration. Images at 20X.

We also noticed that βTC4 spheroids were highly invasive in the 3D assay. Spheroids started to present invasive properties on day one into Matrigel® (**Figure 29B**). Although, only three days after it was possible to verify a high differential between invasive or non-invasive spheroids. An invasion peak was verified at day six, when 95% of all spheroids invaded on extracellular matrix (**Figure 29A**). As it is shown in **Figure 29C**, spheroid invasive fronts keep multicellular structures such as, strands, protrusions or clusters remaining from a cohesive movement, indicating that the invasion in PanNETS seems guided by collective invasion behaviour.

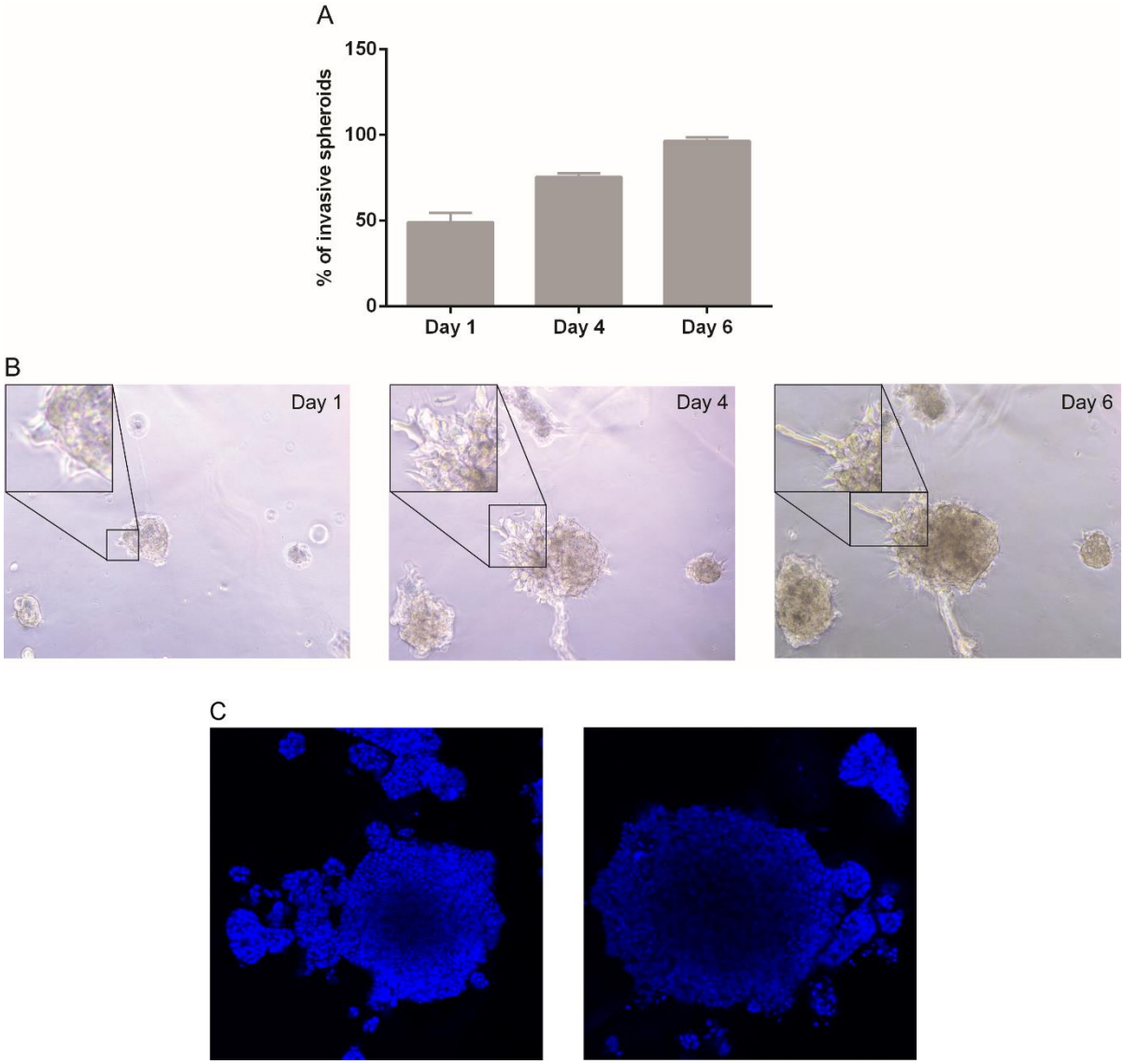

Figure 29. βTC4 invading spheroids in 3D model. βTC4 spheroids embedded in Matrigel® cultured in βTC4 cells normal conditions (DMEM 15% FBS). **(A)** Invasive βTC4 spheroids percentage in relation to the total spheroids (n=2). **(B)** Collective invasion morphology at day 1, day 4 and day 6. Images at 10x. Zoom from 10X images. **(C)** DAPI staining of invasive βTC4 spheroids submerged in Matrigel®.

In addition, to further characterize βTC4 spheroids as to collective invasion, proliferation and cytoskeletal structure, we performed an immunocytofluorescence using 3D model. In this way, we chose CDH1 and CTNNB1 proteins as epithelial markers, Ki67 to verify proliferation, and F-actin as cytoskeleton marker (**Figure 30**). In addition, to further characterize βTC4 spheroids as to collective invasion, proliferation and cytoskeletal structure, we performed an immunocytofluorescence

using 3D model. In this way, we chose CDH1 and CTNNB1 proteins as epithelial markers, Ki67 to verify proliferation, and F-actin as cytoskeleton marker.

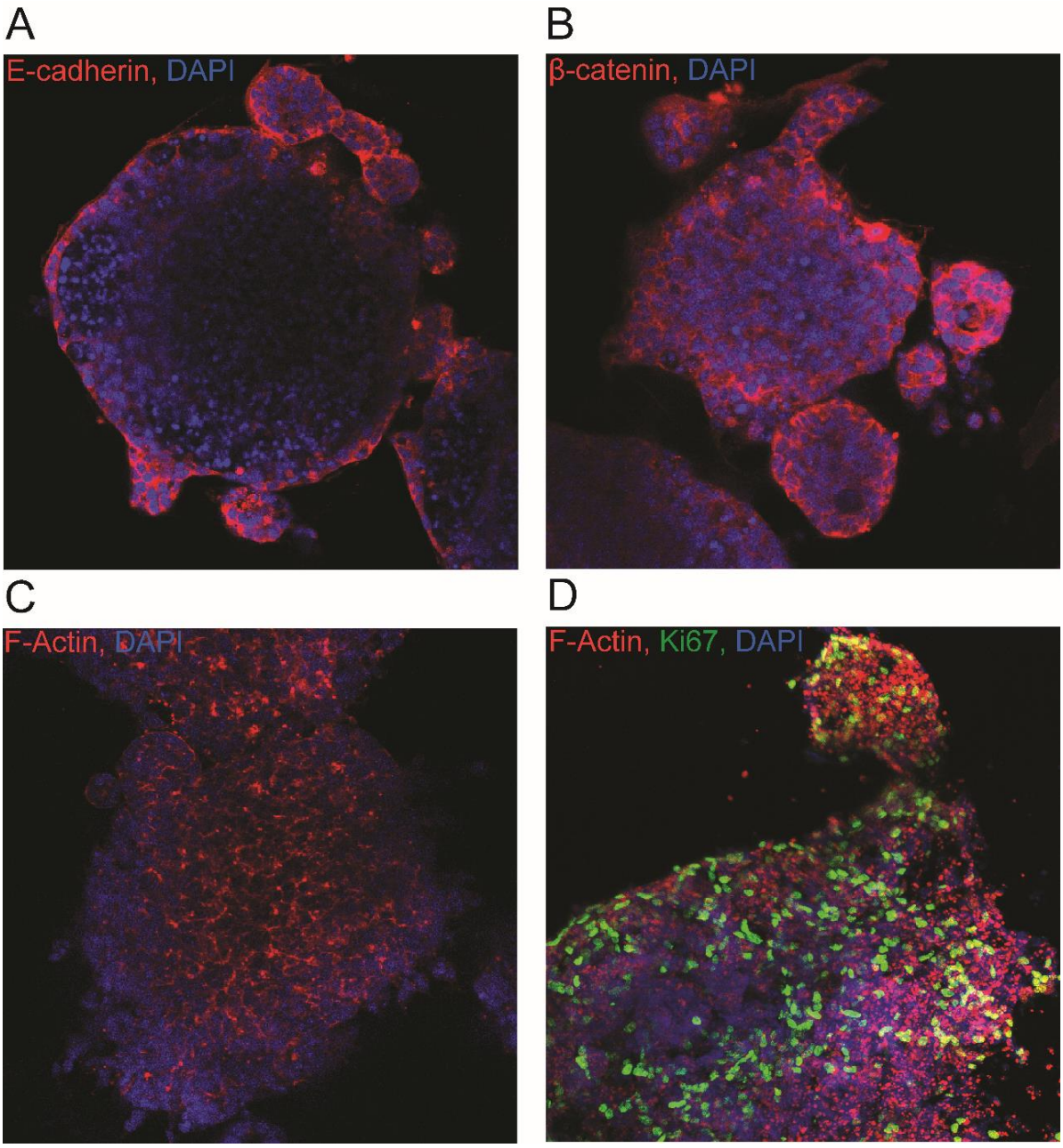

Figure 30. βTC4 spheroids besides proliferative, showed epithelial markers in their invasive fronts and cytoskeleton markers throughout its structure. βTC4 spheroids after four days of invasion in Matrigel® cultured in normal conditions (DMEM 15% FBS). Immunocytofluorescence of **(A)** CDH1, **(B)** CTNNB1, **(C)** F-actin, and **(D)** Ki67 and F-actin were performed. DAPI was used to perform nuclear staining. Images at 20X.

As expected due the collective invasion morphology determined previously, group of cells from invasive strands express epithelial markers as CDH1 and CTNNB1 (**Figure 30A-B**). On the other hand, F-actin protein was verified mostly localized in the center of the spheroid (**Figure 30C**), probably maintaining the cytoskeletal structure and generating traction/protrusion force to migration. Finally, we confirmed that, all spheroid zones are proliferative, given that cells marked by Ki67 was found in all spheroid zones, demonstrating that our 3D model maintains cell viability and proliferation (**Figure 30D**).

Together, these *in vitro* data suggest that βTC4 spheroids invasion and migration process does not follow the traditional mesenquimal invasion concept, when cells invade the peritumoral stroma by single cells invasion mechanism, but it rather involves cell groups whose collective behaviour defines malignant function.

Moreover, *in vitro* culture, we notice two subpopulations of βTC4 spheroids with different tumor malignancy capacity. That is, we detected in βTC4 spheroids the same characteristic that occurs in many tumors *in vivo*, the intra-tumor heterogeneity. In this context, cancer cells can exhibit distinct morphological and phenotypic profiles within the same tumor as a consequence of genetic change, environmental differences, and reversible changes in cellular properties (Meacham and Morrison 2013). Specifically, in βTC4 spheroids, different passages of spheroids were cultured in small plates long-term, due to the features variability observed in this technique, we checked different parameters of spheroid culture before the experimental procedure. During this step, was noted that two populations of βTC4 spheroids with a very high differential as for invasion capacity, then, we used the term "*high*" to more invasive spheroids and "*low*" to spheroids with less invasion level.

To confirm these Behaviour differences, we started analyzing migration capacity between *high* and *low* βTC4 subpopulations using 2,5D model migration assay in different coatings. The first conclusion was that the *high* and *low*

spheroids in plate, laminin, and gelatin did not show relevant comportment alterations (**Figure 31A-B**).

Given the relevant characteristics observed in 2,5 migration assays, we refine this analysis through a time-lapse in vivo assay. In this experiment, we might follow the sequential migration movement. Thus, we did not observed differences in plate and laminin conditions by time-lapse continues analysis (**Plate videos: 1.a (*high*), 1.b (*low*), Laminin videos: 2.a (*high*), 2.b (*low*); supplemental material**).

As seen previously, when Matrigel® coating was used, βTC4 cell from spheroids showed migration in both *high* and *low* subpopulations. In more depth, *high* cells exhibited a migration in which the cell-cell junctions are not lost, as originally βTC4 cells act. On the other hand, *low* cells migrating independently of one another and, thus, they appeared not to maintain cell-cell junctions unlike *high* cells (**Figure 31C**).

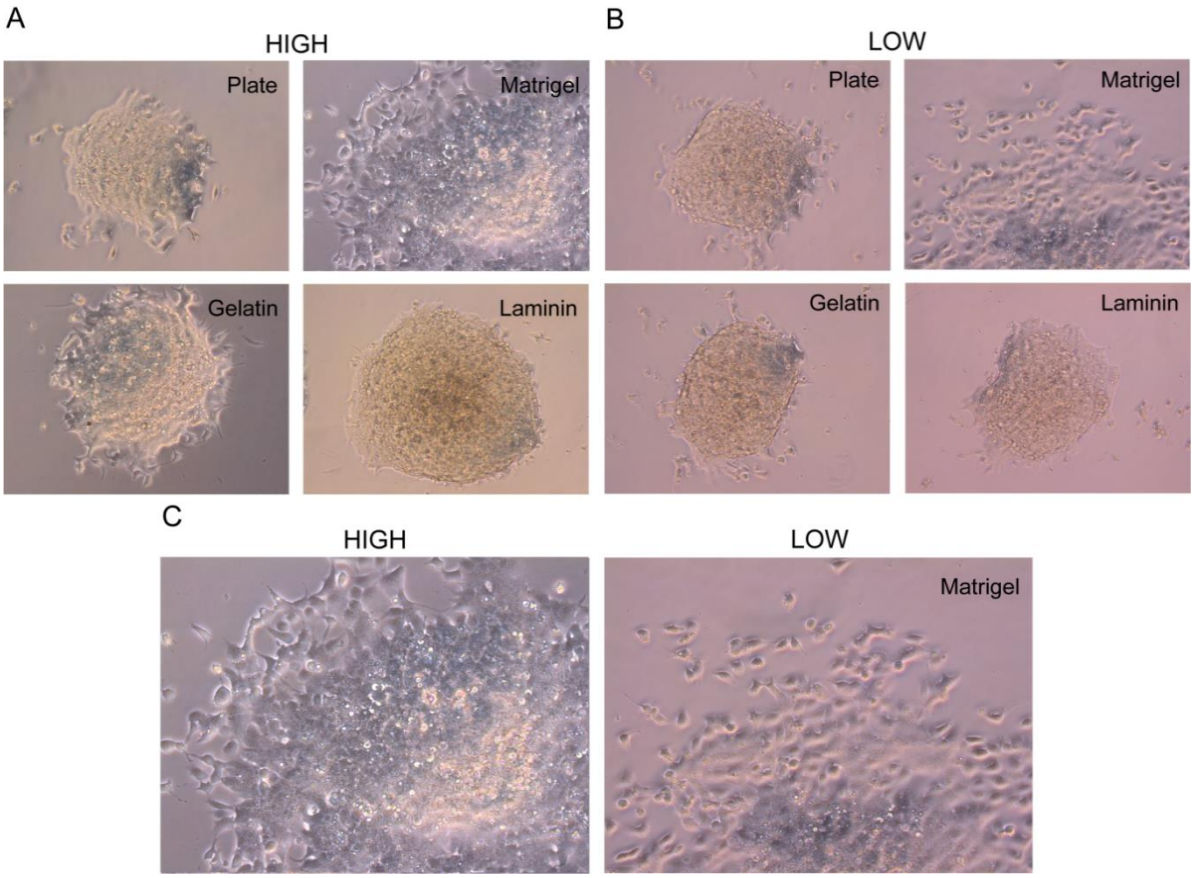

Figure 31. *High* cells migrated on the Matrigel® without lost the cell-cell contacts. (A-B) *High* and *low* spheroids were placed into plates or different coatings: gelatin, laminin and Matrigel® **(C)** *High* and *low* βTC4 cells at 48hs of migration in Matrigel® coating. Images at 20X.

In time-lapse analysis, *high* subclone movement always are maintained a connection point between the cells, confirming their cluster migration capacity. However, *low* cells do not function within this mechanism. In this case, a disconnection, in which leader cells started to advance by single cell migration process was observed, but, as these cells were not connected they retreated their way in search of other cells, not allowing an efficient migration (**Matrigel videos: 3a (*high*); 3b (*low*), supplemental material**).

In the next step, we used spheroids from *high* and *low* cells to compare quantitatively the cell collective invasion through of 3D invasion assay. *High* spheroids were clearly more invasive than *low* spheroids (**Figure 32**), as much in the quantity of spheroids able to invade as in the number of strands per spheroid.

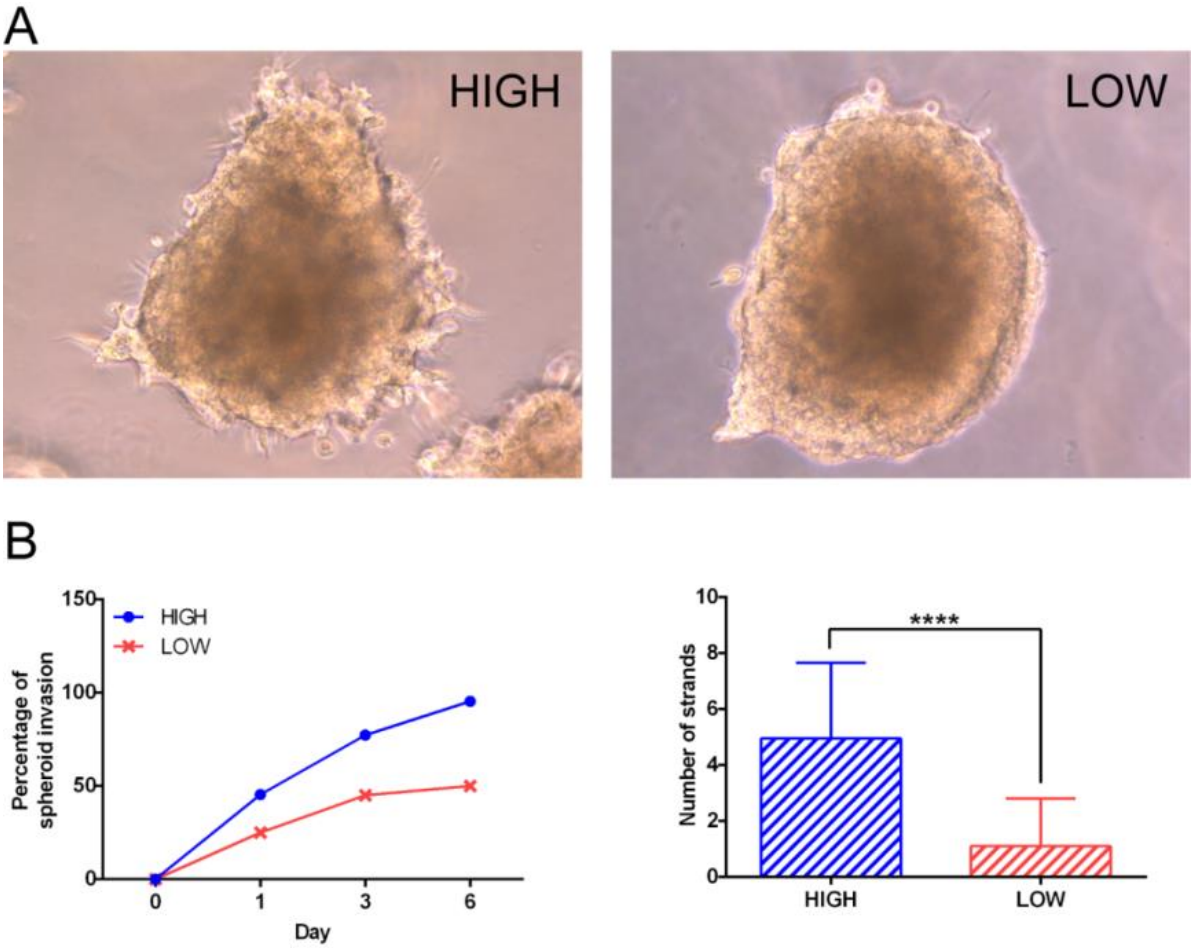

Figure 32. *High* βTC4 spheroids presented higher capacity of collective invasion than *low* βTC4 spheroids. (A) Representative images of *high* and low βTC4 spheroids embebbed in Matrigel® cultured both under normal conditions of maintenance of βTC4 cells. In the fourth day of culture they presented distinct invasion phenotypes. Images at 20X. **(B)** Percentage of invasive spheroids in relation to a total of spheroids (left graphic). Quantification of strands per spheroid n=20 (righ graphic). Difference statically significant (p<0,0001) by Mann-Whitney test.

To compare an invasion capacity of *low* and *high* subpopulations from βTC4 cells we performed a Transwell® invasion assay in basal condition. βTC4 *high* and *low* cells (5.0 x 10^5 cells/mL) of βTC4 DMEM medium (5% of FBS) inserts of the Transwell®® containing a polycarbonate membrane were placed. At the bottom of the well βTC4 DMEM medium (15% of FBS) was placed. Cells were maintained in normoxia at 21% O_2, 5% CO_2, 37°C (**Figure 33**).

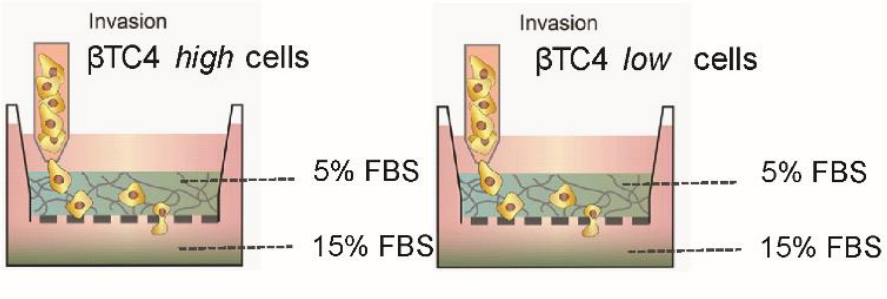

Figure 33. Experimental design of Transwell® invasion assay to compare an invasion capacity of *low* and *high* subpopulations from βTC4 cells.

Finally, as we expect, Transwell® invasion assay confirmed the existence of two subpopulations from βTC4 cells with a high differential as for invasion capacity (**Figure 34**).

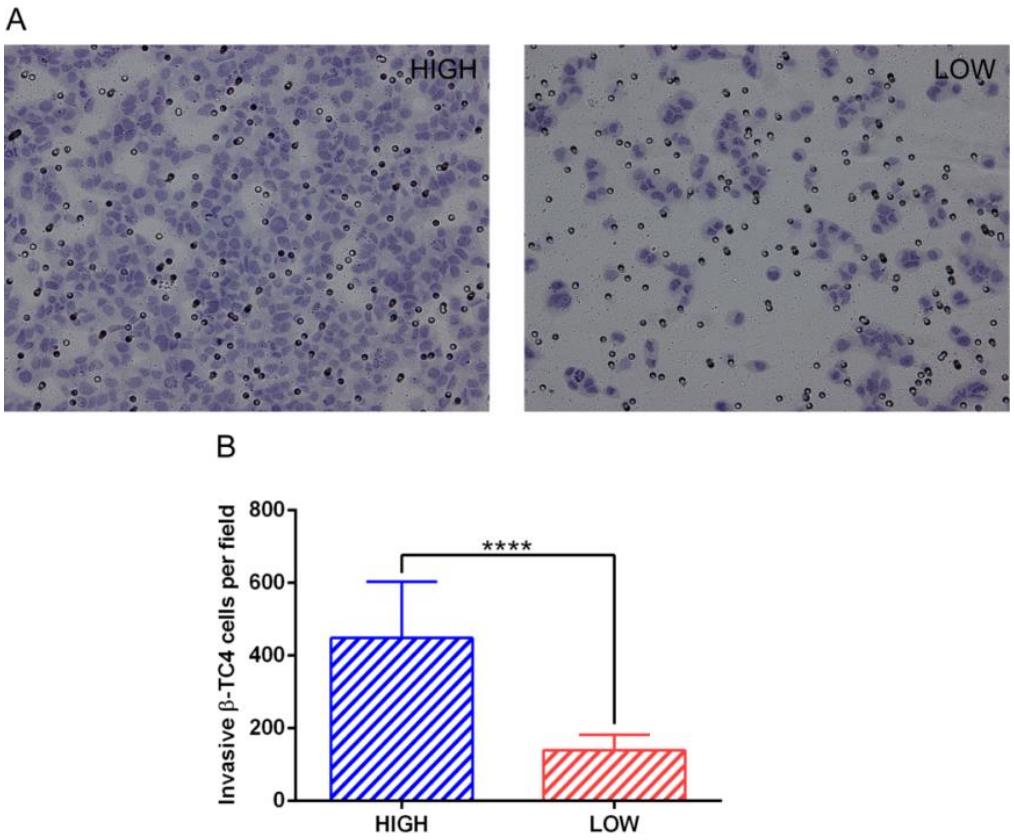

Figure 34. *High* βTC4 cells presented greater capacity of invasion in comparison to the *low* βTC4 cells. 500.000 cells were plated onto each well and the assay was performed at 48h. Error bars represent S.D, wells/condition n=3. **(A)** Representative images of hematoxylin staining from βTC4 cells in membrain by Transwell®® invasion system: *high* cells (left image) and l*ow* cells (right image). **(B)**

βTC4 *high* cells showed higher invasive capacity than *low* cells. Difference stastically significant (p< 0,0001) by Mann-Whitney test.

In summary, βTC4 *in vitro* results demonstrated morphological characteristics from cancer cell collective invasion and migration. Thus, the *high* and *low* subpopulations described were applied as tools to confirm the collective mechanisms from βTC4 cells and spheroids detailed in the following chapters.

2. Invasion molecular characterization

To further validate, previously observed morphological collective Behaviour, the next step was to verify molecular evidences of collective invasion in *in vitro*, *in vivo* samples.

2.1 Characterization of CDH1-mediated collective invasion

As mentioned in the introduction section, the CDH1 is a major cell-cell adherent molecule that inhibits motility of single cells invasion on matrix. On the other hand, CDH1 is an integral component of the guidance mechanisms that orchestrate collective movement, given that adhesion between motile cells and polar cells holds the cluster together and polarizes each individual cell. Thus, knowing the CDH1 role previously described in collective invasion, we decided to verify its expression pattern in our samples.

As we can see in western blot analysis, both untreated and treated tumors expressed CDH1, but after treatment tumors slightly increased CDH1 protein levels (**Figure 35**). In fact, even though western blot analysis is quite efficient for determining protein presence or absence in an entire tumor, this technique is not able to provide information taking into account protein expression variability in different regions of tumor.

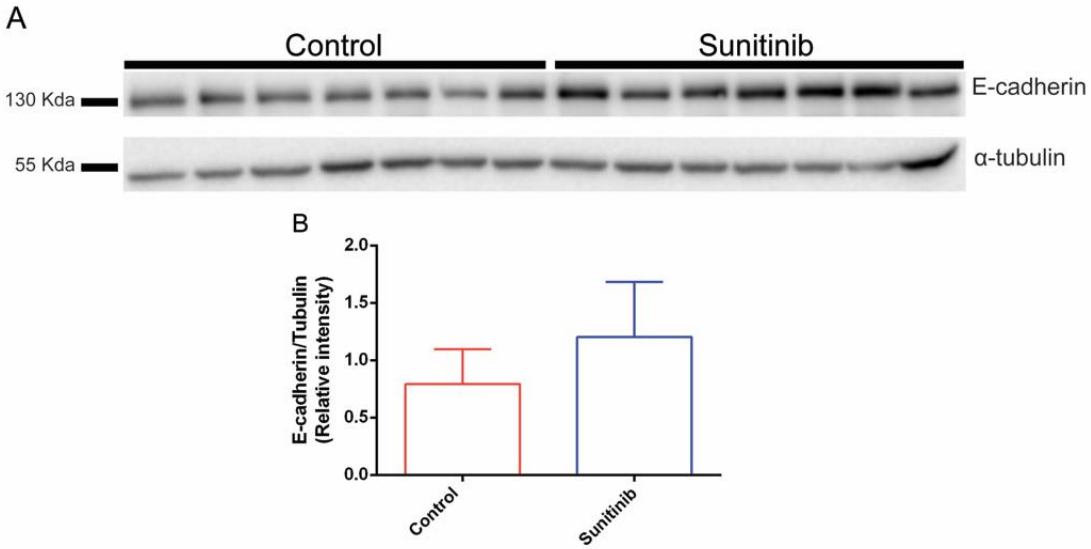

Figure 35. RIP1-Tag2 sunitinib treated tumors showed a CDH1 increase levels in relation to untreated tumors. Trend of CDH1 increase in sunitinib treated tumors (p=0.0728) by Mann-Whitney test. CDH1 detection by western blot from lysates of seven control tumors and seven tumors treated during 4 weeks with sunitinib (both 16 weeks of age). α-Tubulin was used as housekeeping gene. Error bars represent S.D.

To verify intratumoral heterogeneity at the CDH1 expression level, we performed CDH1 immunohistochemistry staining. Thus, it was possible to distinguish CDH1 intensity in periphery key areas, to thereby to correlate protein levels with overall tumor invasiveness. Specifically, CDH1 levels were determined according with the intensity of CDH1 in each tumor front area, including encapsulated tumor fronts and invasive tumor fronts; and excluding tumor center areas (**Figure 36**). Finally, total average of all tumors fronts quantified was correlated with the global tumor invasion per each tumor.

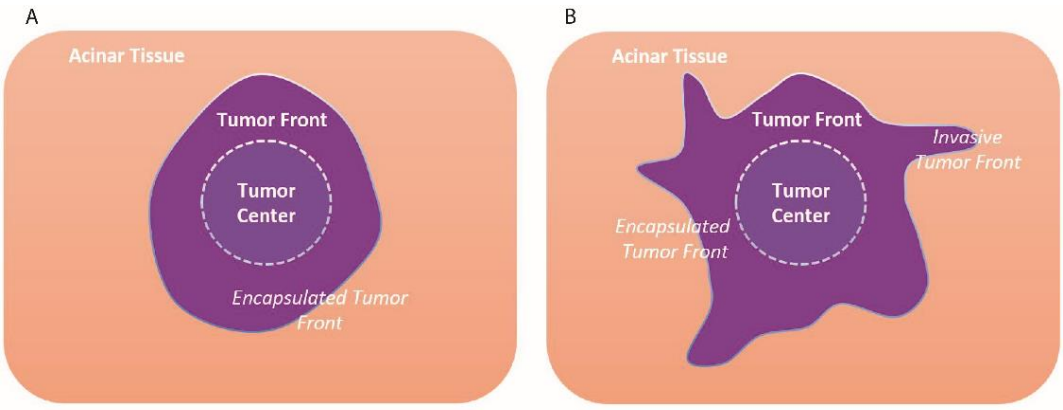

Figure 36. CDH1 immunohistochemistry quantification area. Representative images of encapsulated tumors **(A)** and invasive tumors **(B).** The quantification was performed taking to account each tumor front area, including encapsulated tumor fronts **(A-B)** and invasive tumor fronts **(B)** excluding tumor center areas.

Since RIP1-Tag2 tumors may be invasive before and after treatment, we analysed control and treated tumors in separate according to its invasiveness. As shown in **Figure 37A**, the invasive fronts from RIP1-Tag2 untreated tumors tend to present more CDH1 protein levels than encapsulated fronts. Besides that, there is a positive correlation between high invasiveness capacity and the increases of CDH1 levels (**Figure 37B**).

Finally, there almost does not exist CDH1 expression difference between invasive and encapsulated tumors in RIP1-Tag2 tumors after sunitinib treatment (**Figure 37C**). As well as, treated tumors which presented no significance when correlated with CDH1 expression (**Figure 37D**).

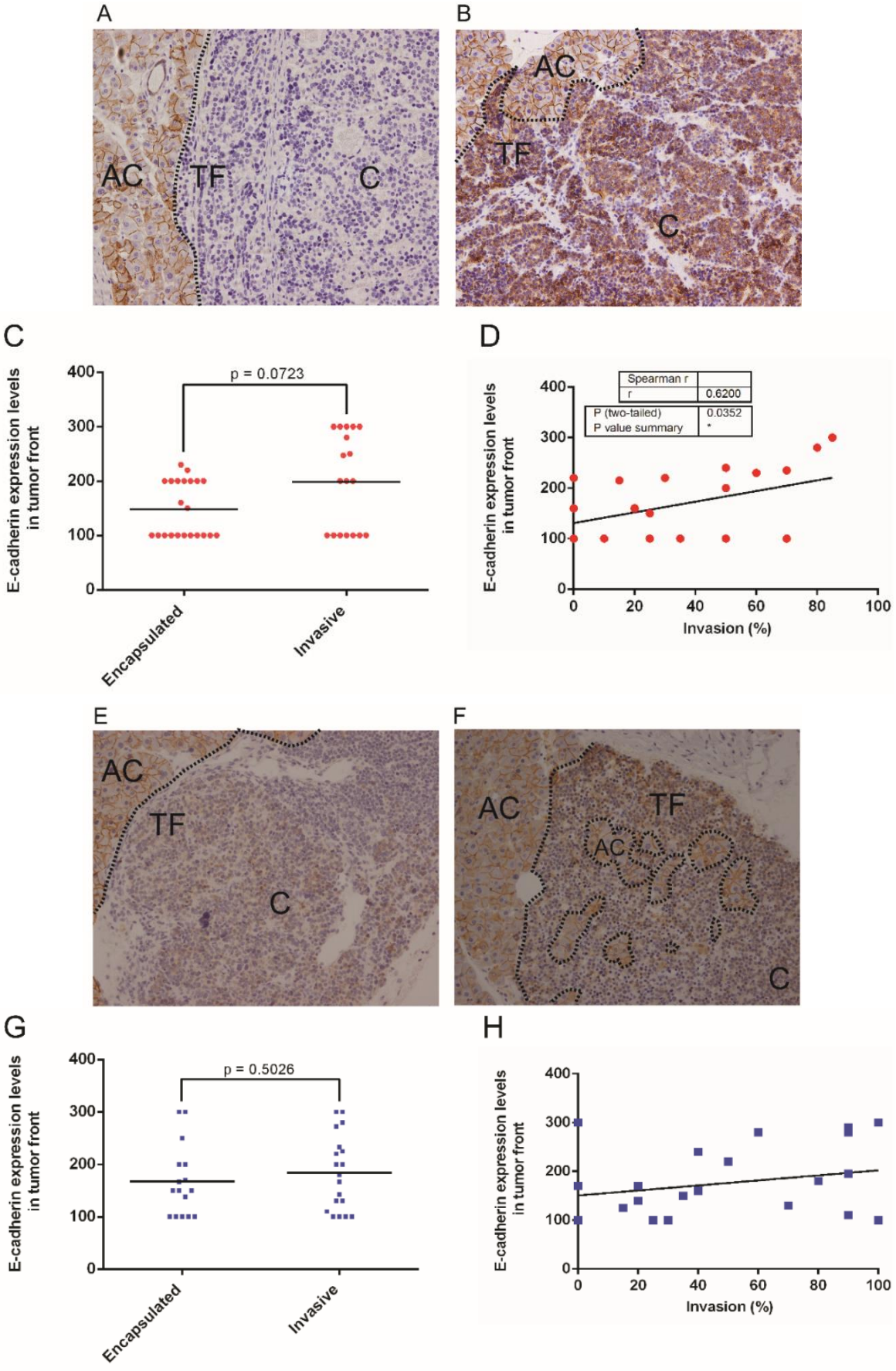
A
AC
TF
C
B
AC
TF
C
C
E-cadherin expression levels in tumor front
p = 0.0723
400
300
200
100
0
Encapsulated
Invasive
D
E-cadherin expression levels in tumor front
Spearman r
r
0.6200
P (two-tailed)
0.0352
P value summary
*
400
300
200
100
0
0
20
40
60
80
100
Invasion (%)
E
AC
TF
C
F
AC
TF
AC
C
G
E-cadherin expression levels in tumor front
p = 0.5026
400
300
200
100
0
Encapsulated
Invasive
H
E-cadherin expression levels in tumor front
400
300
200
100
0
0
20
40
60
80
100
Invasion (%)

Figure 37. Enrichment of CDH1 protein levels in control invasive tumors. Untreated tumors showed a tendency correlation between CDH1 expression and tumor invasion capacity. CDH1 immunohistochemistry was performed on RIP1-TAG2 tumor tissue at 16 weeks of age, untreated or treated with sunitinib during 4 weeks (C=Tumor Center; Ac=Acinar Tissue; TF=Tumor Front). Representative images at 20X. **(A)** Control non-invasive tumor and (B) Control invasive tumor **(C)** Invasive fronts (n=18) showed a trend of increment CDH1 levels in tumor front than encapsulated fronts (n=22). **(D)** CDH1 expression levels in tumor front zones (n=23) were positively correlate with high tumor invasion capacity. **(E)** Sunitinib treated non-invasive tumor. **(F)** Sunitinib treated invasive tumor. **(G)** CDH1 levels did not change in invasive (n=19) and encapsulated (n=16) tumor fronts after sunitinib treatment. **(H)** CDH1 expression levels in tumor front zones (n=24) demonstrated a low correlation with tumor invasion capacity. Significance was verified by Mann Whitney test. Spearman correlations were used to assess associations between continuous variables.

In the end, to compare these results before and after sunitinib treatment in the same analysis, we classified samples by their invasive phenotype, using a three-grade nomenclature classification of noninvasive encapsulated islet tumors (IT), microinvasive carcinomas (IC1), and widely invasive carcinomas (IC2) as described previously (Lopez and Hanahan 2002). As we can see in **Figure 38**, the only significant difference observed among IT, IC1 and IC2 classified samples, was that IT non-invasive control tumors showed lower CDH1 protein levels than IC2 widely invasive control tumors.

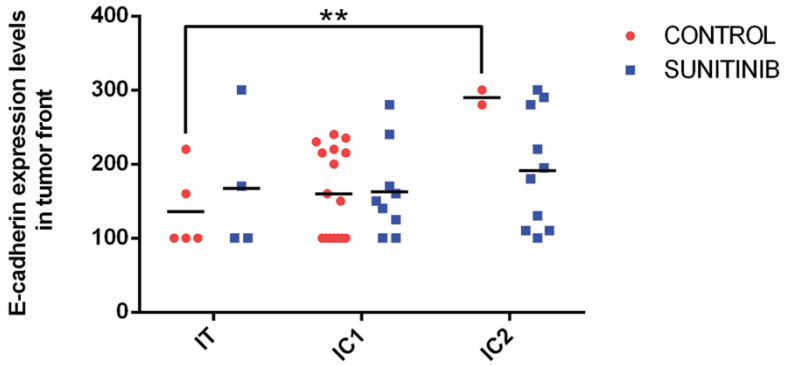

Figure 38. Control widely invasive tumors (IC2) showed higher CDH1 protein levels than noninvasive encapsulated islet tumors (IT), microinvasive carcinomas (IC1). Not significantly differences were observed in sunitinib treated tumors between IT, IC1 and IC2 groups. CDH1 immunohistochemistry was performed on RIP1-TAG2 tumor tissue at 16 weeks of age, untreated or treated with sunitinib for 4 weeks. IT control (n=5), IT sunitinib (n=5); IC1 control (n=16), IC1 sunitinib (n=9); and IC2 control (n=2), IC2 sunitinib (n=10).

All together, these results showed that despite CDH1 differential found in invasive control tumors have been positive, these differences in relation to anti-angiogenic treated tumors were not observed. Therefore, we conclude that CDH1 seems to be a major molecule that drives collective invasion in RIP1-TAG2 control tumors. However, the mechanisms that promotes tumor collective invasion through sunitinib treatment, following unknown and seems guided by CDH1 in conjunction with other molecular targets.

To confirm CDH1 results in βTC4 cells and spheroids, we decided to observe CDH1 expression pattern between highly and less invasive cells in our 2D (**Figure 39A**) and 3D models (**Figure 39B**). The results showed that cell and spheroids highly invasive express CDH1. While, less invasive cell and spheroids demonstrated the absence of the same protein. Thus, the matrix extracellular presence and of a structure closer to the tumor *in vivo* did not change these results.

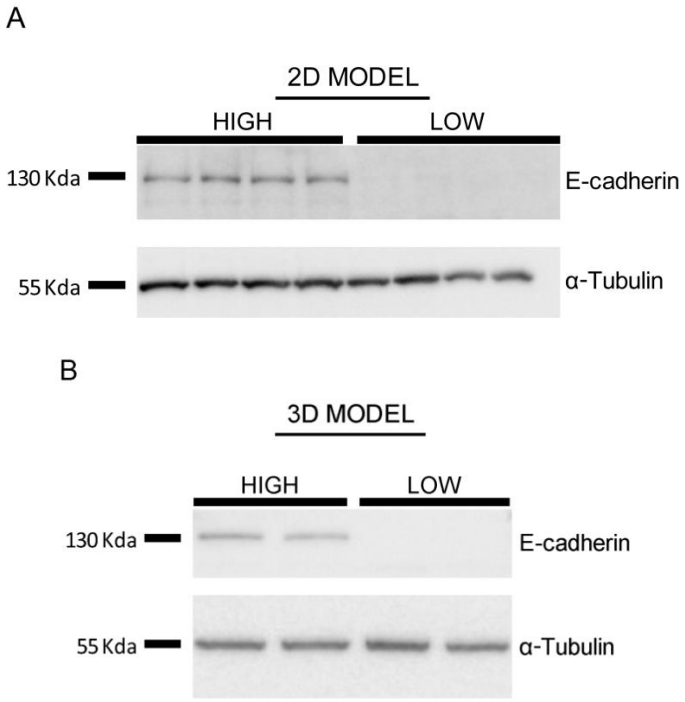

Figure 39. Increase of CDH1 level in βTC4 highly invasive cells and spheroids. (A) Lysates prepared with *high* and *low* cells from 2D model (n=4). α-Tubulin was used as housekeeping gene. **(B)** Lysates prepared with *high* and *low* cells from 3D model (n=2). α-Tubulin was used as housekeeping gene.

Therefore, our highly and less invasive 2D and 3D models were shown to be dependent of CDH1 expression to promote invasion effect. These results corroborate with our *in vivo* data, in which CDH1 drives collective invasion in control tumors.

2.2 EMT-related genes in RIP1-Tag2 tumors

Since the CDH1 results left open the proteins involved in the collective invasion after the anti-angiogenic treatment, we decided to investigate other possible pathways in this process. For this purpose, a microarray performed by Douglas Hanahan from Swiss Institute for Experimental Cancer Research (ISREC) in Lausanne was kindly given to us for our project. These data detected mRNA expression between two groups. Analysed samples consisted of three RIP1-Tag2 tumors untreated and three RIP1-Tag2 tumors sunitinib treated for 4 weeks. In which the control tumors are associated with low invasiveness phenotype and sunitinib treated tumors with high invasiveness phenotype. To determine signatures which could be associated with genetic upregulation or downregulation in our different phenotypes, we performed the Gene Set Enrichment Analysis (GSEA).

The Gene-Sets approach is a powerful tool to establish sets of related genes or pathways that are functionally associated with a disease phenotype. Thus, GSEA was a useful instrument in our case to associate different pathways with tumor invasion capacity in RIP1-Tag2 model. The false discovery rate (FDR) was used to correct for multiple comparisons and gene set sizes. We compared our RNA sequencing results using different databases available at Molecular Signatures DataBase (MolSigDB).

Interestingly, highlighted the signature defining *Epithelial-mesenchymal transition* (pvalue<0.001) from *Hallmark Gene Sets collection* (**Figure 40A-B**), in which RIP1-Tag2 tumors untreated were revealed downregulated in this pathway, while R2 treated tumor samples was not showed a positive enrichment score in all genes analysed (ES) in none genes analysed. Specifically, some genes

previously described as pancreatic cancer EMT markers (Beuran et al. 2015) such as Vimentin, Fibronectin, Collagen (I) and (III) were also observed to be downregulated in treated tumors in sunitinib treated tumors in comparison with control tumors (**Table 17**).

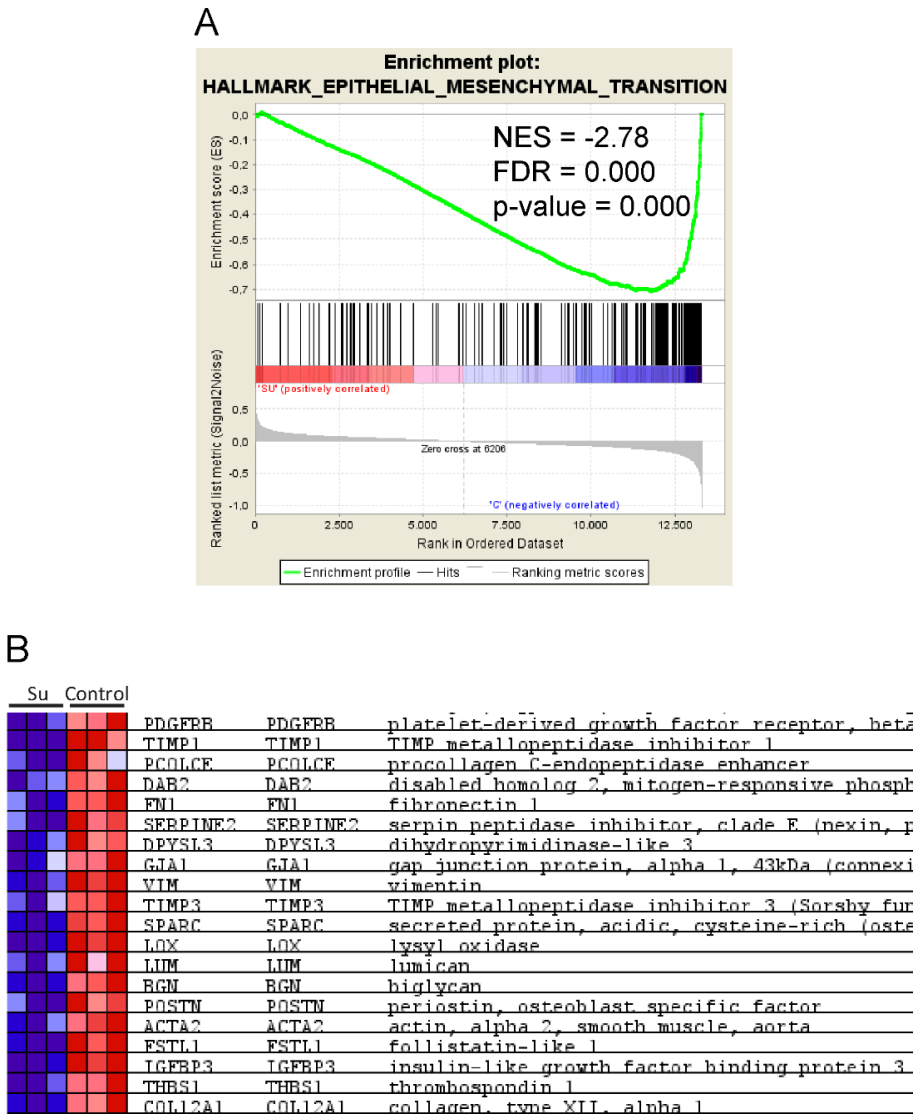

Figure 40. GSEA results demonstrated that control and sunitinib RIP1-Tag2 treated tumors were negatively correlated with *Hallmark epithelial mesenchymal transition signature*. RNA expression data obtained was from three control tumors (C1, C2, C3) and three sunitinib treated tumors during four weeks (SU1, SU2, SU3). Significant enrichment of 93 genes in *Hallmark epithelial mesenchymal transition set* was observed. **(A)** *Hallmark epithelial mesenchymal transition enrichment* plot. Red bars indicate genes expressed preferentially in sunitinib RIP1-TAG2 treated tumors. Purple bars indicate genes overexpressed in control tumors. **(B)** Top 20 leading edge genes in the heat map of gene expression from control and sunitinib treated samples corresponding to the *Hallmark epithelial mesenchymal transition* pathway (red: increased expression; blue: decreased expression).

Table 17. Pancreatic cancer EMT markers enriched on samples from untreated RIP1-TAG2 tumors compared to sunitinib treated tumors. Relation between RNA levels tumors untreated RIP1-TAG2 tumors and sunitinib treated tumors in fold change and T-test.

GENE SYMBOL	DIFFERENCE SU - CTRL	FOLD CHANGE	MEAN CONTROL	MEAN SU	T-test
VIM	-1,6295	0,8239	9,2511	7,6216	0,0004
FN1	-1,5325	0,8371	9,4091	7,8766	0,0022
ITGA5	-0,3768	0,9461	6,9885	6,6116	0,1156
COL1A1	-1,1385	0,8905	10,3969	9,2584	0,0059
COL3A1	-1,4257	0,8487	9,4219	7,9962	0,0045
TGFB1	-1,1431	0,8665	9,2511	7,6216	0,0086

On the other hand, in *Canonical Pathways collection*, two gene sets involving cell junction function presented a high correlation with our data. Results from GSEA, showed an upregulation of genes into *Reactome Cell-Cell Junction Organization* (pvalue>0.05) and *Reactome Tight Junction Organization* (pvalue<0.01) signatures in control tumors compared to treated tumors (**Figure 41**).

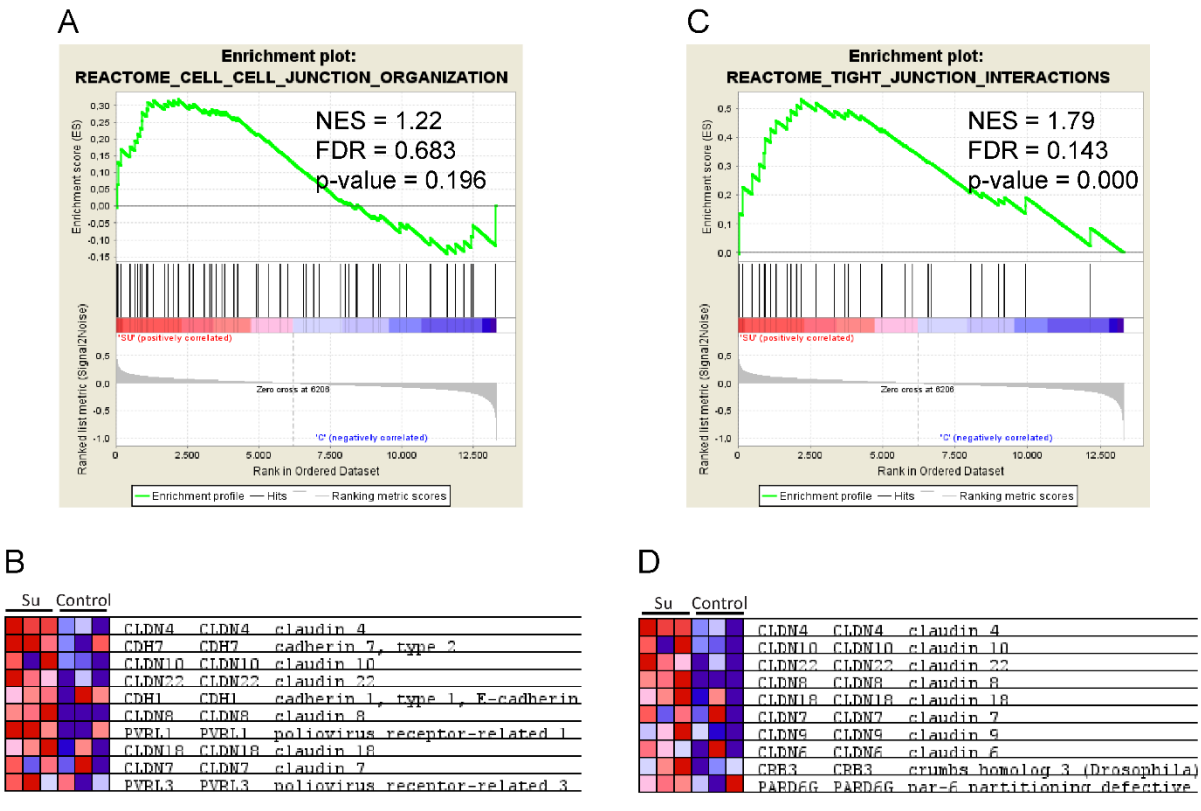

Figure 41. Cell junctions signatures were positively correlated with our data set by GSEA analysis. RNA expression data obtained was from three control tumors (C1, C2, C3) and three sunitinib treated tumors for four weeks (SU1, SU2, SU3). In enrichment plots red bars indicate genes expressed preferentially in sunitinib RIP1-TAG2 treated tumors. Purple bars indicate genes

overexpressed in control tumors. **(A)** Enrichment plot from *Reactome cell cell organization*; GSEA analysis showed significant enrichment of 16 genes in this signature. **(B)** Heat map showed the leading 10 genes that contribute more to the enrichment score. **(C)** Enrichment plot from *Reactome tight junction interactions*; GSEA analysis showed significant enrichment of 12 genes in this signature. **(D)** Heat map showed the leading 10 genes that contribute more to the enrichment score

Collectively, highly invasive RIP1-Tag2 tumors post-treatment decrease EMT related genes expression and increase gene expression of proteins associated with cell-cell binding function. In addition, there is a tendency of increases CDH1 level in untreated invasive tumors. However, the relation between CDH1 and invasiveness was not completely confirmed in RIP1-Tag2 treated tumors.

3. Collective invasion candidates

3.1 Barrier claudins as collective proinvasion markers in RIP1-Tag2 tumors

The results obtained guided us to the hypothesis that other molecular mechanisms act together with CDH1 in PanNETs cell collective Behaviour. Thus, following steps were focalized in validate the differential expression of candidates collective invasion marker in *in vitro high* and *low* βTC4 spheroids (2D, 3D), *in vivo* RIP1-Tag2 model before and after the anti-angiogenic treatment and clinical data from non-malignant primary tumor, malignant primary tumor and metastasis.

To describe other molecules able to orchestrating RIP1-Tag2 tumor collective invasion, we used GSEA analysis data previously described by Microarray technique. As mentioned earlier, were compared RNA data from three control tumors and three sunitinib treated tumors. Since control tumors are related as lower invasive and sunitinib treated tumors as highly invasive, the invasive phenotype demonstrated to be positively correlated (pvalue<0.01) with genes from tight junctions pathway (**Figure 42A**). Indeed, 12 genes from reactome tight junction interactions presented a positive GSEA core enrichment. Specifically,

mainly genes from claudin family showed upregulated in tumors with high invasion capacity (**Figure 42B**).

A

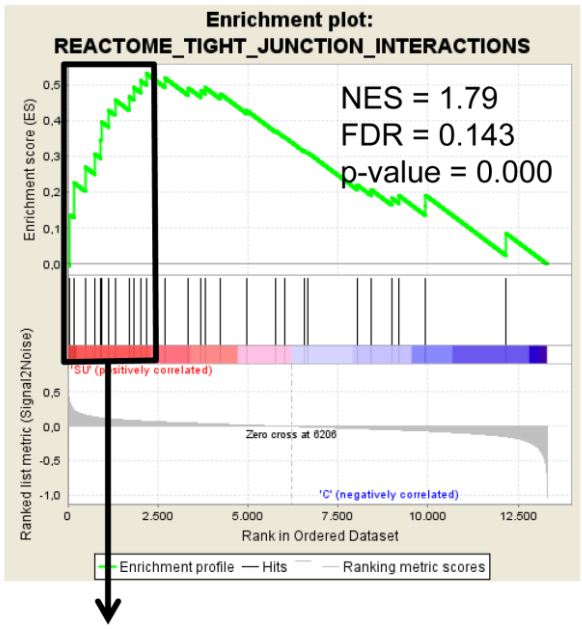

B

LEADING EDGE SUBSET			
	GENE_Symbol	Description	GSEA Core Enrichment
1	Cldn4	Claudin-4, Channel-forming tight junction	Yes
2	Cldn10	Claudin-10, Channel-forming tight junction	Yes
3	Cldn22	Claudin-22, Channel-forming tight junction	Yes
4	Cldn8	Claudin-8, Channel-forming tight junction	Yes
5	Cldn18	Claudin-18, Channel-forming tight junction	Yes
6	Cldn7	Claudin-7, Channel-forming tight junction	Yes
7	Cldn9	Claudin-9, Channel-forming tight junction	Yes
8	Cldn6	Claudin-6, Channel-forming tight junction	Yes
9	Crb3	Crumbs 3, Cell Polarity Complex Component	Yes
10	Pard6g	Par-6 Family Cell Polarity Regulator Gamma	Yes
11	Pard6b	Par-6 Family Cell Polarity Regulator Beta	Yes
12	Cldn15	Claudin-6, Channel-forming tight junction	Yes

Figure 42. Leading edge subsets of genes that contributed most to the enrichment score in *Reactome tight junction interactions transition* pathway are composed mainly by claudins members family. (A) Enrichment plot from Reactome tight junction interations. **(B)** Table of genes enriched in samples from sunitinib treated tumors compared to untreated RIP1-TAG2 tumors.

Claudins are membrane proteins found in tight junctions. According to the functional definition previously described, claudins protein can be generally classified in two groups: barrier-forming or pore-forming. Barrier-forming, are those that predominantly increase transepithelial resistance (TER) or decrease

solute permeability. The second group, pore-forming, are those that predominantly decrease TER or increase solute permeability (Günzel and Yu 2013; Baumgartner et al. 2017) (**Table 18**). Using this classification, we verified claudin RNA expression levels according their functional role in RIP1-Tag2 tumors untreated and sunitinib treated.

Table 18. Claudins isoforms according their functional permeability characteristics.

Barrier-forming claudins		Pore-forming claudins	
↓ permeability to cations	↓ permeability to anions	↑ permeability to cations	↑ permeability to anions
Claudin-1	Claudin-7	Claudin-2	Claudin-7
Claudin-3	Claudin-19	Claudin-10	Claudin-10
Claudin-4		Claudin-15	Claudin-17
Claudin-5		Claudin-16	
Claudin-6			
Claudin-8			
Claudin-9			
Claudin-11			
Claudin-14			
Claudin-18			

Strikingly, when we compared the average RNA expression from barrier-forming claudins *(Cldn1, Cldn3, Cldn4, Cldn5, Cldn6, Cldn8, Cldn9, Cldn11, Cldn14, Cldn18, Cldn19)* with pore claudins (*Cldn2, Cldn10, Cldn15, Cldn17*) higher expression levels of barrier-forming claudins were found than pore-forming claudins in all tumors independent of the treatment applied (**Figure 43**). It is to be noted that this analysis was performed excluding Claudin-7 results, given that its function does not well establish between pore and barrier role.

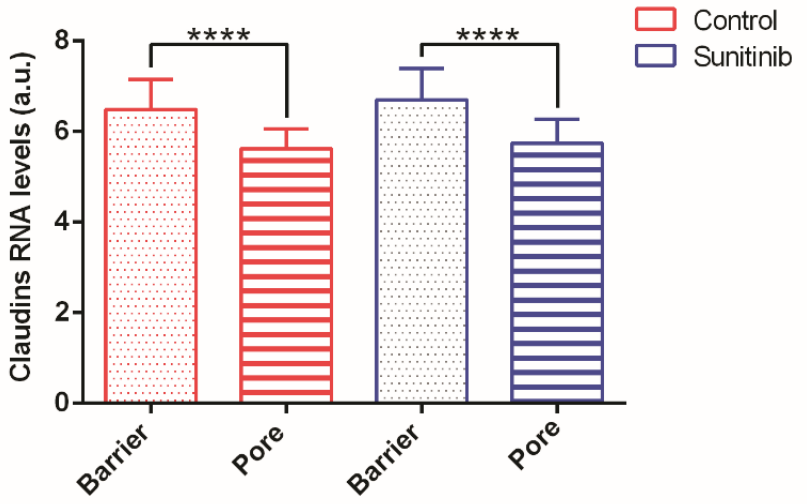

Figure 43. Barrier-forming claudins stood out in RIP1-TAG2 tumors. RNA average expression from barrier-forming claudins *(Cldn1, Cldn3, Cldn4, Cldn5, Cldn6, Cldn8, Cldn9, Cldn11, Cldn14, Cldn18, Cldn19)* is higher than pore-forming *(Cldn2, Cldn10, Cldn15, Cldn17)* claudins before and after anti-angiogenic treatment. Error bars represent S.D. Difference statically significant ($p<0,0001$) by Mann-Whitney test.

In order to decipher whether the anti-angiogenic treatment affect the claudins pattern expressed, we decided taking into account claudin expression differences between untreated and sunitinib treated tumors. To this aim, we checked claudin fuctions from the leading edge genes determined by GSEA analysis.

Among the most enriched genes in tumors treated with sunitinib in respect to the control tumors are: (41.68%) barrier-claudins, (16.66%) pore-claudins, (16.66%) claudins without well-defined function and, (25%) other molecules that are not part of the claudin family. Therefore, the barrier claudin represent almost half of the leading edge genes enriched in treated tumors (Figure 23).

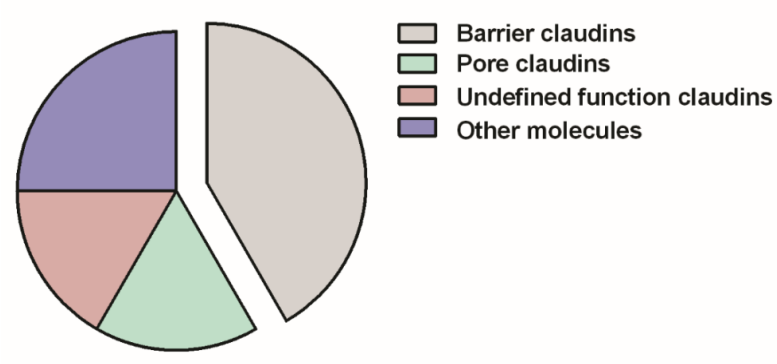

Figure 44. Barrier-claudins forming group represented almost half of leading edge genes enriched in treated tumors. Leading edge genes determined by GSEA analysis were divided by groups: (41.68%) barrier-claudins, (16.66%) pore-claudins, (16.66%) claudins without well-defined function and, (25%) other molecules. Percentage of genes was calculated considering the 12 genes from *Reactome tight junction interactions* that presented a positive GSEA core enrichment.

Overall, these data suggests that barrier-claudins should play an important role in both RIP1-Tag2 tumors before and after anti-angiogenic treatment. Thus, we hypothesize that barrier-forming claudins could be part of mechanisms responsible to collective invasion observed in RIP1-Tag2 tumors. To determine, which more relevant barrier-forming claudins in this context, we compared expression differential between untreated and sunitinib treated tumors for each barrier-forming claudin (**Figure 45**).

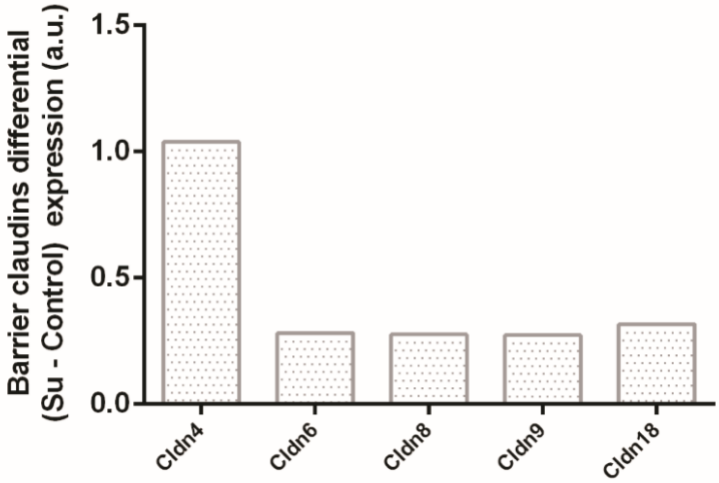

Figure 45. *Cldn4* showed the most difference between untreated and sunitinib treated RIP1-TAG2 tumors in terms of RNA levels. Barrier-forming claudins RNA differential levels (Sunitinib treated tumors – Control tumors) of leading edge genes from GSEA analysis.

As a result, we found that *Cldn4* is the most differentially expressed gene in high invasive tumors treated with sunitinib. To investigate the CLDN4 role in tumor malignancy, the next step was to validate the RNA results also on the protein level.

3.2 CLDN4 expression validation in RIP1-Tag2 tumors

Since CLDN4 was identified as a possible collective invasion marker in RIP1-Tag2 tumors, we decided to elucidate its protein expression through protein level intensity, intratumoral localization and finally by RNA levels. When we compared, eight untreated tumors and eight sunitinib treated tumors, we found that the CLDN4 intensity increases significantly when animals RIP1-Tag2 were treated with sunitinib for 4 weeks (**Figure 46**).

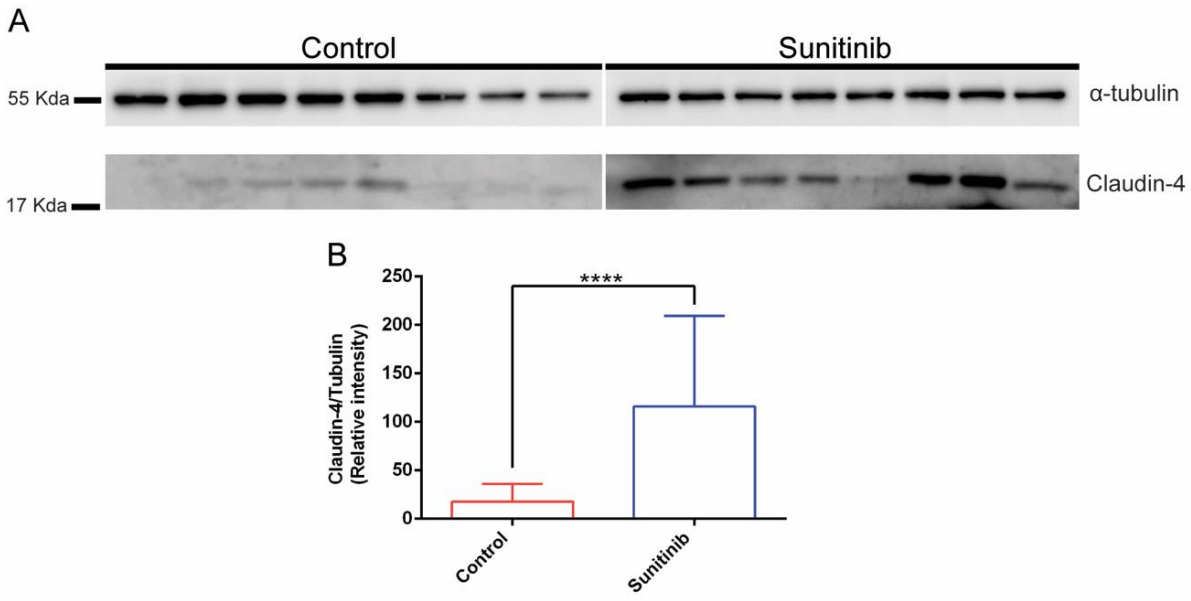

Figure 46. Increase in CLDN4 expression in RIP1-Tag2 tumors treated with sunitinib. CLDN4 detection by western blot from lysates of seven control tumors and seven tumors treated during 4 weeks with sunitinib (both 16 weeks of age). α-Tubulin was used as housekeeping gene. Error bars represent S.D. Difference stastistically significant (p<0,0001) by Mann-Whitney test.

During CLDN4 validation, we also verified CLDN4 levels in RIP1-Tag2 animals treated with DC101 and controls. DC101 is an anti-angiogenic treatment (Anti-VEGFR2 blocking antibody) in which previous findings from our group showed beneficial short-term effects in RIP1-Tag2 tumors.

However, animals DC101 treated after consecutive weeks presented an adaptive resistance that promotes increased local invasion (section 6.1). Our findings demonstrated a relation between DC101 anti-angiogenic treatment and an intensity increase of CLDN4 levels in relation to untreated animals (**Figure 47**).

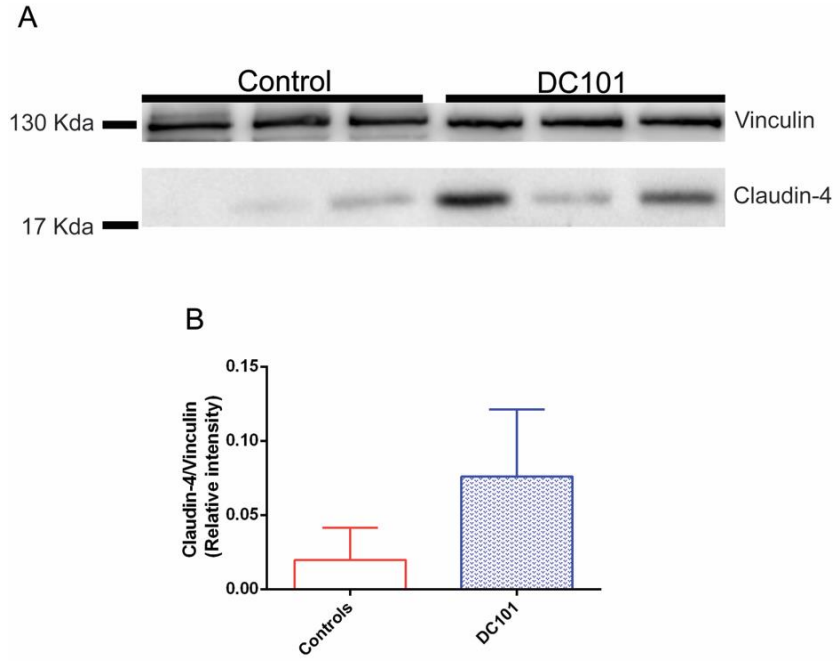

Figure 47. Increase in CLDN4 expression in RIP1-TAG2 tumors treated with DC101. CLDN4 detection by western blot from lysates of seven control tumors and seven tumors treated during 4 weeks with DC101 (both 16 weeks of age). α-Tubulin was used as housekeeping gene. Error bars represent S.D.

To localize the expression of CLDN4 in RIP1-Tag2 tumors, we performed an immunohistochemistry assay in control and sunitinib treated tumor samples. The immunohistochemistry staining showed clear intratumoral heterogeneity of CLDN4 expression pattern, so, this protein did not distribute in all tumor zones with the same intensity. Consequently, CLDN4 quantification was performed taking to account three tumor zones, (i) invasive tumor front, (ii) encapsulated tumor front, and (iii) tumor center. The CLDN4 immunohistochemistry quantification method was similarly to applied to CDH1 (Figure 15), however, in this case, including tumor center areas.

Notably, RIP1-Tag2 tumors before anti-angiogenic treatment demonstrated a CLDN4 expression increases in invasive front in relation to the center zone (**Figure 48A**). In addition, was verified a correlation between the high tumor invasion capacity and the increase CLDN4 protein expression (**Figure 48B**). B). Regarding the tumor after anti-angiogenic treatment, sunitinib tumors treated showed significantly more CLDN4 intensity on the invasive fronts than on the encapsulated fronts and tumor center (**Figure 48C**). Furthermore, these tumors conferred a high tendency to correlate the global invasion capacity and CLDN4 expression (**Figure 48D**).

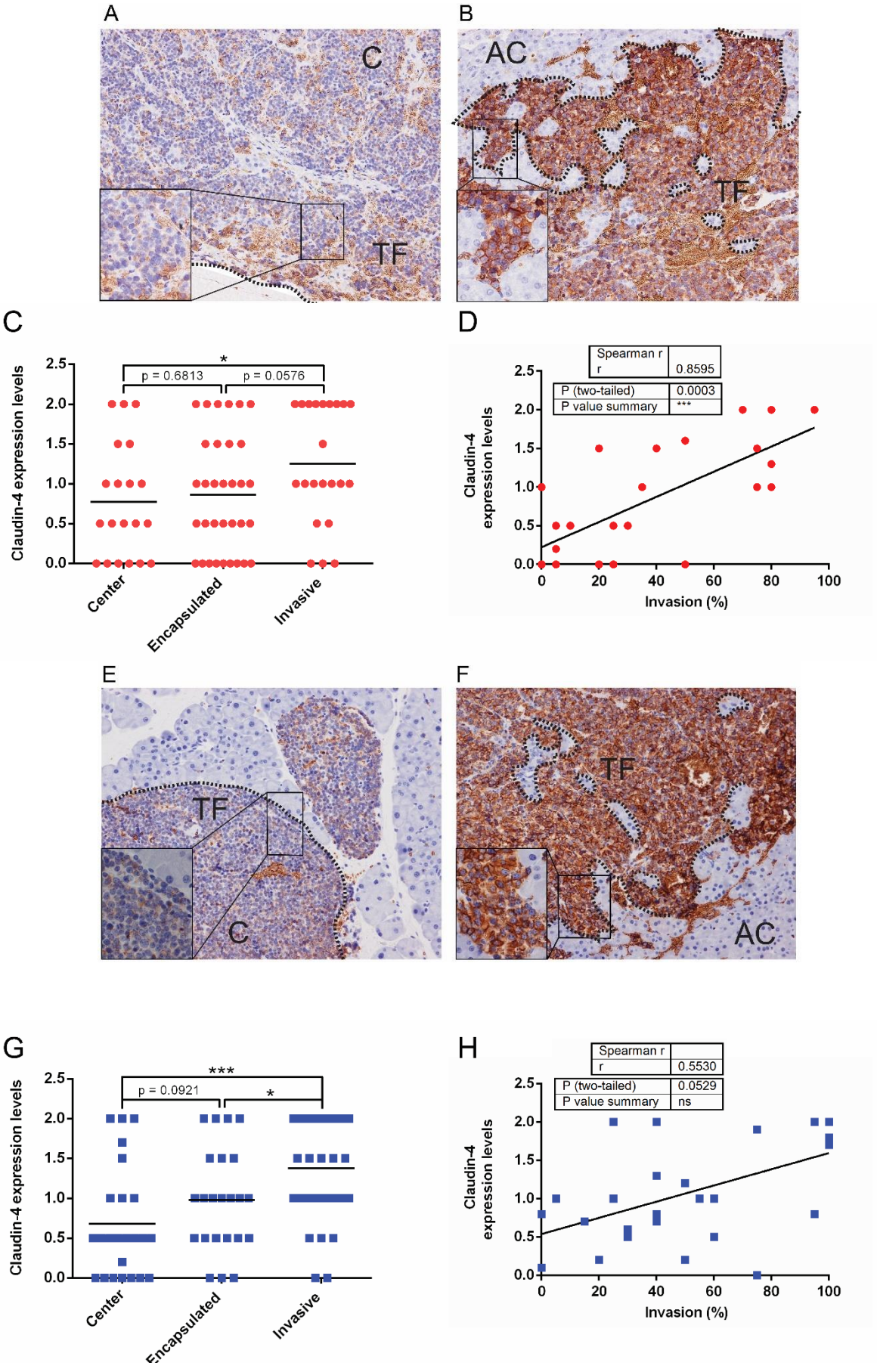
A
C
TF
B
AC
TF
C
Claudin-4 expression levels
2.5
2.0
1.5
1.0
0.5
0.0
*
p = 0.6813
p = 0.0576
Center
Encapsulated
Invasive
D
Spearman r
r
0.8595
P (two-tailed)
0.0003
P value summary
***
Claudin-4 expression levels
Invasion (%)
0
20
40
60
80
100
E
TF
C
F
TF
AC
G
Claudin-4 expression levels
***
p = 0.0921
*
Center
Encapsulated
Invasive
H
Spearman r
r
0.5530
P (two-tailed)
0.0529
P value summary
ns
Claudin-4 expression levels
Invasion (%)

Figure 48. CLDN4 as an invasion marker in RIP1-TAG2 tumors before and after the anti-angiogenic treatment. Immunohistochemistry was performed on RIP1-TAG2 tumor tissue at 16 weeks of age, untreated or treated with sunitinib for 4 weeks (C=Tumor Center; Ac=Acinar Tissue; TF=Tumor Front). Representative images at 20X. Significance was verified by Mann Whitney test. Spearman correlations were used to assess associations between continuous variables. **(A)** Control non-invasive tumor and **(B)** Control invasive tumor. **(C)** Invasive fronts (n=22) showed more CLDN4 levels in periphery than tumor center (n=20) **(D)** CLDN4 expression levels center and periphery tumor zones (n=24) were highly correlated with high tumor invasion capacity**. (E)** Sunitinib treated non-invasive tumor. **(F)** Sunitinib treated invasive tumor. **(G)** CLDN4 protein levels in invasive tumor fronts (n=33) was higher than encapsulated tumors (n=23) and tumor center (n=26) **(B)** Sunitinib treated RIP1-TAG2 tumors presented positive correlation almost significantly between the expression of CLDN4 and global high tumor invasion capacity (n=27).

In the next step, tumors were classified according to their invasion capability as IT, IC1 and IC2, and CLDN4 intensity levels was determined per tumor. The results demonstrated an increase in CLDN4 expression in highly invasive tumors in both, control and sunitinib treated tumors. However, no significant differences were observed to be determined only by the treatment and independent of the invasion capacity (**Figure 49**). These data indicate that CLDN4 is one of the main protein that acts in collective invasion in RIP1-Tag2 tumors before and after the anti-angiogenic treatment.

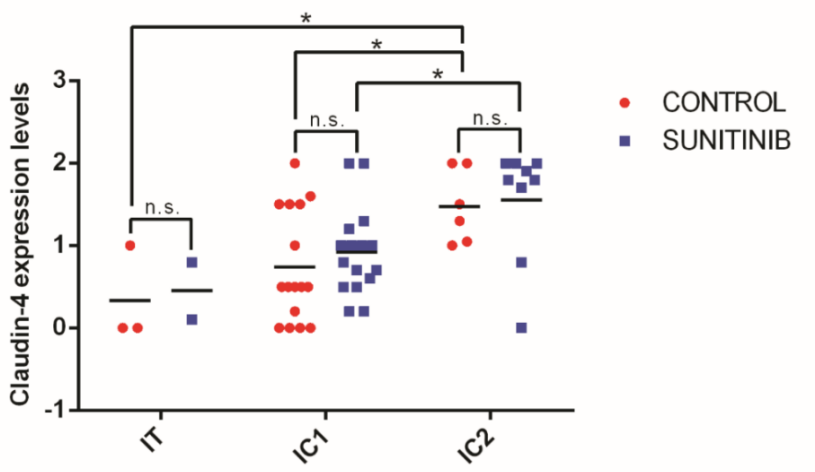

Figure 49. Both control tumors and sunitinib treated tumors increased CLDN4 levels in widely invasive tumors (IC2). CLDN4 immunohistochemistry was performed on RIP1-TAG2 tumor tissue at

16 weeks of age, untreated or treated with sunitinib for 4 weeks. IT control (n=3), IT sunitinib (n=2); IC1 control (n=16), IC1 sunitinib (n=16); and IC2 control (n=6), IC2 sunitinib (n=9)

Finally, these results were confirmed by RNA levels. Then, results obtained by Taqman® Real-Time PCR from RIP1-Tag2 tumors data revealed low *Cldn4* levels in control samples. Interestingly, all tumors after anti-angiogenic treatment increased *Cldn4* expression on at least seven times in relation to control tumors (**Figure 50**). These results demonstrated that this increase of *Cldn4* expression in RIP1-Tag2 tumors occurs at the translational level.

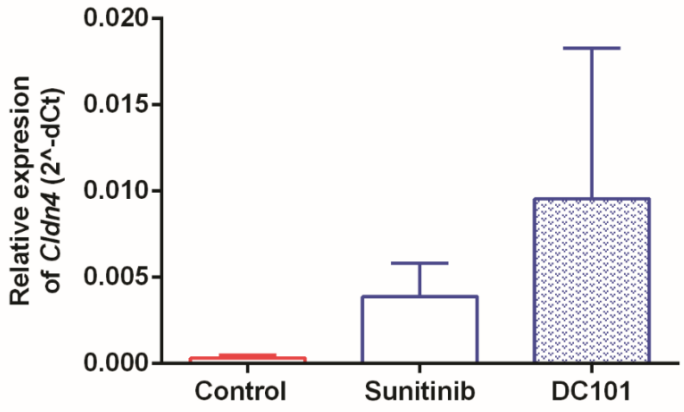

Figure 50. Sunitinib and DC101 anti-angiogenic treatments leaded an increase RNA expression of *Cldn4* in RIP1-Tag2 tumors. Results obtained from Taqman® Real-time PCR of two control tumors and two tumors treated for 4 weeks with sunitinib or DC101 (both 16 weeks of age). RNA quantification of *Cldn4* was normalized by β-actin measured by 2^-ΔCT. **(A)** RNA expression level of RIP1-Tag2 tumors untreated (n=2), treated with sunitinib (n=2) and treated with DC101 (n=2).

Altogether, these results confirmed an increase *Cldn4* RNA and protein levels in highly invasive tumors. In addition, CLDN4 protein was found located on the invasive tumor fronts, whether controls or treated. Due to these encouraging results, the next step was to verify CLDN4 presence in our *in vitro* models for later CLDN4 modulation on functional assays.

3.3 Barrier claudins in βTC4 2D and 3D model *in vitro* model

In order to verify *in vitro* CLDN4 presence in βTC4 cells in 2D model we performed the western blot technique. In fact, we were surprised with not expression of CLDN4 in both *high* and *low* βTC4 cells (**Figure 51A**). Additionally, results from immunofluorescence confirmed CLDN4 absent expression in these cells. It is worth mentioning, that *high* cells showed higher levels of CLDN4 than *low* cells, but even so the CLDN4 levels in both cases were almost nonexistent (**Figure 51B**).

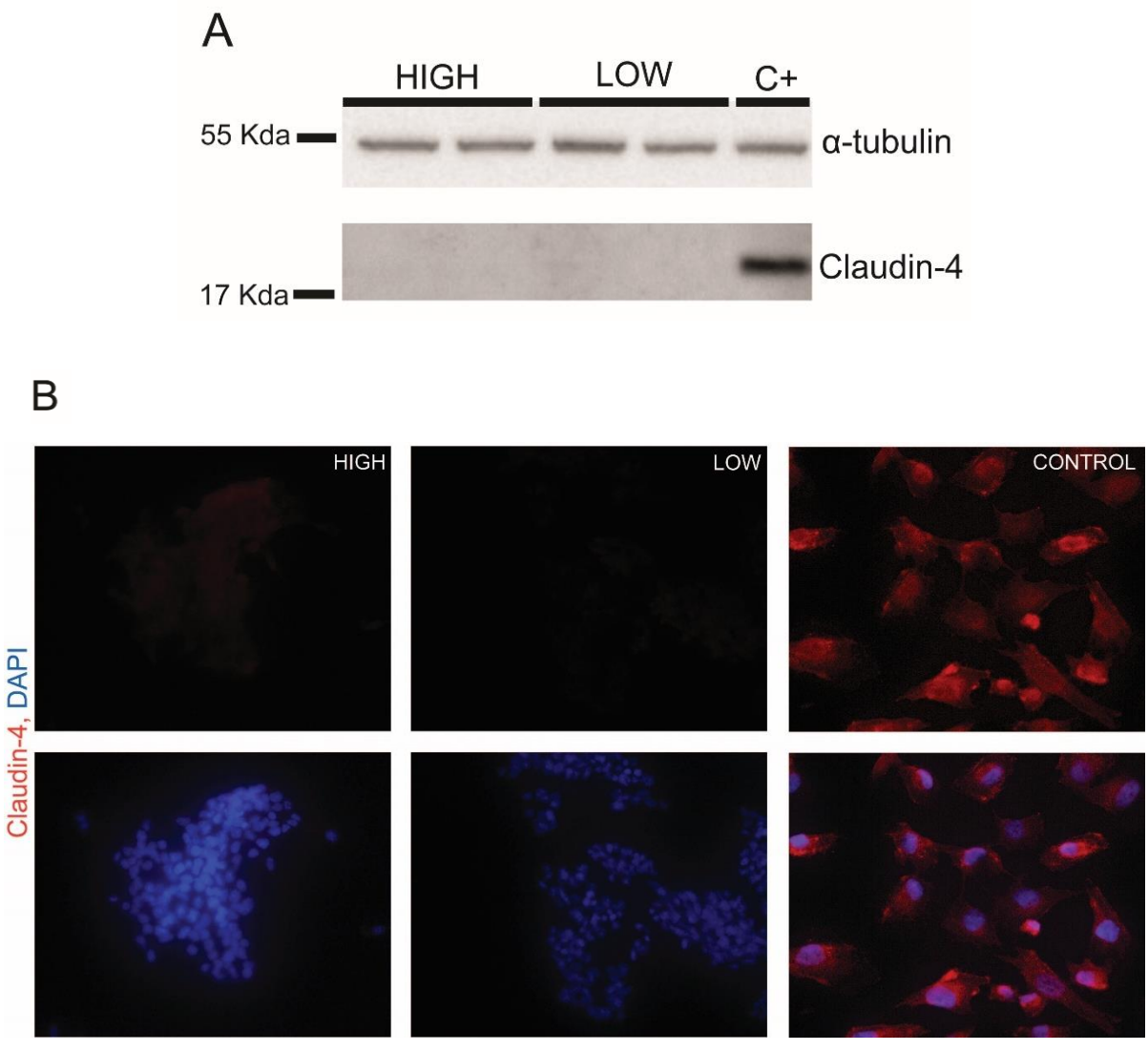

Figure 51. CLDN4 protein could not be detected in any of βTC4 cell subpopulations. (A) Western blot of CLDN4 protein from lysates of the *high* and *low* βTC4 cells in 2D model under normal conditions of βTC4 cells culture. α-Tubulin was used as housekeeping gene. **(B)** Immunocytofluorescence of

CLDN4 in *high* and *low* βTC4 cells (2D model) under normal conditions of βTC4 cells culture. SN12C from renal cell carcinoma was used as positive control of CLDN4. Images at 40X.

It is well known that not all molecules are represented equally in the cells and tumors that originated them, due a microenvironment changes that these cells undergo. This fact has spurred the generation of new 3D culturing techniques that more closely reflect the features of the primary tumors from which they were derived. For this purpose, we analysed CLDN4 protein level in 3D culture. However, *high* and *low* βTC4 spheroids also did not present this protein in three-dimensional architecture (**Figure 52**).

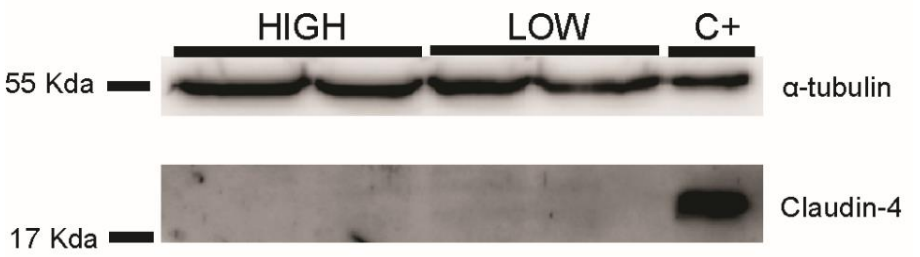

Figure 52. Absence of CLDN4 protein level was verified in *high* and *low* βTC4 spheroids. CLDN4 detection by western blot from two lysates of *high* and *low* BTC4 spheroids in2D model cultured for 3 days in normal βTC4 conditions culture. RIP1-Tag2 control tumor was used as a positive control for CLDN4 protein.

Finally, spheroids βTC4 in 3D conditions were analysed by a Taqman® assay aiming its high RNA levels detection capacity. We noted that both, *high* and *low* subpopulations showed insignificant values in comparison to *Cldn4* positive control represented by RIP1-Tag2 tumor (**Figure 53A**).

A possible explanation for such a low level of CLDN4 would be that in our *in vivo* model CLDN4 induction was observed in RIP1-Tag2 tumors after anti-angiogenic treatment. Thus, we decided to mimic the anti-angiogenic treatment *in vitro* through hypoxia 10% to induce *Cldn4* expression. However, this approach was not efficient to promote *Cldn4* expression (**Figure 53B**).

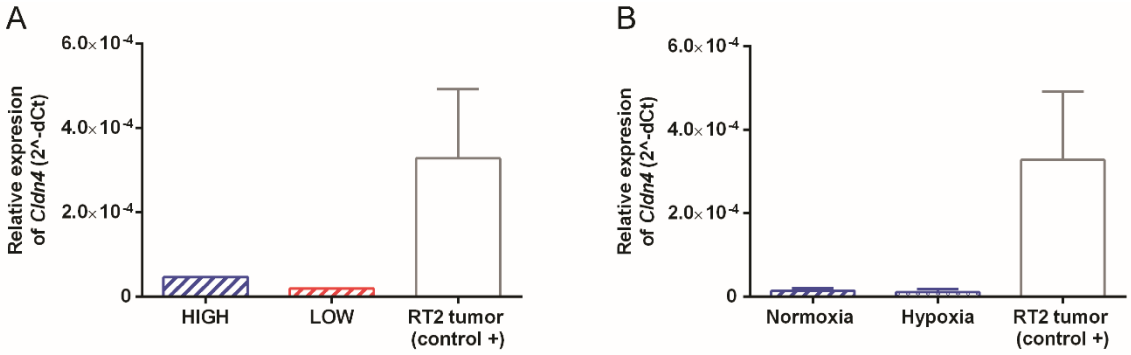

Figure 53. There was almost no relative *Cldn4* expression in *high* and *low* βTC4 spheroids in 3D model. Hypoxia conditions did not induce a CLDN4 expression. Results obtained from a Taqman® Real-time PCR, normalized by *β-actin* and measured by 2^-dCT. Error bars represent S.D. RIP1-Tag2 control tumor was used as a positive control for *Cldn4* expression. **(A)** RNA quantification performed with *high* and *low* βTC4 spheroids in 3D model after three day of invasion. **(B)** RNA quantification performed with *high* βTC4 in 3D model after 24h of hypoxia 10% condition (n=2).

Owing to these results, we tested in 2D model more rigorous treatments to promote CLDN4 induction in βTC4 cells. We combined different hypoxia levels with nutrient deprivation in terms of medium dilution and FBS reduction (**Table 19**) and CLDN4 expression was verified by western blot. Finally, these treatments applied were not able to induce CLDN4 either.

Table 19. CLDN4 induction treatments

Treatment of Claudin-4 induction	Time
Normoxia; 5% FBS	72 hours
Normoxia; 0% FBS	72 hours
Normoxia; 25% nutrients	72 hours
Normoxia; 50% nutrients	72 hours
Hypoxia 3%; 25% nutrients	o/n
Hypoxia 3%; 0% FBS	o/n
Hypoxia 3%; 5% FBS	o/n
Hypoxia 10%; 25% nutrients	48 hours (n.dep.) + 24 hours (hypoxia 10%)
Hypoxia 10%; 50% nutrients	48 hours (n.dep.) + 24 hours (hypoxia 10%)
Hypoxia 10%; 75% nutrients	48 hours (n.dep.) + 24 hours (hypoxia 10%)
6 days medium depletion	6 days
4 days medium depletion	4 days

For the purpose of verification of the possibility that βTC4 cells had lost the CLDN4 expression during its *in vitro* culture, we tested different βTC cell primary

lines with few passages (5-7), developed by our group from distinct RIP1-Tag2 tumors. As we showed in **Figure 54**, none of the primary βTC cells demonstrated the CLDN4 expression.

These results demonstrated that CLDN4 absence *in vitro* is a common characteristic among the four primary lines cultured obtained from different RIP1-Tag2 tumors. Interestingly, as we can see in previous analyses, most of *in vivo* RIP1-Tag2 tumors are CLDN4 positive, even though in low intensity. Thus, our results indicated that there is a loss of CLDN4 when we move from *in vivo* to *in vitro* system.

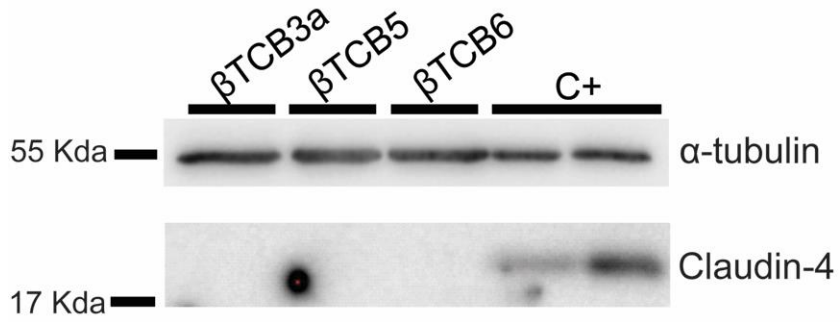

Figure 54. Absence of CLDN4 protein was verified in primary lines from RIP1-Tag2 tumors. Western blot of CLDN4 protein from lysates of three different βTC cell primary lines developed by our group. RIP1-Tag2 tumors were used as CLDN4 positive controls. α-Tubulin was used as housekeeping gene.

Considering that we were not able to detect CLDN4 in any approaches used in our *in vitro* model, we decided to elucidate which barrier-forming claudins, apart from CLDN4, could be acting in βTC4 cell invasion process. In this way, was performed a screening of the presence of barrier-forming claudins in βTC4 cells by western blot technique.

Among all claudins verified (data not shown), CLDN1 was found expressed in *high* cells and almost not expressed in *low* cells (**Figure 55A-B**). These results were also validated by immunofluorescence. The immunofluorescence images make us speculate that the leader migratory cells are the ones that most present CLDN1 (**Figure 55C** white arrows).

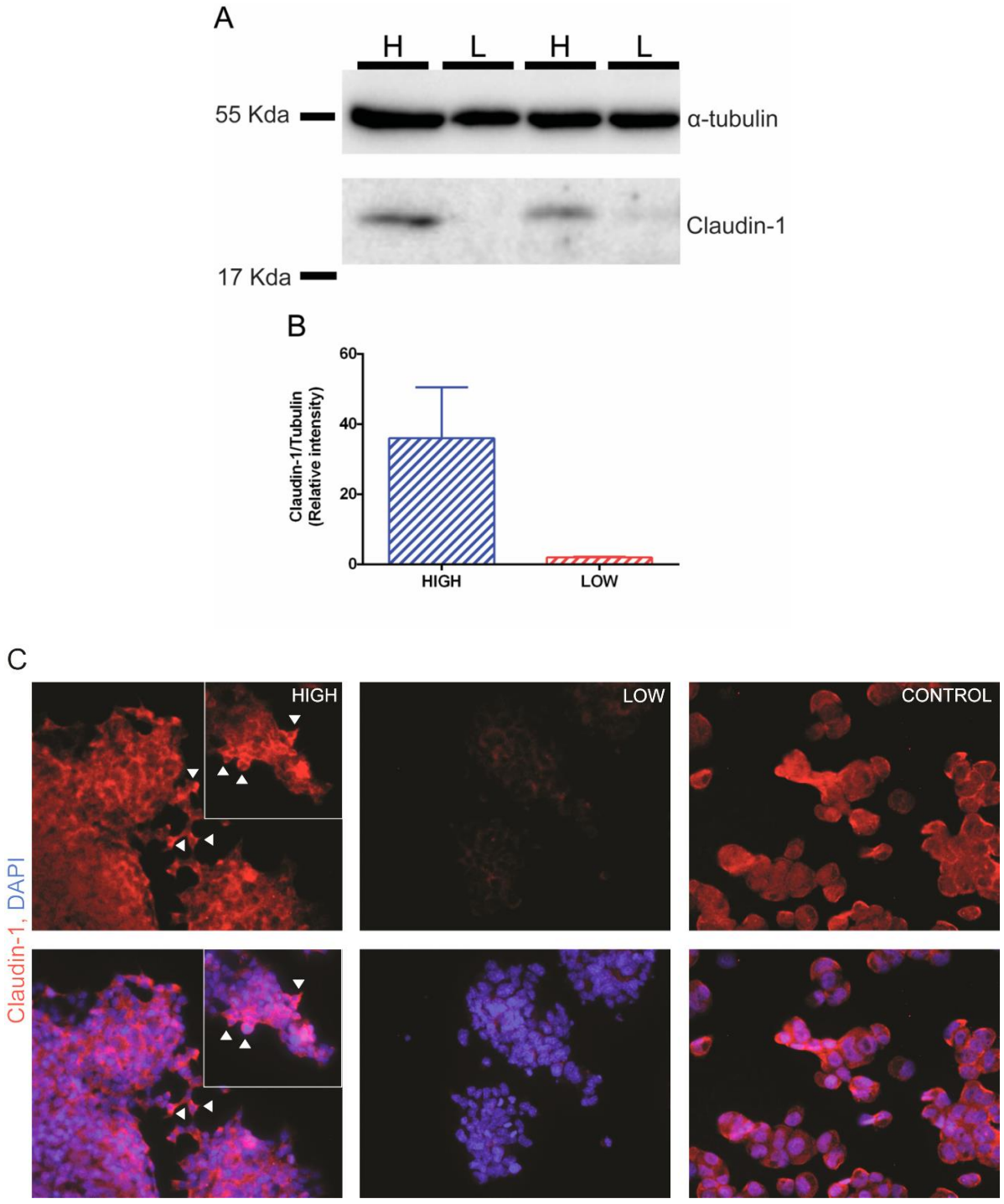

Figure 55. Increase in CLDN1 protein level was detected in highly invasive phenotype of βTC4 cells. (A) CLDN1 detection by western blot from two lysates of *high* and *low* βTC4 cells in 2D model in normal βTC4 conditions culture. **(B)** Western blot quantification by relative intensity. α-Tubulin was used as a housekeeping gene. Error bars represent S.D. **(C)** Immunocytofluorescence of CLDN1 protein in βTC4 *high* and *low* cells in 2D model (40X). Leader migrating cells seems express high levels of CLDN1 (white arrows). Ren13 cells were used as control of CLDN1 protein expression.

To confirm ECM's role in relation to CLDN1 expression in βTC4 spheroids, we verified this protein in 2D and 3D models using *high* and *low* spheroids. Interestingly, *low* spheroids that in 2D showed very *low* levels of CLDN1 when in 3D model acquired this protein without change CDH1 levels. Thus, *low* spheroids seem to recruit CLDN1 in presence ECM, when spheroids are embedded in three-dimensional culture environment to promote their invasion (low levels) without the help of CDH1 (**Figure 56**).

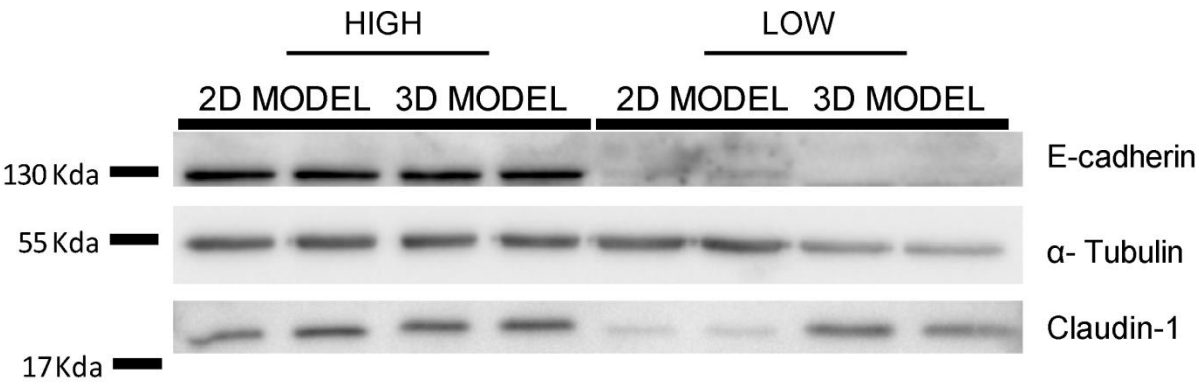

Figure 56. The three-dimensional culture environment increased CLDN1 levels in *low* βTC4 spheroids. CLDN1 and CDH1 detection by western blot from two lysates of *high* and *low* βTC4 cells/spheroids in 2D model and 3D model at normal conditions of culture. βTC4 spheroids were incubated in three-dimensional culture (Matrigel®) for 3 days and after was generated a lysate. α-Tubulin was used as housekeeping gene.

To further describe the barrier claudins role in *in vitro* and *in vivo* model, we decided to compare both samples in a single analysis. For this, we verified the protein level in *high* and *low* βTC4 cells and RIP1-Tag2 tumors untreated and sunitinib treated.

As expected, βTC4 cells showed, again, an absence of CLDN4, while RIP1-Tag2 untreated and treated tumors expressed CLDN4. However, highly invasive treated tumors had increased CLDN4 levels (**Figure 57A**).

On the other hand, CLDN1 protein was not detected untreated and treated tumors, its presence was verified only in βTC4 cells. It is important to highlight the high differential observed between *high* and *low* subpopulations, in which the high

invasive phenotype showed higher CLDN1 expression level than low invasive phenotype (**Figure 57B**).

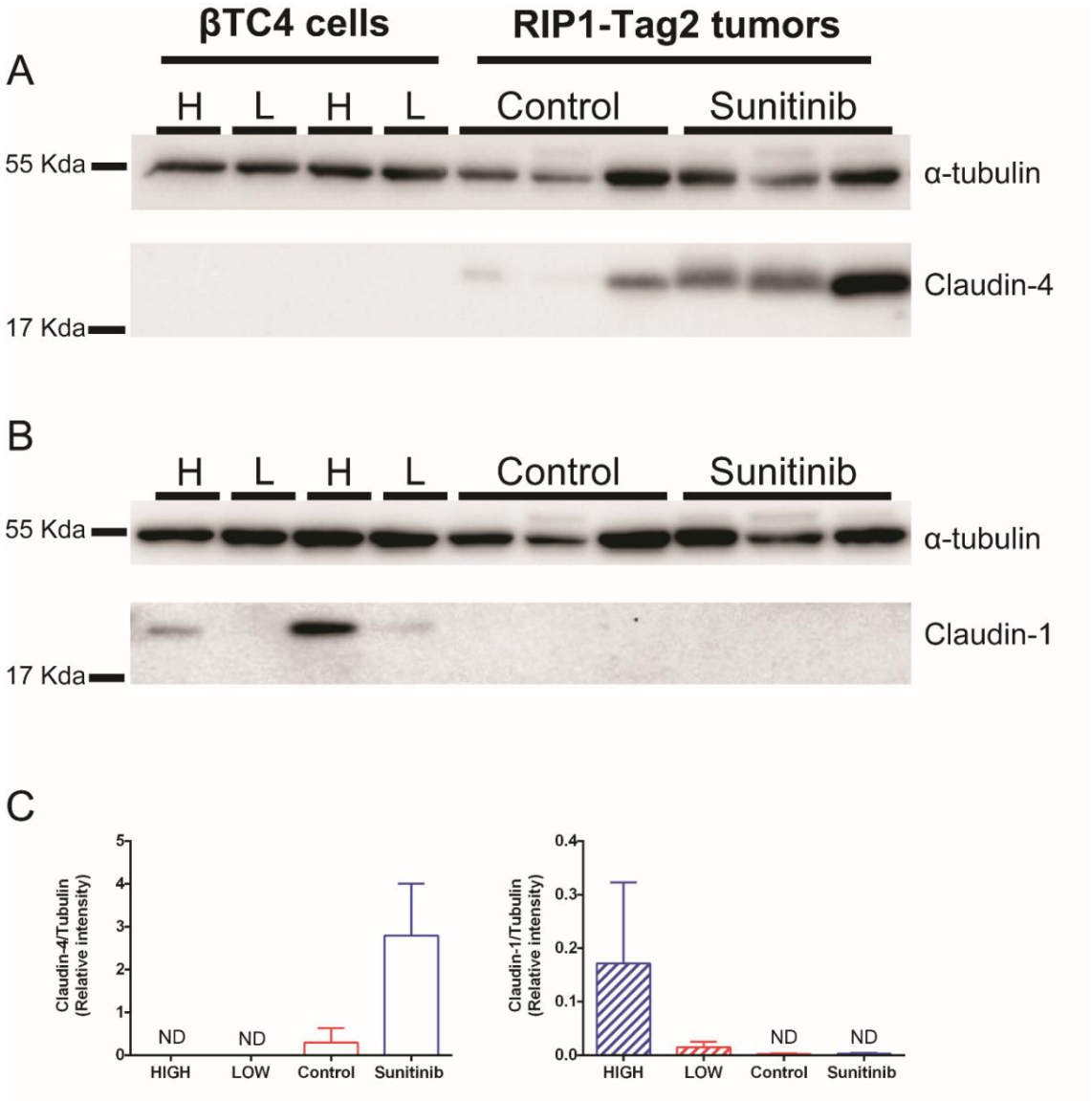

Figure 57. Claudin1/4 barrier-forming as collective invasion mechanism in RIP1-Tag2 tumors and βTC4 cells. Western blot from lisates of *high/low* βTC4 cells 2D model, and untreated/treated RIP1-Tag2 tumors, two per condition. **(A)** Invasive tumors from RIP1-TAG2 increase CLDN4 levels. CLDN4 protein was not detected in βTC4 cells. **(B)** Highly invasive cells showed higher expression of CLDN1 than *low* invasive cells. None of the RIP1-Tag2 tumors presented CLDN1 protein expression. **(C)** Western blot quantification by relative intensity. α-Tubulin was used as housekeeping gene. Error bars represent S.D. Graphics demonstrated an barrier-claudins proteins switch that occurs in PanNETs in vitro and *in vivo* model.

Altogether, these results indicate that, CLDN1 and CLDN4 barrier claudins suffer a molecular switch between them in our *in vitro* and *in vivo* models. Specifically, CLDN1 acts in βTC4 model and CLDN4 in RIP-Tag2 model, being that both are more express according with the tumoral invasiveness increase. Moreover, both proteins perform the same sealing function, maintaining cell-cell junction dynamic integrity allowing the cell collective invasion, during the invasion process in βTC4 cells and RIP-Tag2 tumors (**Figure 58**).

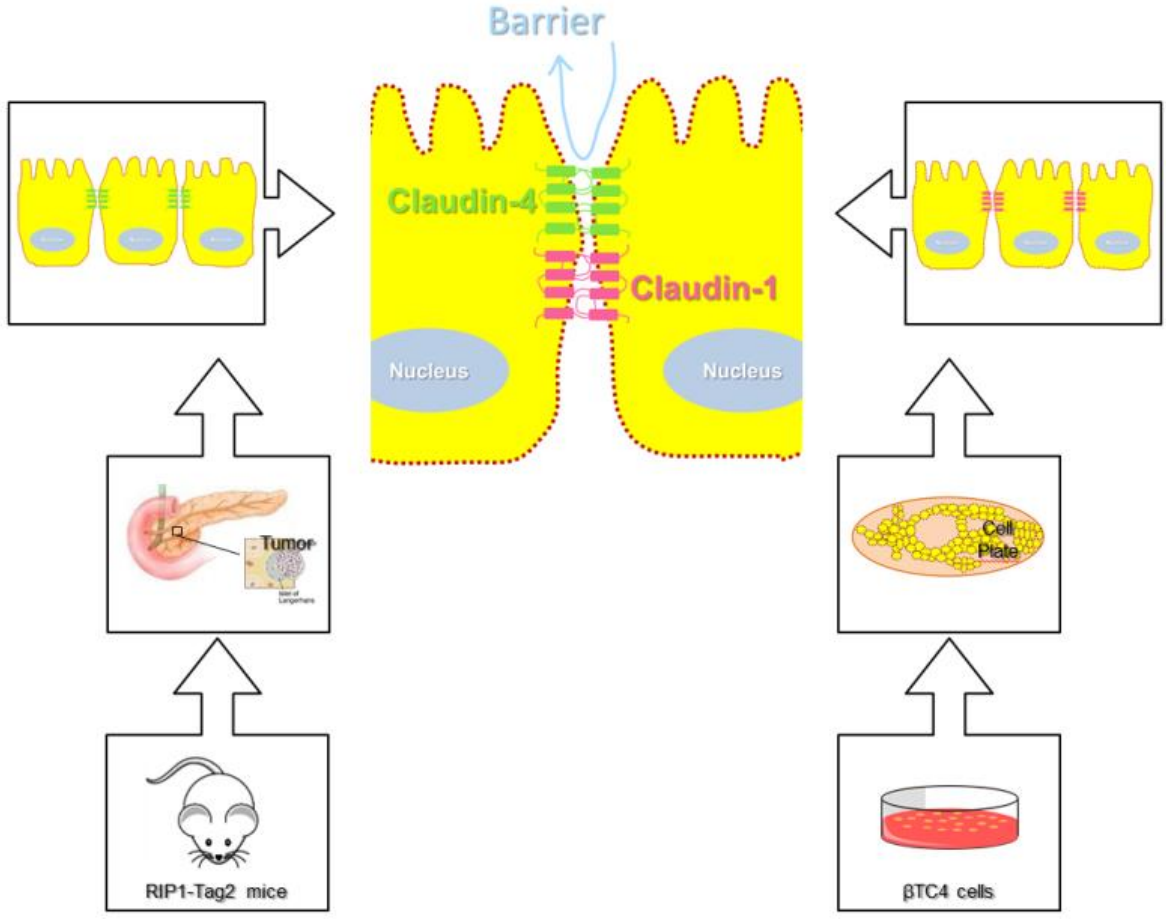

Figure 58. Molecular switch of barrier claudins (1/4) in our *in vivo* and *in vitro* model. Schema detailing the CLDN4 presence in neuroendocrine tumors from RIP1-Tag2 pancreas (left side). As well as, CLDN1 existence in βTC4 cells derived of RIP1-Tag2 tumor, after undergoing culture *in vitro* (right side). Finally, although CLDN1 and CLDN4 being different proteins, both show the same barrier function, capable of sealing two neighboring cells.

4. CLDN1 functional *in vitro* validation

4.1 CLDN1 expression in βTC4 cells exposed to hypoxia and lack of nutrients effects

Previous results demonstrated that anti-angiogenic treatment efficiently decreases the number of tumor vessels essential for the delivery of nutrients and oxygen required for tumor cells proliferation. However, it does not prevent tumor progression, and further, increases of invasion capacity (as described in introduction section).

Therefore, we hypothesized that βTC4 cells sense this “inhospitable environment” and, after a period of adaptation, could be respond up-regulating CLDN1 and increasing their invasion capability. As unfortunately, anti-angiogenics don’t target directly tumor cells, we mimicked the anti-angiogenic treatment mixing different treatments involving: hypoxia (3% and 10%), nutrient deprivation and variations in fetal bovine serum concentration.

Then, in this sense, we chose to repeat exactly the same methodologies applied to promote CLDN4 induction to try induce CLDN1 (**Table 19**). Among all treatments, we observed a clear CLDN1 induction when βTC4 cells were treated for 2 previous days with nutrient deprivation and the last 24 hours with hypoxia 10% (**Figure 59C**).

Therefore, cells exposed to hypoxia, when treated with lack of nutrients responded by up-regulating CLDN1 protein levels (**Figure 59A-B**).

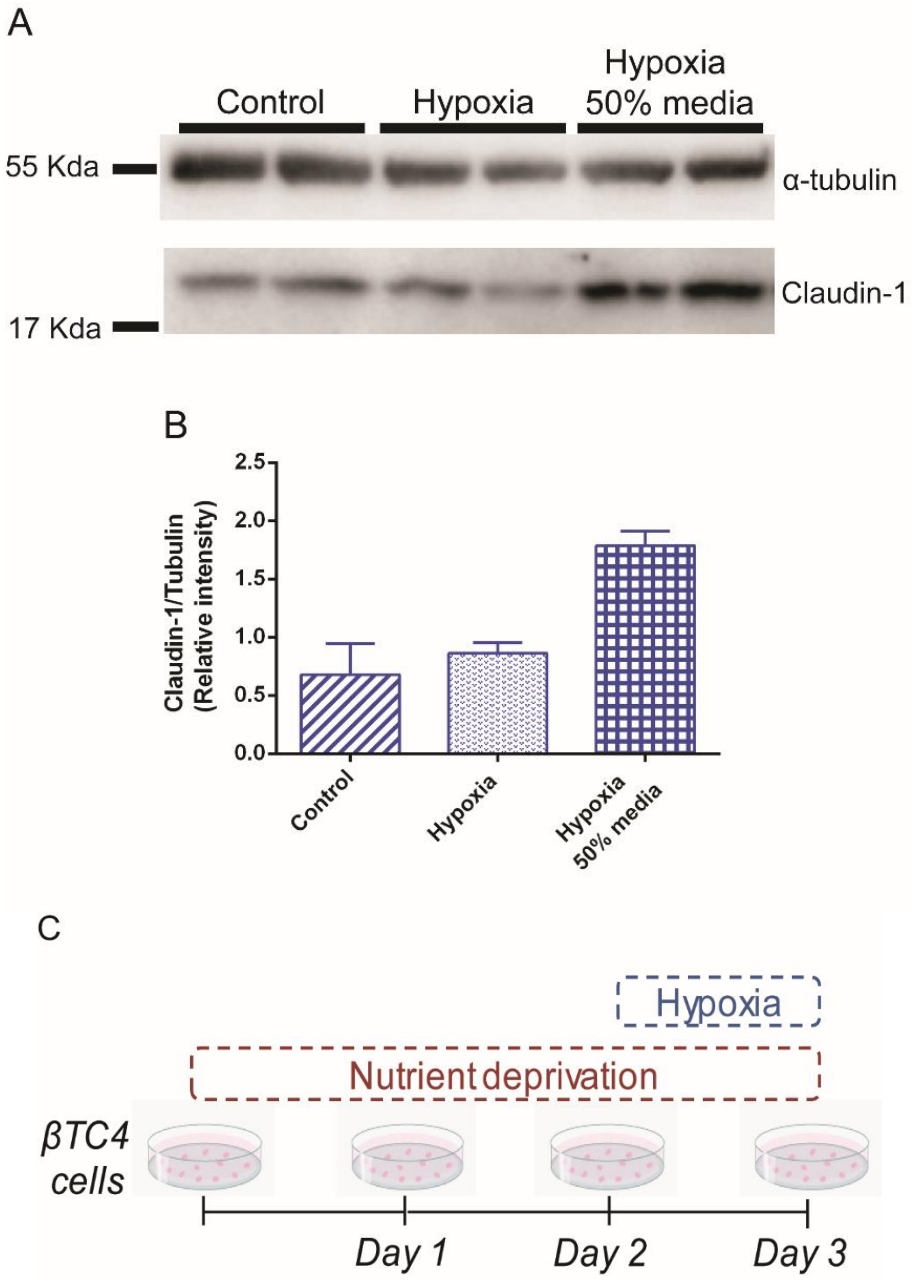

Figure 59. CLDN1 overexpression was observed on βTC4 cells under conditions of hypoxia and nutrient deprivation. (A) CLDN1 detection by western blot from two lysates of *low* βTC4 cells in normal βTC4 conditions culture, βTC4 cells in hypoxia 10% and βTC4 cells in hypoxia 10% plus nutrient deprivation. **(B)** Western blot quantification by relative intensity. α-Tubulin was used as housekeeping gene. Error bars represent S.D. **(C)** Illustration of anti-angiogenic mimic treatment able to induce CLDN1.

CLDN1 is functionally associated with cell-cell contact and the maintenance of cellular polarity. However, the mechanisms driving claudin-mediated cancer invasion and migration remain poorly understood.

Altered expression of CLDN1 protein has been detected in various steps of cancer progression. CLDN1 upregulation was described in colorectal, melanoma, breast, cervical and gastric cancer, while in lung, prostate, gastric, breast and colorectal cancer CLDN1 was verified as downregulated (Kwon 2013; Tabariès and Siegel 2017).

To determine the possible function of CLDN1 up-regulation in PanNETs invasion as a consequence of oxygen and nutrient deprivation, we analysed its effect by Transwell® invasion assay in three conditions:

a) *Control cells in βTC4 DMEM medium (15% FBS).*
b) *Hypoxia 10% treatment in βTC4 DMEM medium (15% FBS).*
c) *Hypoxia 10% treatment in βTC4 DMEM medium (15% FBS) diluted at 50% in PBS*.

Thus, βTC4 *high* cells (5.0 x 105 cells/mL) were plated in conditioned medium βTC4 medium deprived for 24 hours *(a-b)* conditions, or conditioned medium βTC4 medium diluted in 50% conditions (A). All cells were maintained in normoxia conditions at 21% O2, 5% CO2, 37°C for the next 24 hours. After, *(b)* and *(c)* conditions were transferred to a hypoxia chamber at 10% O2, 5% CO2, 37°C and incubated the last 24 hours (**Figure 60**). Thus, totalizing 48 hours of Transwell® assay.

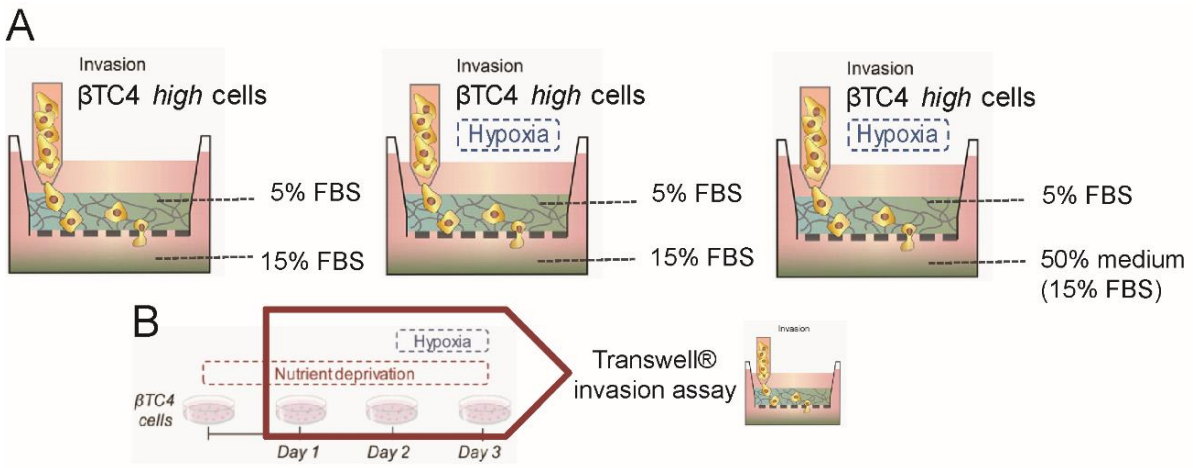

Figure 60. Experimental design of Transwell® invasion assay to verify the CLDN1 induction effects by lack of nutrients and hypoxia 10%.

Obtained results confirmed the relation between the over expression of our candidate and the higher βTC4 cells invasion capacity. Specifically, we reported that only hypoxia conditions were not able to increase the invasion capacity and CLDN1 expression. However, when we combined hypoxia conditions with nutrient reduction, we were able to mimic anti-angiogenic treatment effects in terms of invasion capacity and CLDN1 expression (**Figure 61**).

It is to be noted that βTC4 cells, even if in normal conditions culture, already have a high invasiveness. Knowing that, these cells are of delicate maintenance, the aggressive culture conditions promote, in a first moment, loss of βTC4 invasion capacity.

However, our findings suggest that, if this aggressive treatment is sufficient to mimic anti-angiogenic treatment and overexpress CLDN1, as in the case of hypoxia added to nutrient deprivation, βTC4 cells rescue their invasion capability, being significantly more invasive than only hypoxia treated cells where there is no overexpression of CLDN1.

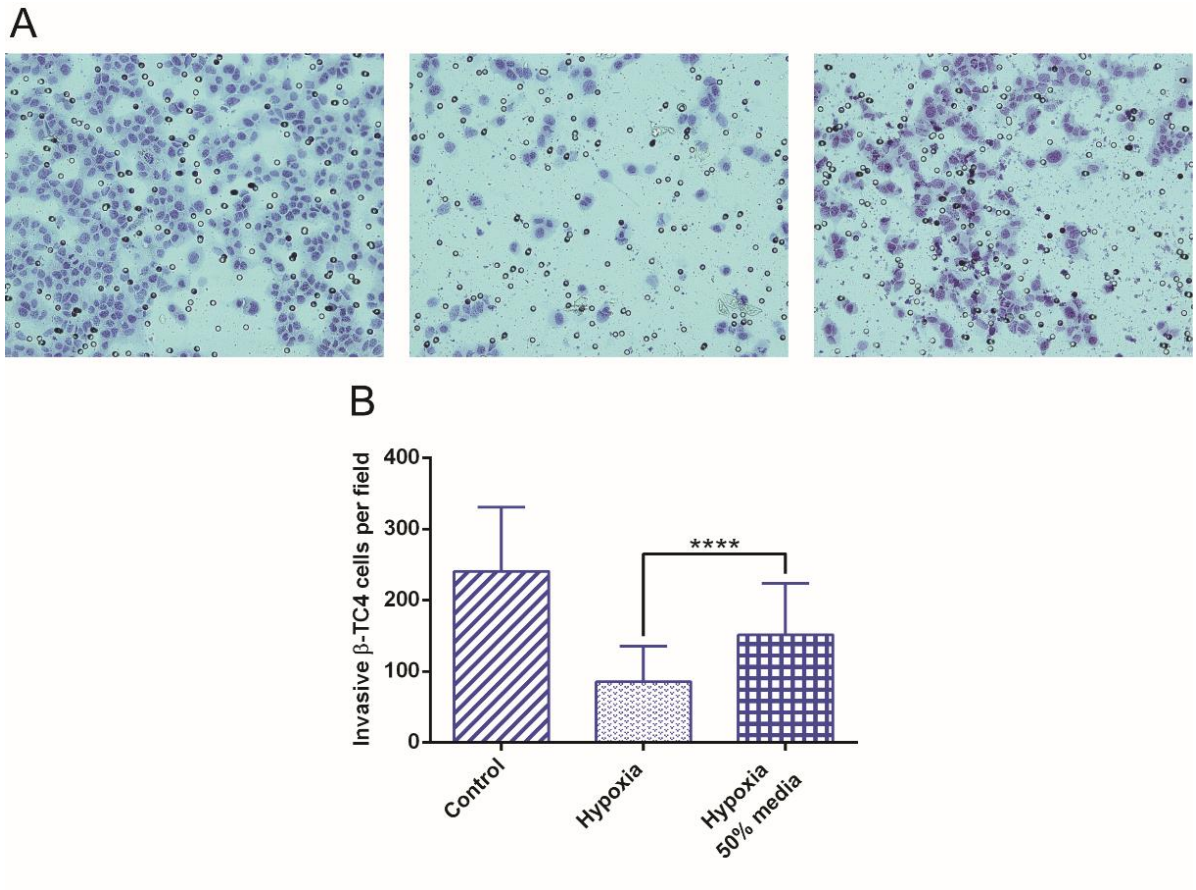

Figure 61. Hypoxia and lack of nutrients drove CLDN1 upregulation and promoted an increase invasion capacity in βTC4 cells after treatment. 500.000 cells were plated onto each well and the assay was performed at 48h. Error bars represent S.D, wells/condition n=3. **(A)** Representative images of hematoxylin staining from βTC4 cells in membrane by Transwell® system. **(B)** βTC4 cells in hypoxia 10% plus nutrient deprivation showed higher invasive capacity than βTC4 cells only hypoxia 10%. Difference statically significant (p< 0,0001) by Mann-Whitney test.

To summarize, βTC4 cells in conditions that mimic anti-angiogenic treatment demonstrated a functional direct relation between CLDN1 expression and βTC4 cells invasion process.

4.2 CLDN1 *in vitro* inhibition

4.2.1 Effects of CLDN1 inhibition of βTC4 cells in 2D model

Once known the ability of βTC4 cells to respond to the anti-angiogenic treatment effects *in vitro*, the YM201636 inhibitor was used to determine the *in vitro* consequences of CLDN1 inhibition.

YM201636 is a small molecule inhibitor of PIKfyve. The enzyme PIKfyve is a lipid kinase (240kDa) responsible to phosphorylates the D-5 position in endosomal phosphatidylinositol-3-phosphate (PI3P) to yield the 3,5-bisphosphate (PI(3,5)P2). This kinase binds to PI(3)P via its FYVE domain. PIKfyve is critical for maintaining the proper morphology of the endosome/lysosome. Thus, this enzyme has been implicated in processes as autophagy and endosome to trans-Golgi network trafficking (Cai et al. 2013). Pikfyve inhibition by YM201636 consequently blocks constant recycling of CLDN1, which decrease its level in membrane and accumulates intracellularly. Even that, YM201636 inhibited also CLDN2 for being recycled in a similar way to CLDN1, the localization of others epithelial markers as ZO-1, occludin and CDH1 appear unchanged (Dukes, Whitley, and Chalmers 2012).

First, we verified phenotype and viability changes of βTC4 cells under YM201636 treatment. Phenotypically, these βTC4 cells remain unchanged after YM201636 treatment (**Figure 62A**), this conclusion can be best observed in greater resolution in **Figure 62B-C**. As to cell viability, visually we did not observe differences between control and YM201636 treated cells, this viability maintenance was confirmed and quantified by trypan blue staining (**Figure 62F-D**).

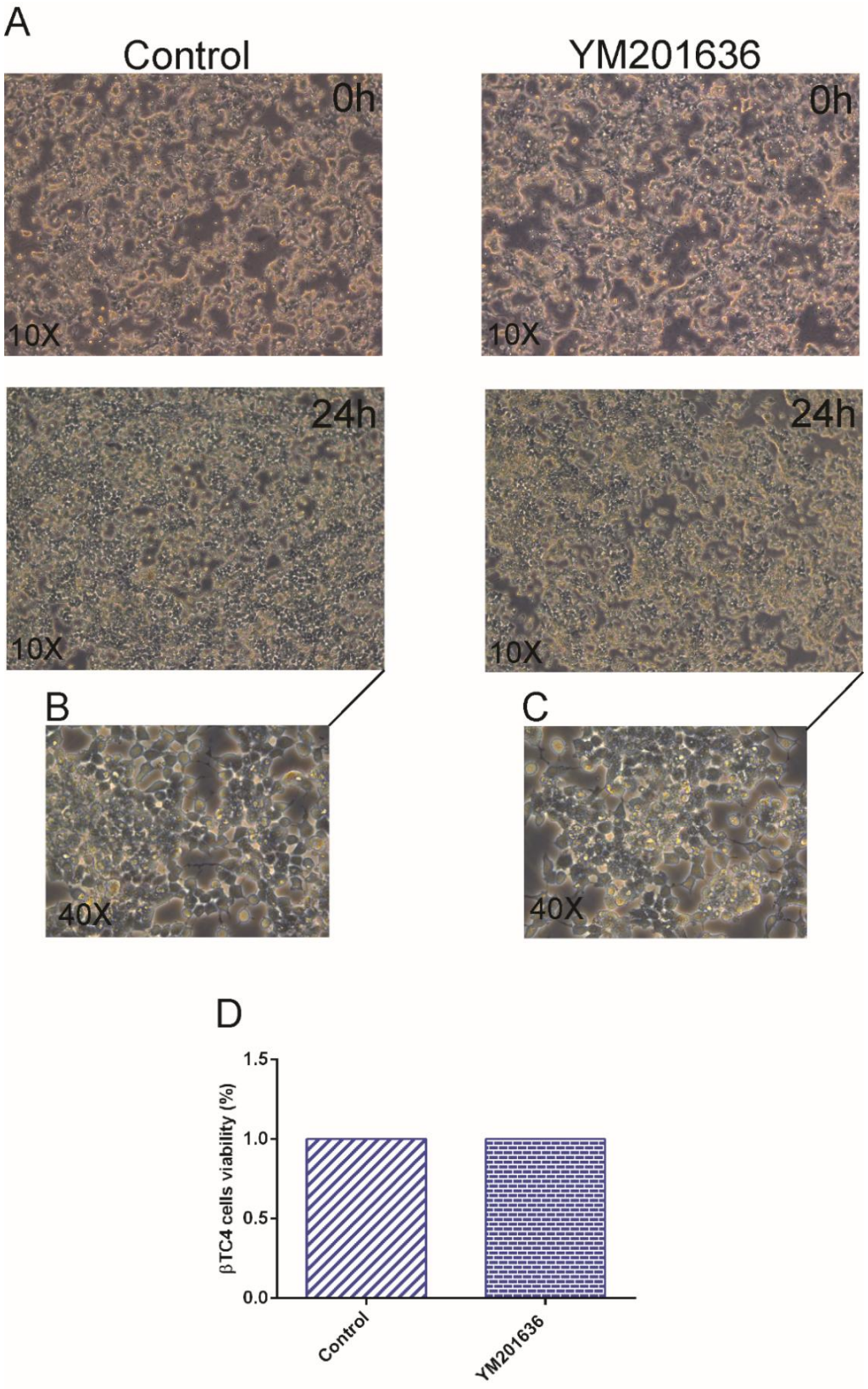

Figure 62. YM201636 treatment did not change the cell phenotype and viability. βTC4 cells were plated and treated with YM201636 (400nM) for 24 hours. **(A)** Pictures at 10X. **(B-C)** Pictures at 40X. **(D)** Percentage of cell viability by trypan blue staining.

To assess CLDN1 inhibition functional effects, YM201636 inhibitor was added to βTC4 media and invasive capacity of cells was measure by Transwell® invasion assay. In detail βTC4 *high* cells (5.0 x 10^5 cells/mL) in βTC4 DMEM medium (5% of FBS) were placed in inserts of the Transwell®. At the same time, the inhibitory effect was studied by adding 400nM of CLDN1 inhibitor (YM201636), to the upper compartment of the Transwell® (**Figure 63**). At the bottom of the well βTC4 DMEM medium (15% of FBS) was placed. Cells were maintained in normoxia at 21% O_2, 5% CO_2, 37°C for 24 hours.

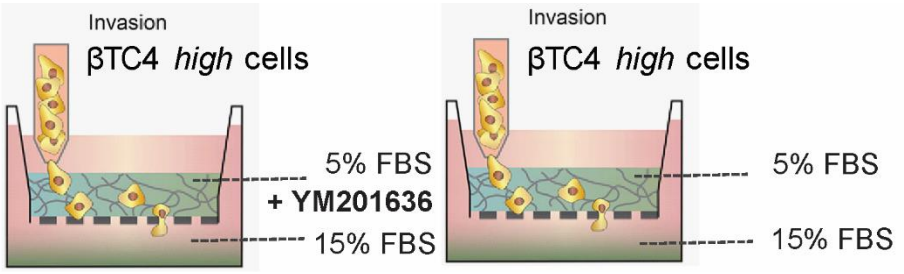

Figure 63. Experimental design of Transwell® invasion assay to assess invasion capacity effect by CLDN1 inhibition using YM201636.

βTC4 cells responded to YM201636 inhibitor stimulation *in vitro* by decreasing their invasion to almost 40% (**Figure 64**).

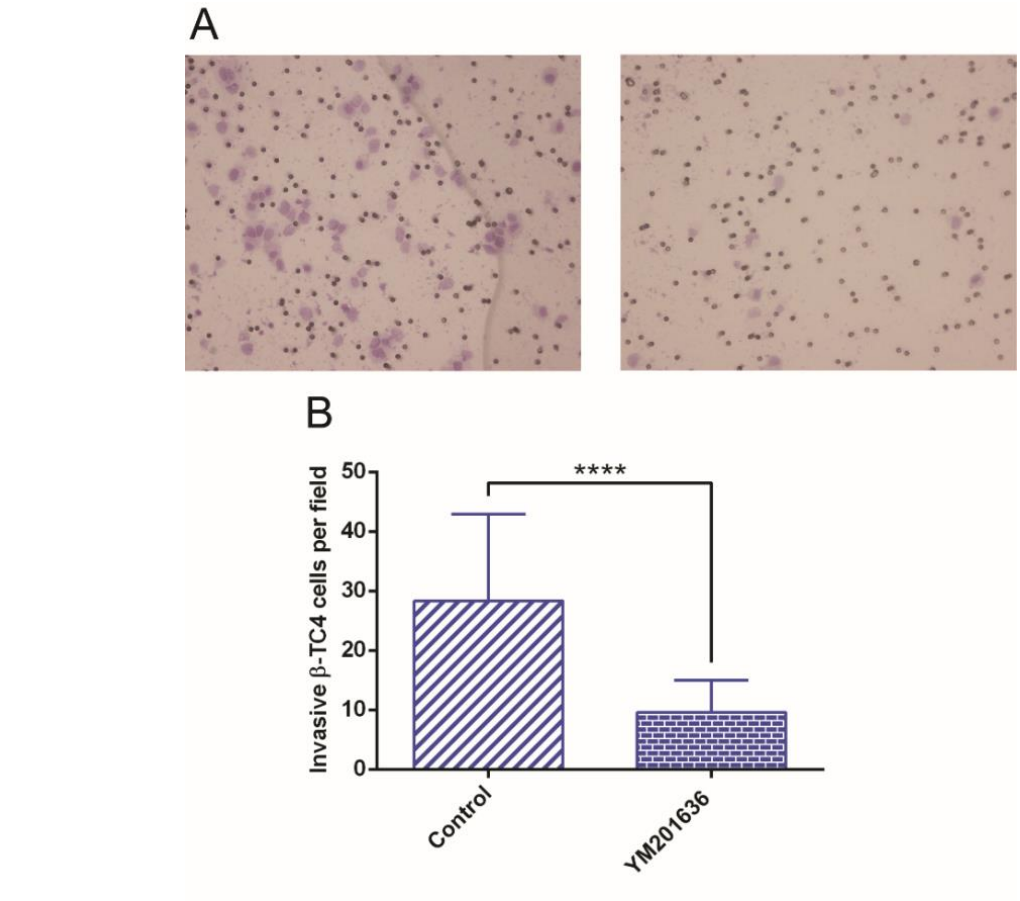

Figure 64. CLDN1 inhibition drastically decreased the invasion abilities of βTC4 cells. (A) Representative images (20X) of Transwell® membranes hematoxylin stained from cells treated with vehicle and YM201636. **(B)** Quantification of invading cells through Transwell® Matrigel®® membranes in 24 hours. Difference statically significant (p< 0,0001) by Mann-Whitney test. Error bars represent S.D, wells/condition n=3.

Taking into account the microenvironment closest to what occurs in the tumor *in vivo* and to confirm this invasion as collective invasive, we decided to verify CLDN1 inhibition by YM201636 treatment in 3D model of βTC4 spheroids submerged in Matrigel®.

In 3D model, results confirmed a drastic decrease of βTC4 spheroid invasion capacity when inhibiting CLDN1, consistent with the effects observed with its inhibition in βTC4 cells in 2D model. Specifically, the number of strands per spheroid is halved when the spheroids are treated with YM201636, this effect occurs since the first day staying until the third and last day of the treatment (**Figure 65**).

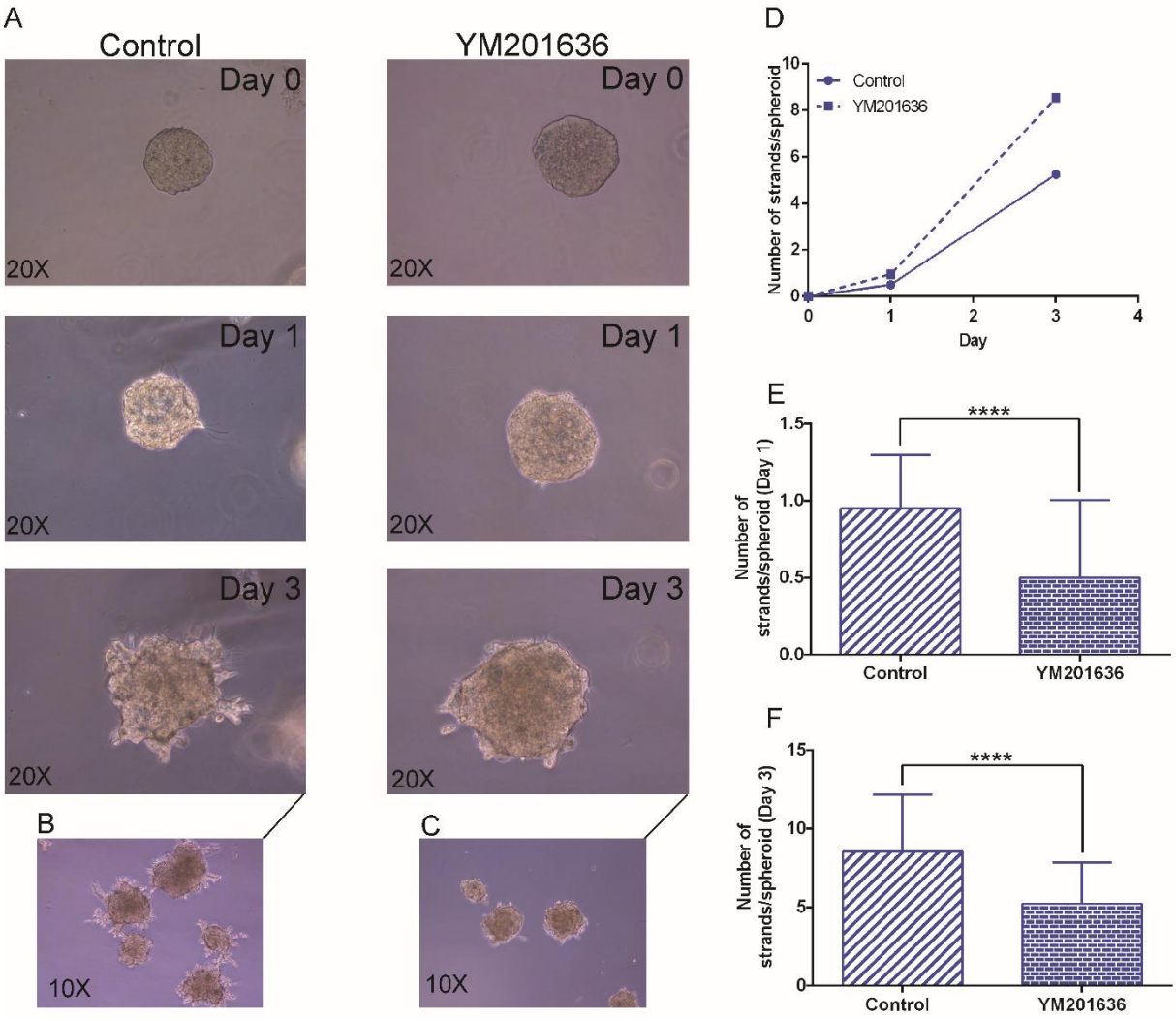

Figure 65. βTC4 spheroids treated with YM201636 responded to CLDN1 inhibition decreasing their invasive capacity. βTC4 spheroids were submerged in 3D Matrigel® structure and treated with YM201636 (400nM) at day 0. **(A)** Pictures of the same spheroid at 20X were taken in 0, 1, 3 day of treatment. **(B-C)** Global final differences observed in pictures of different spheroids at day 3 were performed at 10X objective. **(D)** Number of strands per spheroids for all the days of the assay. **(E-F)** Strands capable to invade the Matrigel® from vehicle conditions (n=83) and YM201636 treated (n=92) were quantified per spheroid at day 1 **(E)** and day 3 **(F)**. Difference statically significant (p< 0,0001) by Mann-Whitney test. Error bars represent S.D.

Altogether, results from these functional assays, demonstrated that CLDN1 inhibition clearly caused decreased βTC4 cells and spheroid invasion while CLDN1 induction via anti-angiogenic effects promoted increased βTC4 cells

invasion. These results support our hypothesis that barrier claudin, CLDN1, is one of the most factors responsible for collective invasion in PanNETs.

Therefore, our data demonstrated both *in vitro* functional implications and *in vivo* an association of the claudin family in establishing the malignization process before and after the anti-angiogenic treatment in RIP1-Tag2 PNET mouse model.

5. Clinical relevance in PanNETs patients

Overall, our results have demonstrated both *in vitro* and *in vivo* association between barrier-claudins, specifically CLDN1/4, and tumor malignization. In order to move these results to clinical setting we performed an analysis of an independent gene expression study of a set of mRNA transcriptomes of PanNET patients from the public database Gene Expression Omnibus (GEO) reference GSE73338 (Missiaglia et al. 2009).

Patient dataset analysed comprised 90 samples of a PanNET study containing normal pancreas, normal pancreas islets, primary non-functional tumors, primary functional tumors (insulinomas), and metastases from non-functional primary tumors (**Figure 66**; graphic on top). To correlate these data according tumor malignization steps, clinical data from PanNETs was grouped in three progression stages, primary non-malignant tumors, primary malignant tumors and metastasis.

In total the analysis was performed using 63 non-functional primary tumors, in which 31 had synchronic metastasis and were determined as malignant primary tumors. In this group of 31 patients, 7 samples were from liver or lymph node metastases. Finally, the 26 non-functional primary tumor patients did not have metastasis were classified as non-malignant primary tumors (**Figure 66**; graphic below) (Missiaglia et al. 2009; Sadanandam et al. 2015).

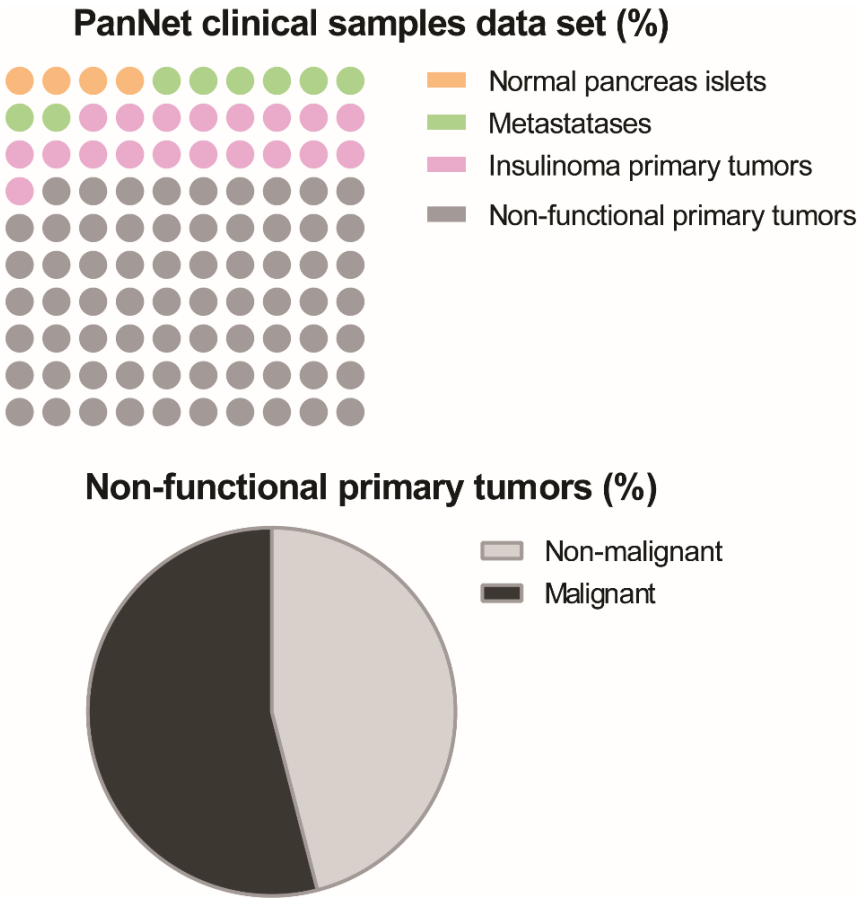

Figure 66. PanNET patient samples dataset description. Graphical description of the GSE73338. PanNET patient dataset as described in Missiaglia *et al.*, 2009 . Clinical dataset is comprise by 97 total samples, being 4 normal pancreas islet (4%) (used as control tissue), 7 metastases (8%), 62 insulinoma primary tumors (69%) and 19 non-functional tumors analysis (19%) (further divided into 26 non-malignant and 31 malignant samples).

5.1 EMT-related genes in patient samples

To better extrapolate the data obtained in RIP1-Tag2 mice, we chose to select only data from primary non-functional tumors. These tumors are often classified according to the WHO as high-grade tumors. High grade tumors are characterized as more aggressive and proliferative tumors, which happen to be more similar to RIP1-Tag2 invasive mice tumors. However primary non-functional tumors do not secrete insulin as RIP1-Tag2 mice tumors do.

To understand to what extent this correlation observed can be traced to tumor malignancy, we performed a detailed analysis relating our tumor invasion

markers with different stages of tumor malignancy. Then, clinical data from PanNETs were grouped in three progression stages, primary non-malignant tumors, primary malignant tumors and metastasis. In total, the analysis was performed using 57 non-functional primary tumors, in which 31 had synchronic metastasis and were determined as malignant primary tumors. In this group of 31 patients, 7 samples were from liver or lymph node metastases. Finally, the 26 non-functional primary tumor patients did not have metastasis were classified as non-malignant primary tumors.

Taking in account our previous results, in which we did not found EMT expression patterns *in vitro* and *in vivo* samples, we decided to confirm these findings in PanNETs clinical data. To this aim, EMT related genes in pancreatic cancer (Beuran et al. 2015) were individually analysed in non-malignant primary tumors, malignant primary tumors.

RNA levels from genes described as attenuated and acquired during in EMT process as Fibronectin (Fn1), Integrin Subunit Alpha 5 (Itga5), Syndecan 1(Sdc1), Zinc Finger E-Box Binding 2 (Zeb2), Snail Transcriptional Repressor 1(Snai1) and Transforming Growth Factor Beta 1 (Tgfb1) were verified in the three stages of tumor progression.

In this analysis, we not found any clear expression changes in these EMT markers in non-malignant primary tumor, malignant primary tumor and metastasis. In addition, *Cdh1* downregulation considered determinant as mesenchymal phenotype marker in our data was not observed. Unlike this, *Cdh1* was found upregulated in metastasis in relation to malignant primary tumor (**Figure 67**).

Thus, these consistently clinical results demonstrated that the mesenchymal phenotype is not the main mechanism that promote PanNETs tumors malignancy in patients, instead of this, is collective invasion that seems has this role.

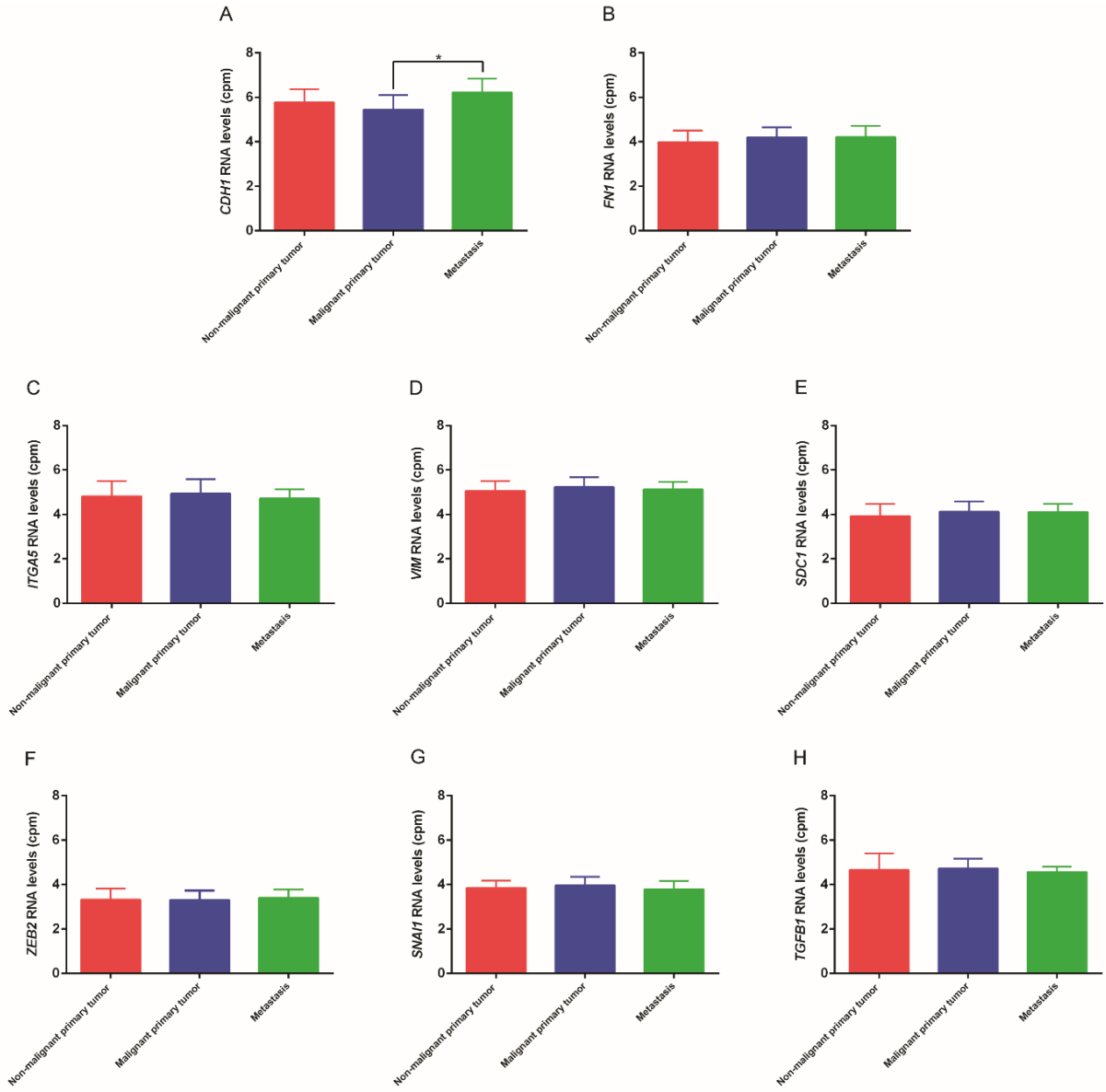

Figure 67. Clinical samples did not show differences in expression levels in the most of EMT related genes during tumor progression. (A-H) RNA levels from EMT related genes in patients samples of non-malignant tumors (n=26), primary malignant tumors (n=31) and metastasis (n=7) were compared. **(A)** Differences were statistically significant as to *CDH1* levels by Mann-Whitney test, being p=0.0561 in malignant tumors primary versus metastases. Error bars represent S.D

5.2 Expression of barrier-forming claudins in clinical samples

Finally, seeking to understand a claudin family role in PanNETs patient samples, were compared all barrier and pore forming claudin RNA levels in clinical samples independently of malignancy. We confirmed higher levels of barrier-

forming claudins than pore-forming claudins in PanNETs tumors from patients (**Figure 68**).

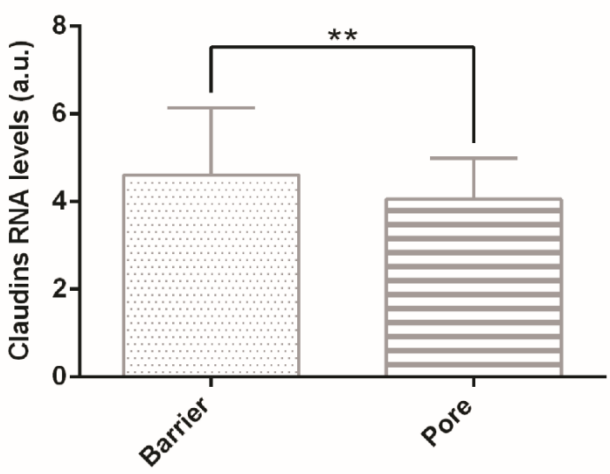

Figure 68. PanNETs patient samples showed higher levels of barrier-forming claudins in comparison to pore-forming claudins. RNA average expression from barrier-forming claudins (*CLDN1, CLDN3, CLDN4, CLDN5, CLDN11, CLDN14, CLDN18*) is higher than pore-forming (*CLDN2, CLDN10, CLDN15, CLDN17*) in primary non-malignant tumors and primary malignant tumors (p=0.0014). Error bars represent S.D. Difference statically significant by Mann-Whitney test.

As well as, malignant tumors increase a barrier-forming claudins expression in comparison to non-malignant tumors (**Figure 69A**). In addition, the barrier claudins difference values between malignant and non-malignant tumors demonstrated that *CLDN1* and *CLDN4* are among the three barrier claudins most differentially expressed in malignant tumors (**Figure 69B**).

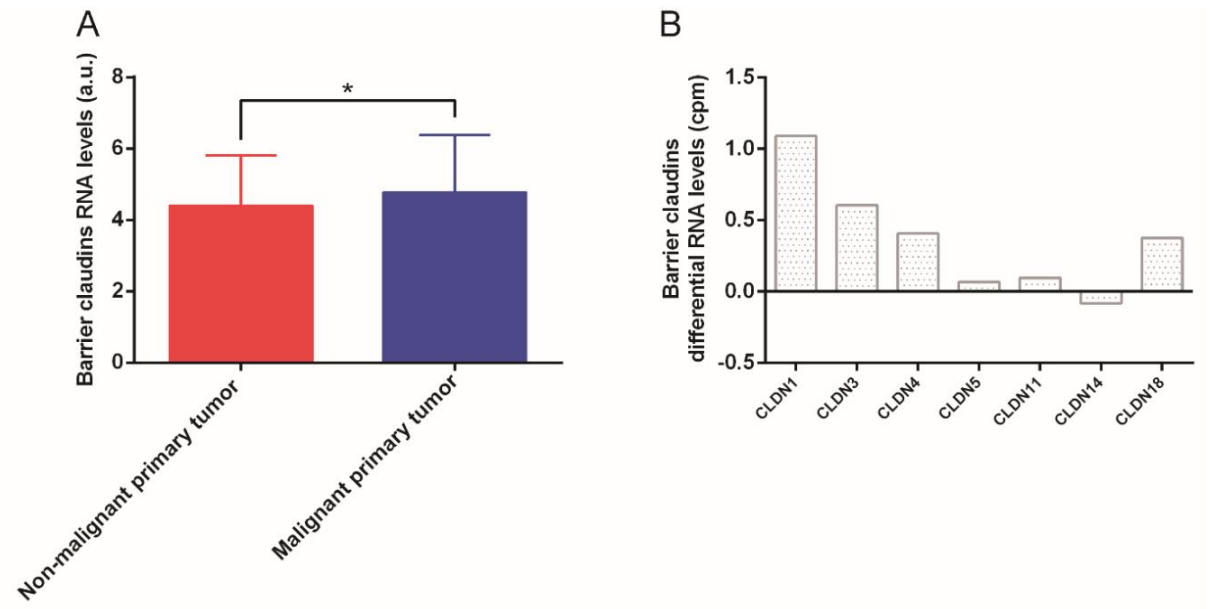

Figure 69. Primary malignant tumors from clinical samples did show high expression of barrier-forming claudins. **(A)** RNA average expression from barrier-forming claudins *(CLDN1, CLDN3, CLDN4, CLDN5, CLDN11, CLDN14, CLDN18*) in primary malignant tumors versus primary non-malignant tumors). Primary malignant tumors increase a barrier-forming claudin levels in comparison to primary non-malignant tumors (p = 0.0118). Error bars represent S.D. Difference statically significant by Mann-Whitney test. **(B)** *CLDN1* showed a higher difference between primary malignant tumors and primary non-malignant tumors in terms of RNA levels.

As we can see in Figure 49A, during the tumor malignancy, the *CLDN4* up-regulate tendency was reported in untreated patients (**Figure 70A**). However, these results were not completely conclusive, due the differences found were not significant. In the other hand, the up-regulation of *CLDN1* was positive during tumor malignancy steps in PanNETs clinical data. As soon, was verified an increase *CLDN1* expression in primary malignant tumors and metastasis in relation to primary non-malignant tumors (**Figure 70B**), thus, hinting a role for this protein as a tumor progression driver. Therefore, the clinical results demonstrated that our candidates seem might be acting together to maintain the collective invasion and, consequently, the tumor malignancy in PanNETs.

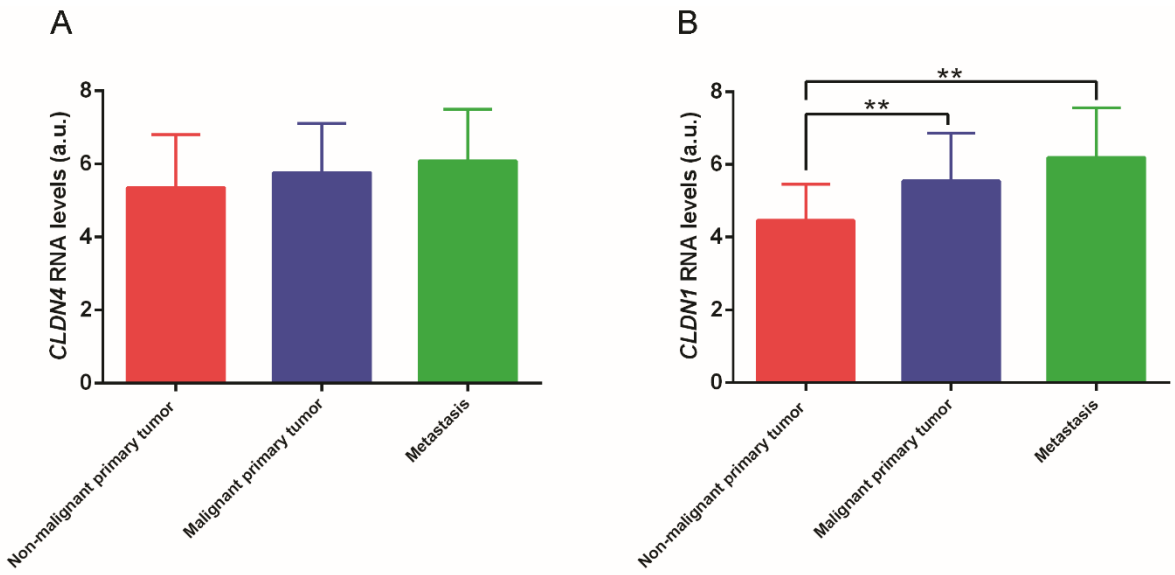

Figure 70. Different steps of tumor malignancy in patients were associated with an increase of claudin1/4 RNA expression levels in clinical samples. PanNETs were grouped according to tumor malignancy steps. **(A)** *CLDN4* RNA levels from patients samples of non-malignant tumors (n=26), primary malignant tumors (n=31) and metastasis (n=7). Error bars represent S.D. **(B)** *CLDN1* RNA levels from patients samples of non-malignant tumors (n=26), primary malignant tumors (n=31) and metastasis (n=7). Differences were statistically significant by Mann-Whitney test, being p=0.0010 in non-malignant tumors primary versus malignant tumors and p=0.0047 in non-malignant tumors primary versus metastasis.

The gradual increases of *CLDN4* and *CLDN1* correlating with malignization, thus, suggesting the importance of these barrier-claudins to maintain the collective invasive Behaviour in PanNETs. Therefore, these molecules might be applied in the future as a prognostic biomarker to PanNETs tumor malignancy, as well as, a potential target to intervene in collective invasion capacity in different kind of tumors.

DISCUSSION

Initially, angiogenesis inhibitors used for cancer treatment seemed to have many advantages over established drugs. Being that anti-angiogenic therapies target endothelial cells genetically, it was believed that these drugs would be completely effective and would not present tumor resistance. Over time, it has been realised that, even though endothelial cells are not transformed, this does not assure efficiency and absence of resistance to these drugs. Using the RIP1-Tag2 model, it has been shown that after 4 weeks of treatment with DC101 (anti-VEGFR2 monoclonal antibody), resistance to therapy was induced within the tumor. Thus, after initial efficacy in terms of tumor volume reduction, it was found that DC101 in the long-term induced a reestablishment of the tumor vasculature culminating in tumor regrowth (Casanovas et al. 2005).

Later, in addition to adaptive tumor resistance being verified after VEGF/VEGFR2 inhibition, an increased invasiveness and metastatic capacity in RIP1-Tag2 tumors has also been observed. This invasion was also associated with high intratumoral hypoxia levels (Pàez-ribes et al. 2010). Molecularly, this invasive phenotype was shown to be related to the maintenance of proteins responsible for cell adhesion, seeming to favour a collective cell invasion mode. However, collective invasion in PanNETs has not been previously described, neither their relationship with anti-angiogenic treatment. In this way, the main objective of this thesis was to functionally validate the collective cancer cell movement in PanNETs before and after anti-angiogenic therapies using a translational approach: first in cell/spheroid models '*in vitro*', followed by validation in the RIP1-Tag2 model of tumor invasion, and, finally, to confirm these findings in the clinical setting with samples of PanNETs.

1. Morphological collective invasion characterization

Most carcinomas may invade as cohesive multicellular groups through a process known as "collective invasion". Alternatively, tumor cells can invade individually by two different processes: the protease-, and integrin-dependent "mesenchymal invasion" program or the protease-, integrin-independent "amoeboid invasion" program (Valastyan & Weinberg 2011). Despite the fact that

not all molecular determinants of each migration mode are completely understood, some key parameters have been identified as “checkpoints” to classify a given migration type (Peter Friedl and Wolf 2010). As an example, to confirm morphologically whether RIP1-Tag2 tumors locally invade in a collective manner, we used a methodology recommended by Friedl and colleagues in which he described the use of histological analysis of tumors *in vivo* to determine whether invasive cells are cohesive and maintain their cell-cell unions during invasion. All of these concepts were confirmed both in control tumors and in anti-angiogenic treated tumors. Thus, we concluded that RIP1-Tag2 tumors invade collectively whether treated or untreated with angiogenesis inhibition therapy, however it remained unclear whether this occurred through the same molecules (Peter Friedl et al. 2012).

In addition, collective invasion is determined *in vitro* by a 3D ECM spheroid invasion method, that is, using multicellular aggregates that are seeded into 3D ECM (collagen I, Matrigel® or others) favouring radial invasion of multicellular strands. Strand size and shape and cell–cell adhesion junction immunostaining may determine differences between individual and collective invasion. The vertical penetration depth and the number of invasive strands are used to determine collective invasion capacity per spheroid (Peter Friedl et al. 2012). In order to follow this methodology, we developed spheroids from βTC4 cells of RIP1-Tag2 tumors and seeded them in three-dimensional conditions. As indicated in the literature, we morphologically verified the cluster of cells through DAPI staining, and the number of multicellular strands informed us about the level of invasion. Finally, the immunostaining pattern of CDH1 and CTNNB1 at the 3D level confirmed the maintenance of adhesion proteins in multicellular invasive strands. Importantly, this methodology has several limitations, the most important of which is the difficulty of antibody penetration into the 3D structure of Matrigel®. To answer this question, we extended the permeabilization and primary antibody incubation steps. Thus, the primary antibody incubation was applied for 2 nights, and the permeability solution was applied not only during permeabilization but also during blocking and antibody incubation steps.

To set up the 3D technique and verify different parameters of culture, many 3D invasion assay using spheroids βTC4 were performed. During this step, the existence of two populations of βTC4 spheroids, which differed substantially in terms of invasion capacity, was noted; these two subpopulations were deemed "*high*" and "*low*" βTC4 spheroids. One possible explanation for this event is that the separation of βTC4 spheroids in small plates for their growth at high confluence in *in vitro* culture may have favoured an expansion of certain *high* or *low* phenotype within each group. These two spheroid subpopulations are probably derived from the intratumoral heterogeneity observed in primary tumors. As we know, genomics research has revealed a substantial intratumor molecular heterogeneity that may evolve over the course of disease and exposure to treatment (Yap et al., 2012). Specifically, the tumor heterogeneity observed in NETs represents a very low mutation rate compared to other malignancies, though the engagement of epigenetic changes in driving NET evolution is emerging, mainly in genes that encode for proteins directly involved in chromatin remodelling (Di Domenico et al. 2017). An analysis using the RIP1-Tag2 model and human PanNET revealed that mutations in chromatin remodeling genes were enriched in intermediary and more metastatic tumors (Sadanandam et al. 2015). Based on these data, we suspect that the heterogeneity observed in the two subpopulations of βTC4 spheroids may be of epigenetic origin. However, *high* and *low* subpopulations still need to be better defined and clarified by both approaches, genetically and epigenetically. Thus, in this thesis these subpopulations were used only as a preliminary tool for screening possible collective invasion markers *in vitro.*

2. Molecular collective invasion characterization

Several authors agree that CDH1 is the protein most differentially expressed in cell tumors that invade collectively. The importance of this marker is even higher, given that its down regulation is necessary to characterize a full EMT (Lehembre et al. 2008; Peter Friedl et al. 2012; Mayor and Roberto 2012; Valastyan & Weinberg 2011; Peter Friedl and Mayor 2017). Specifically, via

CDH1, invasive cell clusters maintain their strong and stable cell adhesion, as well as their apicobasal polarity (Peter Friedl and Mayor 2017). Hence, CDH1 is considered a differential signal between collective and individual invasion in most cases.

RIP1-Tag2 tumors express CDH1 at distinct levels and this well-known marker has been confirmed in untreated tumors, with expression correlated to tumoral invasion capacity. However, in tumors after anti-angiogenic treatment this mechanism is not clear. Unexpectedly, aggressive tumors, when treated with sunitinib, did not show a significant increase in CDH1 expression, suggesting that another mechanism may also be involved in the invasive increase after anti-angiogenic treatment. These results corroborate that which has been observed in βTC4 model, that in untreated conditions βTC4 cells and spheroids showed an increase of CDH1 expression, which was correlated with a greater invasion capacity in 2D and 3D models.

Previous evidence suggests that the invasive phenotype of RIP1-Tag2 tumors does not involve a classical EMT. Chun and Hanahan described no detectable expression differences of EMT transcription factors in non-invasive IT and highly invasive IC2. In addition, N-cadherin, one prominent marker of EMT, is not obviously different between IT and IC2 lesions (Chun and Hanahan 2010). On the other hand, Lehembre and colleagues verified that the loss of E-cadherin levels induces upregulated expression of the NCAM gene, increasing integrin-dependent mesenchymal cell migration and invasion (Lehembre et al. 2008).

3. Collective invasion candidates

The claudin family was the most interesting group of genes obtained from the GSEA analysis data, for which RNA levels from untreated versus sunitinib treated RIP1-Tag2 tumors were compared. There are thought to be around 26 human claudins with a physiological role (Günzel and Yu 2013). Some of them were described to be altered in several cancers (Osanai et al. 2017). In RIP1-Tag2 tumors, barrier function claudins were associated with a more invasive phenotype

in treated tumors. Among them, CLDN4 was the most highly expressed gene in sunitinib treated tumors compared to non-treated. In a recent review, data from different sources were grouped according to primary tumor organ of origin and the altered expression of different claudins. In the majority of cancer types CLDN4 was found to be increased, such as breast, esophagus, stomach, large intestine, biliary tract, pancreas, bladder, kidney, prostate and ovary uterine corpus. However, in tumors from breast, stomach, large intestine, liver, bladder and uterine cervix, CLDN4 expression was found to be decreased (Osanai et al. 2017).

A strong increase of CLDN4 expression was found after sunitinib and DC101 treatment, and this overexpression was also associated with a higher invasiveness in sunitinib treated samples. All of our findings led us to suggest that an increase in the barrier of cell-cell adhesions formed by CLDN4 might represent a crucial factor in contributing to local invasion. Furthermore, contrastingly from the CDH1 results, the differential CLDN4 expression between control and treated tumors was highly significant, showing that the collective invasion observed before and after anti-angiogenic treatment seems to be driven by the same molecules.

To translate the CLDN4 results to βTC4 cells and spheroids *in vitro*, we used 2D and 3D models. Surprisingly, we observed an absence of CLDN4 at the RNA and protein level in all models analysed, and further, every attempt to induce CLDN4 *in vitro* failed. Many cancer cell lines express CLDN4 *in vitro*, such as SKOV3 (ovarian), MCF-7 (breast), HEC-1A (endometrial) and PANC-1 (pancreas) (Cuevas et al. 2015; Nichols, Ashfaq, and Iacobuzio-Donahue 2004; Michl et al. 2001; Casanovas et al. 2005; Hicks et al. 2016). Thus, the absence of CLDN4 in cell lines certainly is not an overall problem with different cell types. In fact, even though βTC4 cells were derived from the RIP1-Tag2 tumor, we are not aware about the CLDN4 expression level specifically in this tumor. To verify whether the lack of CLDN4 was due to the non-expression of this protein by the tumor of origin, or whether there was loss of expression when these tumors were passed to the *in vitro* system, we compared different primary cells from different RIP1-Tag2 tumors. Nevertheless, once more, we did not find protein levels of CLDN4 in any

of the three βTC primary lines analysed. Indeed, these differences may be observed as a result of a true divergence between *in vitro* culture and the *in vivo* scenario. This phenomenon is similar to that shown in other studies in the literature that demonstrate tumor subtypes which are not fully molecularly represented into cell lines (Goodspeed et al. 2016), such as in lung cells when12 of 30 cancer cell lines were found to have distinct EGFR mutations within the same cultures (Nagai et al., 2005). This effect could be a consequence of biological mechanisms of heterogeneity within primary tumors, which may be operational in cell line models (Goodspeed et al. 2016).

On the other hand, gene expression differences between primary xenografts of human small–cell lung cancer, cell lines derived from these tumors and secondary xenograft tumors from these cells have been investigated. As a result, gene expression differences between primary xenografts and monolayer culturing of the cell lines were identified, indicating genomic alterations between the two model systems. In the secondary xenograft, these genes remained differentially expressed, indicating that stable changes had occurred in *in vitro* culture (Daniel et al. 2009).

In vivo cells primarily exist embedded within a complex and information-rich environment that contains multiple ECM components, mixed cell populations that interact heterotypically and a medley of cell-secreted factors. Many cell types, when isolated from tissues and placed into cell culture, become progressively flatter, divide aberrantly and lose part of their phenotype. Interestingly, some of these cell types may regain their physiological form and function when embedded in a three-dimensional (3D) *in vitro* culture environment (Baker and Chen 2012; Riffle and Hegde 2017; Goodspeed et al. 2016). Since our 3D model could not regain CLDN4 expression and among four βTC cell lines analysed, none of them showed CLDN4 protein levels, a potential explanation for this observed phenomenon is that a switch between *in vitro* and *in vivo* models occurs among claudins. Under this hypothesis, another claudin family component would play the role of CLDN4 in βTC4 cells.

Through screening of barrier-forming claudins in βTC4 cells, the current study demonstrated an association between CLDN1 and invasion capacity in *high* βTC4 cells. Briefly, a molecular switch between barrier CLDN1/4 in our *in vivo* and *in vitro* model has been described, in which both claudins are more expressed in accordance with the greater tumor invasiveness capacity. Importantly, CLDN1 acts only in the βTC4 *in vitro* model and CLDN4 only in the RIP-Tag2 *in vivo* model. Several reports have shown that CLDN4 and CLDN1 expression tends to either coincide, or not, in different tumor types such as breast, colorectal and gastric tumors (Hahn-Strömberg et al. 2017; Kwon 2013). However, the deeper relationship between these two proteins is still not well understood. Taking into account that both CLDN1/4 increase transepithelial resistance and, that, overexpression of these claudins affects the same sealing function in distinct models, the key point here is not a specific member of the claudins but the barrier function as a whole.

In order to discuss the association of CLDN1/4 in PanNETs patient samples, we performed a correlation analysis between CLDN1/4 and their adapter proteins based on RNA levels. Patient samples showed a significant correlation between *CLDN1* and *CLDN4* with *TPJ2* (ZO2) protein (**Figure 71A-B**). Furthermore, *CLDN4* and *CLDN1* demonstrated a high correlated expression, thus, when one of the two proteins was more expressed the other protein followed the same pattern (**Figure 71C**). This information further corroborates barrier function from claudins as a relevant factor in this context, independently if whether through *CLDN1* or *CLDN4* proteins or the two proteins at the same time.

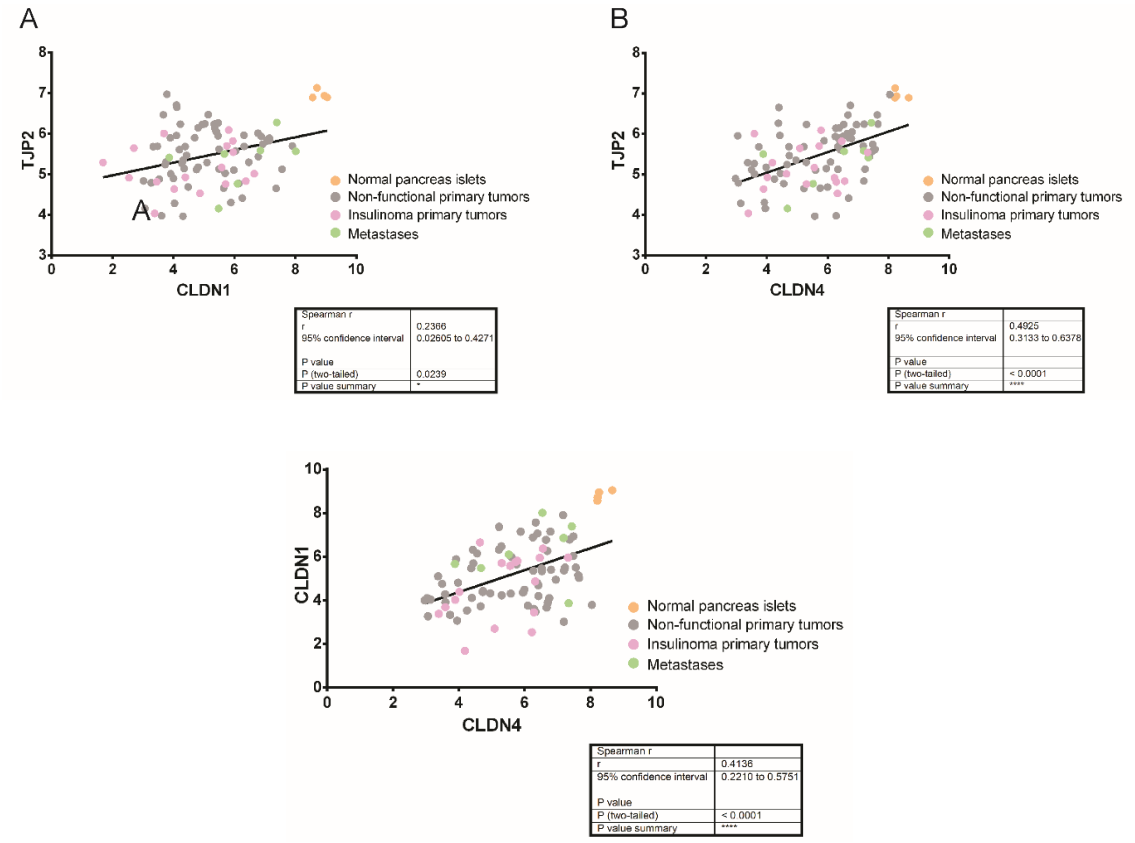

Figure 71. GEO data base demonstrated a correlation between CLDN1/4 and ZO2 in patients. Patient RNA level groups analysed were: normal pancreas islet (n=4), non-functional PNET (n=62), insulinoma (n=17) and metastasis (n=7). Spearman correlations were used to assess associations between continuous variables. Significance was determined by P value. **(A)** TPJ2 and CLDN1 correlation; p=0.0239. **(B)** TJP2 and CLDN4 correlation; p<0.0001. **(C)** CLDN1 and CLDN4 correlation; p<0.0001.

As previously discussed in this section, molecular expression alterations can be led by extracellular matrix presence in *in vitro* models, since the three-dimensional environment provides tumor *in vivo* characteristics that are not present in traditional 2D models. In our results, *low* invasive βTC4 cell and spheroids in the 2D model showed irrelevant CLDN1 and CDH1 levels. When in the 3D microenvironment, βTC4 spheroids increase considerably the presence of CLDN1, but not CDH1. These findings suggest that *low* βTC4 spheroids, with almost no CDH1 protein level, probably are able to invade collectively by the recruitment of CLDN1. Despite *low* levels, *low* βTC4 spheroids show a 1.5 strands per spheroid average. This rate represents significant invasion level considering

the difficulty entailed in collective invasion through Matrigel® or in more complex 3D environments.

4. CLDN1 *in vitro* modulation

The increase of hypoxic level in hyperinvasive tumors and metastatic lesions in the RIP1-Tag2 mouse model treated with anti-VEGFR2 and sunitinib have been well documented (Pàez-ribes et al. 2010). In this way, with a goal to translate *in vivo* molecular CLDN modulation to *in vitro* models, we used 10% hypoxia in combination with a lack of nutrients to mimic the anti-angiogenic therapy. We were able to verify increased CLDN1 protein level after the treatment, and consequently increased invasive capacity of βTC4 cells and spheroids. However, when we applied this methodology to verify this effect for the CLDN4 molecule, as expected, we did not report any response in relation to CLDN4 expression, which was understandable given that these cells do not express CLDN4 under control conditions.

Following our objective, we continued investigating possible manners of modulating CLDN1 functions. Internalization of TJ proteins from the plasma membrane is a crucial mechanism of regulating TJ plasticity and function in both epithelial and endothelial barrier tissues. When internalized, TJ proteins enter complex vesicular machinery, where further trafficking is directly dependent on the downstream signaling pathways that regulate the sorting and destiny of TJ proteins, as well as on cell and barrier responses (Stamatovic et al. 2017). There is distinct internalization among individual tight junction proteins; CLDN1 specifically is constantly endocytosed and recycled back to the plasma membrane in a range of epithelial cell lines (Gehne et al. 2017).

Recent studies show that the constitutive recycling of CLDN1 is dependent upon Endosomal Sorting Complex Required for Transport (ESCRT) (Cai et al. 2013). In this membrane trafficking protein, sorting of some proteins through cargo selection into mutivesicular bodies (MVB) is required (Jin, Lang, and Weisman 2016). For protein sorting to be effective, PI(3,5)P2 action is necessary, which, in

turn, is a product of PI(3)P phosphorylation by the PIKfyve enzyme (Cai et al. 2013). Thus, PIKfyve inhibition treatment causes non-conversion of PI(3)P into PI(3,5)P2, stopping the separation of proteins into mutivesicular bodies and preventing the ESCRT machinery from recycling CLDN1, and as a consequence, accumulating this protein intracellularly into vesicles.

Dukes and colleagues demonstrated that PIKfyve inhibitor (YM201636) treatment is able to inhibit the endocytic CLDN1, providing intracellular accumulation and blocking its function in the membrane (Dukes, Whitley, and Chalmers 2012). Our *in vitro* data using 2D and 3D models showed that YM201636 inhibits tumor invasion by 3D invasion and Transwell®® assay without affecting cellular phenotype and viability, suggesting a functional role of CLDN1 in βTC4 collective invasion. Corroborating our findings, several tumor types have demonstrated CLDN1 upregulation in invasive tumors, such as human samples from endometrial cancer and oral squamous carcinoma cells (Babkair et al. 2016; Shimada et al. 2017). Specifically, was related the increased collective migration and invasion by CLDN1 overexpression during collective movement in epithelial cells (Fortier, Asselin, and Cadrin 2013). Although there is some suspicion in relation to CLDN1 function and its effect in collective invasion, this is the first time that these results are described in PanNETs tumors.

Since PIKfyve enzyme has also been linked to insulin-stimulated translocation of the glucose transporter GLUT4, replication of salmonella and regulation of glutamate transporters, other proteins could be affected besides CLDN1 during PIKfyve inhibition by YM201636 (Dukes, Whitley, and Chalmers 2012). A future experiment that will provide clarity with regards to this inhibitor and will confirm the role of CLDN1 in collective invasion, will be the genetic silencing of CLDN1 through shRNA. For this, we will transfect TRC Lentiviral Mouse Cldn1 shRNA system (Dharmacon®) in *high* βTC4 cells. Next, we will use *high* βTC4 cells transitorily transfected with the shRNA to verify the invasion pattern after CLDN1 genetic silencing in our 2D and 3D models *in vitro*. In addition, it would be interesting to use these cells to perform an *in vivo* study. In this way, shCLDN1

cells and shNS cells would be injected into the subcutaneous or renal capsule of athymic nude mice, where tumor cells would grow and generate a palpable tumor. To study the impact of CLDN1 genetic silencing after anti-angiogenic resistance, mice would first receive DC101 therapy. Animals would be sacrificed after 4 weeks of treatment and the tumor tissue would be analysed for invasion capacity and histology and, finally, molecular CLDN1 silencing would be confirmed.

5. Clinical samples validation

In order to translate from the preclinical RIP1-Tag2 model and BTC4 spheroids to human PanNET patients, a clinical data set of PanNET patient samples was used. These data were selected specifically for analysis, as described in Results (section 5.1), due to high molecular and phenotypical resemblance between non-functional primary tumors and RIP1-Tag2 invasive tumors. In addition, to evaluate our collective invasion candidates in clinical data, the selected samples from PanNETs were grouped in three progression stages, primary non-malignant tumors, primary malignant tumors and metastasis (Sadanandam et al. 2015).

Recently the research value of RIP1-Tag2 tumors for its cognate human cancer was evaluated, using a genomic comparison of tumors from both human and mice samples. For this, RIP1-Tag2 tumors were separated into two distinct subtypes: well-differentiated IT and poorly differentiated tumors associated with liver metastasis (MLP). Human PanNETs were independently split into these same two subtypes. As a result, MLP subtypes in human and mouse were similar to liver metastases, taking into account their transcriptome profiles and signature genes, coinciding with a non-functional signature. Therefore, this evaluation confirmed that the molecular mechanisms of PanNET tumors might be studied using the RIP1-Tag2 model as a surrogate for both human functional and non-functional tumors (Sadanandam et al. 2015). On the other hand, there is also evidence for genetic and phenotypic heterogeneity in RIP1-Tag2 tumors, since a range of chromosomal aberrations have been observed (Hodgson et al. 2001).

Our results demonstrated that among barrier claudins the three most differentially expressed in malignant primary tumors in relation to non-malignant primary tumors were *CLDN1*, *CLDN3* and *CLDN4*. Surprisingly, *CLDN1* and *CLDN4* are our collective candidates from preclinical studies, and in patient data they were also found to be highly expressed in malignant tumors in comparison to non-malignant tumors. Ultimately, we verified a significant up-regulation of *CLDN1* in accordance with the higher level of tumor malignancy in PanNETs clinical data. However, despite the tendency of *CLDN4* to increase levels in more malignant lesions, these results were not significant. Thus, PanNET tumor results also suggest that barrier claudins perform a crucial role in collective invasion, involving specific claudin members *CLDN1* or *CLDN4*, depending the context, but it is the barrier function as a whole that seems to be key in this process. Even though more comprehensive studies are surely necessary, our results suggest that barrier claudins, and specifically CLDN1 and CLDN4 in PanNETs, could in future be a useful prognostic biomarker for patients, and a possible second-line target to avoid tumor invasion after treatment resistance.

6. Clinical relevance and future treatments

As mentioned before, in most types of cancer CLDN4 is found to be increased, for example in breast, esophagus, stomach, large intestine, biliary tract, pancreas, bladder, kidney, prostate and ovary uterine corpus. On the other hand, in tumors from breast, stomach, large intestine, liver, bladder and uterine cervix, CLDN4 expression is found to be decreased (Osanai et al. 2017).

Taking into account this group of tumors, the closest to PanNETs are pancreatic tumors. In patient pancreatic samples, strong CLDN4 expression was apparent in 99% of primary pancreatic ductal adenocarcinomas, and in 100% of metastatic pancreatic ductal adenocarcinomas in comparison to only 19% of normal pancreatic duct epithelium (Kojima, Kyuno, and Sawada 2012). Our findings in PanNETs are equivalent to those found in pancreatic tumors; we found a strong increase of CLDN4 after sunitinib and DC101 treatment, and this

overexpression was also associated with a higher invasiveness in sunitinib treated samples.

Regarding inhibition of claudins in patients, apilimod is a first-in-class PIKfyve kinase inhibitor, and this drug has demonstrated promising results in B-cell non-Hodgkin lymphoma (B-NHL) and is undergoing a human phase I clinical trial (NCT02594384) estimated to be finalized in December of 2019. PIKfyve kinase was verified as a target for B-NHL and its inhibition by apilimod demonstrated powerful and selective antiproliferative and cytotoxic effects. Nonetheless, even though potent effects of apilimod have been demonstrated, this clinical trial was performed prior to the identification of its direct target, which has been described until now as the role of PIKfyve to control endolysosomal membrane traffic (Gayle et al. 2017).

In this sense, PIKfyve kinase inhibitors could be also indicated in other cancer types such as PanNETs, focusing on CLDN1 inhibition, provided that the findings obtained in this thesis were confirmed in further preclinical studies. In any case, the results of these clinical trials will enlighten as to the safety and tolerability of PIKfyve inhibitors, helping to determine side effects from this therapy regardless of the disease.

7. Claudin binders as a novel strategy to treat cancer

As detailed in the Introduction, claudin structurally has four transmembrane domains, of which two are extracellular loops. The first extracellular loop is the coreceptor required for entry of hepatitis C virus (HCV) and influences the paracellular charge selectivity, and the second extracellular loop is the receptor of Clostridium perfringens enterotoxin (CPE). CPE is the toxin with major virulence of C. perfringens. It has been described that claudin-3, -4, -6, -7, -8, and -14, but not claudin-1, -2, -5, and -10, are sensitive to CPE. A single CPE polypeptide is comprised of 319 amino acids, has a molecular weight of 35kDa and causes food poisoning in humans, in which it binds to its claudin receptor, then causes changes in membrane permeability via a complex formation on the plasma membrane,

followed by the induction of apoptosis (Kojima, Kyuno, and Sawada 2012). Recent data reported CLDN4 as crucial in tumor progression via proliferation, transformation, and metastasis (Liang et al. 2017). Additionally, CLDN4 protein is highly expressed in many kinds of malignant tumors, among them pancreatic, ovarian, gastric and prostate (English and Santin 2013; Liang et al. 2017; Kojima, Kyuno, and Sawada 2012; Romanov et al. 2014).

In gastric cancer the cytotoxic effect of CPE was determined *in vivo* in xenograft mouse models, in which one group was treated with CPE and the other was not. The CPE positive group significantly suppressed tumor growth and had reduced tumor volume in relation to untreated animals. However, these treated animals showed injection site skin necrosis and enteritis as a consequence of the treatment (Liang et al. 2017). Some studies altered the structure of CPE to overcome systemic toxicity. In order to treat prostate cancer selectively with CPE enterotoxin, a modified protoxin was constructed with a flexible linker containing a PSA-specific protease cleavage site. Being that PSA is secreted and active only in prostate cancer cells, the cytotoxicity toward PSA-negative but CLDN4-expressing cells was greatly reduced or eliminated (Romanov et al. 2014).

Therefore, the use of CPE optimized with a focus on target gene therapy is one strategy that might be explored in all tumors that overexpress CLDN4 and other CPE-binding claudins. Given that invasive RIP1-Tag2 tumors were found to be associated with CLDN4 upregulation after the anti-angiogenic treatment, optimized CPE could be a relevant strategy to overcome collective invasion and reduce tumoral malignancy observed after therapy.

Some authors have identified CLDN1 as essential for HCV entry. In detail, residues within the first extracellular loop of CLDN1, but not protein interaction motifs in intracellular domains, are crucial for HCV entry. In the development of antiviral drug antibodies, an antibody directed against an epitope inserted in the first extracellular loop of CLDN1 was able to block HCV infection (Fukasawa et al. 2015). This binding site of CLDN1 has not yet been applied as an approach in the

treatment of cancer but could be interesting to explore in the future to treat several cancer types that show a CLDN1 overexpression pattern (Hashimoto et al. 2017).

Finally, to improve CLDN-targeted based therapies in future, it is crucial to define CLDN binders in detail. This information will be beneficial for developing the next generation of CLDN binders, including chemicals, peptides, and functional antibodies. Thus, determining the complex structures of different CLDNs and anti-CLDN antibodies will help in theoretical in silico drug design for CLDN-targeted drug development. The future of CLDN-targeted therapy seems to be promising, given that several groups are already determining and screening new types of CLDN binders, and clinical trials of anti-CLDN antibodies as antitumor reagents are ongoing (Hashimoto et al. 2017).

Furthermore, the ease of bonding of claudins provided by coreceptors in their extracellular loops is part of a whole promising context that has been described in relation to Claudin binders. In the future, these strategies could be applied in PanNETs tumors, aiming to intervene in tumor progression steps.

Overall, this thesis has shed light on the biology of collective invasion in PanNETs, and though more comprehensive studies are surely required, our results suggest that barrier claudins, and in specific CLDN1 and CLDN4 in PanNETs, could be a useful prognostic biomarker for patients in the future, and a possible second-line target to avoid tumor invasion after antiangiogenic treatment resistance.

CONCLUSIONS

1. Morphologically, the invasion of RIP1-Tag2 tumors is determined by collective cancer cell invasion, in which cancer cells invade in multicellular strands across acinar tissue and remain attached to a large tumor mass.

2. We have successfully set up an *in vitro* three-dimensional tumor model using spheroids from βTC4 cells which mimic collective invasion effects before and after anti-angiogenic treatment.

3. βTC4 spheroids in a three-dimensional model have a collective invasion behaviour, whereby spheroids invade in multicellular strands while maintaining epithelial markers CDH1 and CTNNB1 along their protusions.

4. The invasion mechanism in RIP1-Tag2 untreated tumors is associated with CDH1 function, but in RIP1-Tag2 tumors after anti-angiogenic treatment this relationship is not observed, suggesting that other players are important.

5. CLDN4 protein seems to induce invasiveness before and after anti-angiogenic therapy in RIP1-Tag2 tumors, which is involved in barrier function stability and increased integrity adhesion between cells and is thereby associated with tumor collective invasiveness capacity.

6. CLDN1 functional validations in βTC4 cells and spheroids demonstrated a direct implication of CLDN1 in cancer cell invasion in 2D and 3D models.

7. In PanNETs patients, CLDN1 is strongly associated with tumor progression.

8. This study suggests that barrier-forming claudins, and especially CLDN1, might be suitable tumor progression biomarkers for PanNETs tumors, as well as potential targets to impinge on collective invasion.

REFERENCES

B

Babkair, Hamzah, Manabu Yamazaki, Md Shihab Uddin, Satoshi Maruyama, Tatsuya Abé, Ahmed Essa, Yoshimasa Sumita, et al. 2016. “Aberrant Expression of the Tight Junction Molecules Claudin-1 and Zonula Occludens-1 Mediates Cell Growth and Invasion in Oral Squamous Cell Carcinoma.” *Human Pathology* 57: 51–60.

Baker, Brendon M., and Christopher S. Chen. 2012. “Deconstructing the Third Dimension – How 3D Culture Microenvironments Alter Cellular Cues.” *Journal of Cell Science* 125 (13): 3015–24.

Baumgartner, Heidi K., Michael C. Rudolph, Palaniappian Ramanathan, Valerie Burns, Patricia Webb, Benjamin G. Bitler, Torsten Stein, Ken Kobayashi, and Margaret C. Neville. 2017. “Developmental Expression of Claudins in the Mammary Gland.” *Journal of Mammary Gland Biology and Neoplasia* 22 (2): 141–57.

Beuran, Mircea, Ionut Negoi, Sorin Paun, Adriana Daniela Ion, Coralia Bleotu, Ruxandra Irina Negoi, and Sorin Hostiuc. 2015. “The Epithelial to Mesenchymal Transition in Pancreatic Cancer: A Systematic Review.” *Pancreatology* 15 (3): 217–25.

Bienz, Mariann, and Hans Clevers. 2000. “Linking Colorectal Cancer to Wnt Signaling.” *Cell* 103 (2): 311–20.

Boekhorst, V. te, and P. Friedl. 2016. “Plasticity of Cancer Cell Invasion—Mechanisms and Implications for Therapy.” In *Advances in Cancer Research*, 1st ed., 132:209–64.

C

Cai, Xinming, Yongyao Xu, Atwood K. Cheung, Ronald C. Tomlinson, Abel Alcázar-Román, Leon Murphy, Andreas Billich, et al. 2013. “PIKfyve, a Class III PI Kinase, Is the Target of the Small Molecular IL-12/IL-23 Inhibitor Apilimod and a Player in Toll-like Receptor Signaling.” *Chemistry and Biology* 20 (7): 912–21..

Capozzi, Monica, Claudia Von Aarx, Chiara De Divittis, Alessando Ottaiano, Fabiana Tatangelo, Giovanni Maria Romano, and Salvatore Tafuto. 2016. “Antiangiogenic Therapy in Pancreatic Neuroendocrine Tumors.” *Anticancer Research* 36 (10): 5025–30. https://doi.org/10.21873/anticanres.11071.

Casanovas, Oriol, Daniel J. Hicklin, Gabriele Bergers, and Douglas Hanahan. 2005. “Drug Resistance by Evasion of Antiangiogenic Targeting of VEGF Signaling in Late-Stage Pancreatic Islet Tumors.” *Cancer Cell* 8 (4): 299–309.

Chaffer, Christine L., Beatriz P. San Juan, Elgene Lim, and Robert A. Weinberg. 2016. “EMT, Cell Plasticity and Metastasis.” *Cancer and Metastasis Reviews* 35 (4): 645–54.

Chaffer, Christine, and Robert Weinberg. 2011. “A Perspective on Cancer.” *Science* 331 (6024): 1559–65.

Chanrion, Maia, Inna Kuperstein, Cédric Barrière, Fatima El Marjou, David Cohen, Danijela Vignjevic, Lev Stimmer, et al. 2014. “Concomitant Notch Activation and P53 Deletion Trigger Epithelial-to-Mesenchymal Transition and Metastasis in Mouse Gut.” *Nature Communications* 5 (1): 5005.

Chun, Matthew G. H., and Douglas Hanahan. 2010. “Genetic Deletion of the Desmosomal Component Desmoplakin Promotes Tumor Microinvasion in a Mouse Model of Pancreatic Neuroendocrine Carcinogenesis.” Edited by Bruce E. Clurman. *PLoS Genetics* 6 (9): e1001120.

Clark, Andrew G., and Danijela Matic Vignjevic. 2015. “Modes of Cancer Cell Invasion and the Role of the Microenvironment.” *Current Opinion in Cell Biology* 36: 13–22.

Cuevas, Maria E., Jenna M. Gaska, Andrea C. Gist, Jonathan M. King, Rebecca A. Sheller, and Maria C. Todd. 2015. “Estrogen-Dependent Expression and Subcellular Localization of the Tight Junction Protein Claudin-4 in HEC-1A Endometrial Cancer Cells.” *International Journal of Oncology* 47 (2): 650–56.

D

Daniel, Vincent C, Luigi Marchionni, Jared S Hierman, Jonathan T Rhodes, W. L. Devereux, Charles M Rudin, Rex Yung, et al. 2009. “A Primary Xenograft Model of Small-Cell Lung Cancer Reveals Irreversible Changes in Gene Expression Imposed by Culture In Vitro.” *Cancer Research* 69 (8): 3364–73.

Domenico, Annunziata Di, Tabea Wiedmer, Ilaria Marinoni, and Aurel Perren. 2017. “Genetic and Epigenetic Drivers of Neuroendocrine Tumours (NET).” *Endocrine-Related Cancer* 24 (9): R315–34.

Du, Yi Chieh Nancy, Brian C. Lewis, Douglas Hanahan, and Harold Varmus. 2007. “Assessing Tumor Progression Factors by Somatic Gene Transfer into a Mouse Model: Bcl-XL Promotes Islet Tumor Cell Invasion.” *PLoS Biology* 5 (10): 2255–69.

Dukes, Joseph D., Paul Whitley, and Andrew D. Chalmers. 2012. “The Pikfyve Inhibitor YM201636 Blocks the Continuous Recycling of the Tight Junction Proteins Claudin-1 and Claudin-2 in MDCK Cells.” *PLoS ONE* 7 (3): 1–10.

E

Efrat, Shimon, S. Linde, H. Kofod, David Spector, Michael Delannoy, Seth Grant, Douglas Hanahan, and S. Baekkeskov. 1988. “Beta-Cell Lines Derived from Transgenic Mice Expressing a Hybrid Insulin Gene-Oncogene.” *Proceedings of the National Academy of Sciences* 85 (23): 9037–41.

Ehehalt, Florian, Hans D Saeger, C Max Schmidt, and R Grutzmann. 2009. “Neuroendocrine Tumors of the Pancreas.” *The Oncologist* 14 (5): 456–67.

English, Diana P., and Alessandro D. Santin. 2013. “Claudins Overexpression in Ovarian Cancer: Potential Targets for Clostridium Perfringens Enterotoxin (CPE) Based Diagnosis and Therapy.” *International Journal of Molecular Sciences* 14 (5): 10412–37.

F

Folkman, Judah, Karol Watson, Donald Ingber, and Douglas Hanahan. 1989. “Induction of Angiogenesis during the Transition from Hyperplasia to Neoplasia.” *Nature* 339 (6219):

Fortier, Anne Marie, Eric Asselin, and Monique Cadrin. 2013. “Keratin 8 and 18 Loss in Epithelial Cancer Cells Increases Collective Cell Migration and Cisplatin Sensitivity through Claudin1 Up-Regulation.” *Journal of Biological Chemistry* 288 (16): 11555–71.

Friedl, P, S Borgmann, and E B Bröcker. 2001. “Amoeboid Leukocyte Crawling through Extracellular Matrix: Lessons from the Dictyostelium Paradigm of Cell Movement.” *Journal of Leukocyte Biology* 70 (4): 491–509. https://doi.org/10.1189/JLB.70.4.491.

Friedl, Peter, and Stephanie Alexander. 2011. “Cancer Invasion and the Microenvironment: Plasticity and Reciprocity.” *Cell* 147 (5): 992–1009.

Friedl, Peter, and Darren Gilmour. 2009. “Collective Cell Migration in Morphogenesis, Regeneration and Cancer.” *Nature Reviews Molecular Cell Biology* 10 (7): 445–57.

Friedl, Peter, Joseph Locker, Erik Sahai, and Jeffrey E. Segall. 2012. “Classifying Collective Cancer Cell Invasion.” *Nature Cell Biology* 14 (8): 777–83.

Friedl, Peter, and Roberto Mayor. 2017. “Tuning Collective Cell Migration by Cell-Cell Junction Regulation.” *Cold Spring Harbor Perspectives in Biology* 9 (4).

Friedl, Peter, and Katarina Wolf. 2003. “Tumour-Cell Invasion and Migration: Diversity and Escape Mechanisms.” *Nature Reviews Cancer* 3 (5): 362–74.

Friedl, Peter, and Katarina Wolf. 2010. “Plasticity of Cell Migration: A Multiscale Tuning

Model.” The Journal of Cell Biology 188 (1): 11–19.

Fukasawa, Masayoshi, Shotaro Nagase, Yoshitaka Shirasago, Manami Iida, Mayo Yamashita, Kohki Endo, Kiyohito Yagi, et al. 2015. “Monoclonal Antibodies against Extracellular Domains of Claudin-1 Block Hepatitis C Virus Infection in a Mouse Model.” Edited by J.-H. J. Ou. *Journal of Virology* 89 (9): 4866–79.

G

Ganss, Ruth, Eduard Ryschich, Ernst Klar, Bernd Arnold, and G??nter J. H??mmerling. 2002. “Combination of T-Cell Therapy and Trigger of Inflammation Induces Remodeling of the Vasculature and Tumor Eradication.” *Cancer Research* 62 (5): 1462–70.

Gayle, Sophia, Sean Landrette, Neil Beeharry, Chris Conrad, Marylens Hernandez, Paul Beckett, Shawn M. Ferguson, et al. 2017. “Identification of Apilimod as a First-in-Class PIKfyve Kinase Inhibitor for Treatment of B-Cell Non-Hodgkin Lymphoma.” *Blood* 129 (13): 1768–78.

Gehne, Nora, Agathe Lamik, Martin Lehmann, Reiner F. Haseloff, Anuska V. Andjelkovic, and Ingolf E. Blasig. 2017. “Cross-over Endocytosis of Claudins Is Mediated by Interactions via Their Extracellular Loops.” *PLoS ONE* 12 (8): 1–21.

Giampieri, Silvia, Cerys Manning, Steven Hooper, Louise Jones, Caroline S. Hill, and Erik Sahai. 2009. “Localized and Reversible TGFβ Signalling Switches Breast Cancer Cells from Cohesive to Single Cell Motility.” *Nature Cell Biology* 11 (11): 1287–96.

González-Mariscal, Lorenza, Alaide Domínguez-Calderón, Arturo Raya-Sandino, José Mario Ortega-Olvera, Orlando Vargas-Sierra, and Gabriela Martínez-Revollar. 2014. “Tight Junctions and the Regulation of Gene Expression.” *Seminars in Cell and Developmental Biology* 36: 213–23.

Goodspeed, A., L. M. Heiser, J. W. Gray, and J. C. Costello. 2016. “Tumor-Derived Cell Lines as Molecular Models of Cancer Pharmacogenomics.” *Molecular Cancer Research* 14 (1): 3–13.

Günzel, Dorothee, and Alan S. L. Yu. 2013. “Claudins and the Modulation of Tight Junction Permeability.” *Physiological Reviews* 93 (2): 525–69.

H

Haeger, Anna, Marina Krause, Katarina Wolf, and Peter Friedl. 2014. “Cell Jamming: Collective Invasion of Mesenchymal Tumor Cells Imposed by Tissue Confinement.” *Biochimica et Biophysica Acta - General Subjects* 1840 (8): 2386–95.

Hahn-Strömberg, Victoria, Shlear Askari, Abrar Ahmad, Rahel Befekadu, and Torbjörn K. Nilsson. 2017. “Expression of Claudin 1, Claudin 4, and Claudin 7 in Colorectal Cancer and Its Relation with CLDN DNA Methylation Patterns.” *Tumor Biology* 39 (4): 101042831769756.

Hanahan, Douglas, and Gabriele Bergers. 2008. “Modes of Resistance to Anti-Angiogenic Therapy.” *Nature Reviews Cancer* 8 (8): 592–603.

Hashimoto, Yosuke, Masayoshi Fukasawa, Hiroki Kuniyasu, Kiyohito Yagi, and Masuo Kondoh. 2017. “Claudin-Targeted Drug Development Using Anti-Claudin Monoclonal Antibodies to Treat Hepatitis and Cancer.” *Annals of the New York Academy of Sciences* 1397 (1): 5–16.

Helvert, Sjoerd Van, Cornelis Storm, and Peter Friedl. 2018. “Mechanoreciprocity in Cell Migration.” *Nature Cell Biology* 20 (1): 8–20.

Hicks, Douglas A., Carly E. Galimanis, Patricia G. Webb, Monique A. Spillman, Kian Behbakht, Margaret C. Neville, and Heidi K. Baumgartner. 2016. “Claudin-4 Activity in Ovarian Tumor Cell Apoptosis Resistance and Migration.” *BMC Cancer* 16 (1): 788.

Hodgson, Graeme, Jeffrey H. Hager, Stas Volik, Sujatmi Hariono, Meredith Wernick, Dan Moore, Donna G. Albertson, et al. 2001. “Genome Scanning with Array CGH Delineates Regional Alterations in Mouse Islet Carcinomas.” *Nature Genetics* 29 (4): 459–64.

J

Jin, Natsuko, Michael J Lang, and Lois S Weisman. 2016. “Phosphatidylinositol 3,5-Bisphosphate: Regulation of Cellular Events in Space and Time.” *Biochemical Society Transactions* 44 (1): 177–84.

K

Kelgiorgi, Dionysia, and Christos Dervenis. 2017. “Pancreatic Neuroendocrine Tumors: The Basics, the Gray Zone, and the Target.” *F1000Research* 6 (May): 663.

Kojima, T, D Kyuno, and N Sawada. 2012. “Targeting Claudin-4 in Human Pancreatic Cancer.” *Expert Opin Ther Targets* 16 (9): 881–87.

Krause, G., J. Protze, and J. Piontek. 2015. “Assembly and Function of Claudins: Structure-Function Relationships Based on Homology Models and Crystal Structures.” *Seminars in Cell and Developmental Biology* 42: 3–12.

Krause, Gerd, Lars Winkler, Sebastian L. Mueller, Reiner F. Haseloff, Jörg Piontek, and Ingolf E. Blasig. 2008. “Structure and Function of Claudins.” *Biochimica et Biophysica Acta - Biomembranes* 1778 (3): 631–45.

Kwon, Mi Jeong. 2013. “Emerging Roles of Claudins in Human Cancer.” *International Journal of Molecular Sciences* 14 (9): 18148–80.

L

Lamouille, Samy, Jian Xu, and Rik Derynck. 2014. “Molecular Mechanisms of Epithelial–mesenchymal Transition.” *Nature Reviews Molecular Cell Biology* 15 (3): 178–96.

Lawrence, Ben, Bjorn I. Gustafsson, Anthony Chan, Bernhard Svejda, Mark Kidd, and Irvin M. Modlin. 2011. “The Epidemiology of Gastroenteropancreatic Neuroendocrine Tumors.” *Endocrinology and Metabolism Clinics of North America* 40 (1): 1–18.

Lehembre, Francois, Mahmut Yilmaz, Andreas Wicki, Tibor Schomber, Karin Strittmatter, Dominik Ziegler, Angelika Kren, et al. 2008. “NCAM-Induced Focal Adhesion Assembly: A Functional Switch upon Loss of E-Cadherin.” *EMBO Journal* 27 (19): 2603–15.

Liang, Zheng-yun, Xing Kang, Hong Chen, Meng Wang, and Wen-xian Guan. 2017. “Effect of Clostridium Perfringens Enterotoxin on Gastric Cancer Cells SGC7901 Which Highly Expressed Claudin-4 Protein.” *World Journal of Gastrointestinal Oncology* 9 (4): 153.

Lopez, Theresa, and Douglas Hanahan. 2002. “Elevated Levels of IGF-1 Receptor Convey Invasive and Metastatic Capability in a Mouse Model of Pancreatic Islet Tumorigenesis.” *Cancer Cell* 1 (4): 339–53.

Lorentzen, A., J. Bamber, A. Sadok, I. Elson-Schwab, and C. J. Marshall. 2011. “An Ezrin-Rich, Rigid Uropod-like Structure Directs Movement of Amoeboid Blebbing Cells.” *Journal of Cell Science* 124 (8): 1256–67.

Lu, Pengfei, Valerie M. Weaver, and Zena Werb. 2012. “The Extracellular Matrix: A Dynamic Niche in Cancer Progression.” *Journal of Cell Biology* 196 (4): 395–406.

M

Markov, Alexander G., Jörg R. Aschenbach, and Salah Amasheh. 2015. “Claudin Clusters as Determinants of Epithelial Barrier Function.” *IUBMB Life* 67 (1): 29–35..

Mayor, Eric Theveneau, and Roberto. 2012. “Cadherins in Collective Cell Migration of Mesenchymal Cells.” *Current Opinion in Cell Biology* 24 (5): 677–84. https://doi.org/10.1016/j.ceb.2012.08.002.Cadherins.

Meacham, Corbin E., and Sean J. Morrison. 2013. “Tumour Heterogeneity and Cancer Cell Plasticity.” *Nature* 501 (7467): 328–37.

Mendel, Dirk B, A Douglas Laird, Xiaohua Xin, Sharianne G Louie, James G Christensen, Guangmin Li, Randall E Schreck, et al. 2003. “In Vivo Antitumor Activity of SU11248, a Novel Tyrosine Kinase Inhibitor Targeting Vascular Endothelial Growth Factor and Platelet-Derived Growth Factor Receptors.” *Clinical Cancer Research* 9 (1): 327–37.

Michl, Patrick, Malte Buchholz, Monika Rolke, Steffen Kunsch, Matthias Löhr, Bruce McClane, Shoichiro Tsukita, Gerhard Leder, Guido Adler, and Thomas M. Gress. 2001. “Claudin-4: A New Target for Pancreatic Cancer Treatment Using Clostridium Perfringens Enterotoxin.” *Gastroenterology* 121 (3): 678–84.

Missiaglia, Edoardo, Irene Dalai, Stefano Barbi, Stefania Beghelli, Massimo Falconi, Marco della Peruta, Lorenzo Piemonti, et al. 2009. “Pancreatic Endocrine Tumors: Expression Profiling Evidences a Role for AKT-MTOR Pathway.” *J Clin Oncol* 28 (2): 245–55.

N

Nichols, Lynette S., Raheela Ashfaq, and Christine A. Iacobuzio-Donahue. 2004. “Claudin 4 Protein Expression in Primary and Metastatic Pancreatic Cancer: Support for Use as a Therapeutic Target.” *American Journal of Clinical Pathology* 121 (2): 226–30.

O

O’Farrell, Anne Marie, Tinya J. Abrams, Helene A. Yuen, Theresa J. Ngai, Sharianne G. Louie, Kevin W H Yee, Lily M. Wong, et al. 2003. “SU11248 Is a Novel FLT3 Tyrosine Kinase Inhibitor with Potent Activity in Vitro and in Vivo.” *Blood* 101 (9): 3597–3605.

Osanai, Makoto, Akira Takasawa, Masaki Murata, and Norimasa Sawada. 2017. “Claudins in

Cancer: Bench to Bedside." *Pflugers Archiv European Journal of Physiology* 469 (1): 55–67.

P

Pàez-ribes, Marta, Elizabeth Allen, James Hudock, Takaaki Takeda, Francesc Viñals, Masahiro Inoue, Gabriele Bergers, and Douglas Hanahan. 2010. "To Increased Local Invasion and Distant Metastasis." *Response* 15 (3): 220–31.

Pennacchietti, Selma, Paolo Michieli, Maria Galluzzo, Massimiliano Mazzone, Silvia Giordano, and Paolo M. Comoglio. 2003. "Hypoxia Promotes Invasive Growth by Transcriptional Activation of the Met Protooncogene." *Cancer Cell* 3 (4): 347–61.

Pietras, Kristian, and Douglas Hanahan. 2005. "A Multitargeted, Metronomic, and Maximum-Tolerated Dose 'Chemo-Switch' Regimen Is Antiangiogenic, Producing Objective Responses and Survival Benefit in a Mouse Model of Cancer." *Journal of Clinical Oncology* 23 (5): 939–52.

Poincloux, Renaud, Olivier Collin, Floria Lizárraga, Maryse Romao, Marcel Debray, Matthieu Piel, and Philippe Chavrier. 2011. "Contractility of the Cell Rear Drives Invasion of Breast Tumor Cells in 3D Matrigel." *Proceedings of the National Academy of Sciences* 108 (5): 1943–48.

R

Raymond, Eric, Laetitia Dahan, Jean-Luc Raoul, Yung-Jue Bang, Ivan Borbath, Catherine Lombard-Bohas, Juan Valle, et al. 2011. "Sunitinib Malate for the Treatment of Pancreatic Neuroendocrine Tumors." *New England Journal of Medicine* 364 (6): 501–13.

Riffle, Stephen, and Rashmi S. Hegde. 2017. "Modeling Tumor Cell Adaptations to Hypoxia in Multicellular Tumor Spheroids." *Journal of Experimental and Clinical Cancer Research* 36 (1): 1–10.

Romanov, Victor, Terry C. Whyard, Wayne C. Waltzer, and Theodore G. Gabig. 2014. "A Claudin 3 and Claudin 4-Targeted Clostridium Perfringens Protoxin Is Selectively Cytotoxic to PSA-Producing Prostate Cancer Cells." *Cancer Letters* 351 (2): 260–64.

Rosenthal, Rita, Dorothee Günzel, Dian Theune, Carolina Czichos, Jörg Dieter Schulzke, and Michael Fromm. 2017. “Water Channels and Barriers Formed by Claudins.” *Annals of the New York Academy of Sciences* 1397 (1): 100–109.

S

Sabeh, Farideh, Ryoko Shimizu-Hirota, and Stephen J. Weiss. 2009. “Protease-Dependent versus-Independent Cancer Cell Invasion Programs: Three-Dimensional Amoeboid Movement Revisited.” *Journal of Cell Biology* 185 (1): 11–19.

Sadanandam, A., S. Wullschleger, C. A. Lyssiotis, C. Grotzinger, S. Barbi, S. Bersani, J. Korner, et al. 2015. “A Cross-Species Analysis in Pancreatic Neuroendocrine Tumors Reveals Molecular Subtypes with Distinctive Clinical, Metastatic, Developmental, and Metabolic Characteristics.” *Cancer Discovery* 5 (12): 1296–1313.

Sanz-Moreno, Victoria, and Christopher J. Marshall. 2010. “The Plasticity of Cytoskeletal Dynamics Underlying Neoplastic Cell Migration.” *Current Opinion in Cell Biology* 22 (5): 690–96.

Scarpa, Aldo, David K. Chang, Katia Nones, Vincenzo Corbo, Ann Marie Patch, Peter Bailey, Rita T. Lawlor, et al. 2017. “Whole-Genome Landscape of Pancreatic Neuroendocrine Tumours.” *Nature* 543 (7643): 65–71.

Shimada, Hiroshi, Seiro Satohisa, Takayuki Kohno, Takumi Konno, Ichi Ken-Takano, Syunta Takahashi, Tsubasa Hatakeyama, Chihiro Arimoto, Tsuyoshi Saito, and Takashi Kojima. 2017. “Downregulation of Lipolysis-Stimulated Lipoprotein Receptor Promotes Cell Invasion via Claudin-1-Mediated Matrix Metalloproteinases in Human Endometrial Cancer.” *Oncology Letters* 14 (6): 6776–82.

Smith, Ashley, Theodoros N. Teknos, and Quintin Pan. 2013. “Epithelial to Mesenchymal Transition in Head and Neck Squamous Cell Carcinoma.” *Oral Oncology* 49 (4): 287–92.

Smith, Bethany, and Neil Bhowmick. 2016. “Role of EMT in Metastasis and Therapy Resistance.” *Journal of Clinical Medicine* 5 (2): 17.

Stamatovic, Svetlana M., Allison M. Johnson, Nikola Sladojevic, Richard F. Keep, and Anuska V. Andjelkovic. 2017. “Endocytosis of Tight Junction Proteins and the Regulation of Degradation and Recycling.” *Annals of the New York Academy of Sciences* 1397 (1): 54–65.

T

Tabariès, S., and P. M. Siegel. 2017. “The Role of Claudins in Cancer Metastasis.” *Oncogene* 36 (9): 1176–90.

Talkenberger, Katrin, Elisabetta Ada Cavalcanti-Adam, Anja Voss-Böhme, and Andreas Deutsch. 2017. “Amoeboid-Mesenchymal Migration Plasticity Promotes Invasion Only in Complex Heterogeneous Microenvironments.” *Scientific Reports* 7 (1): 1–12.

Tamura, Atsushi, and Sachiko Tsukita. 2014. “Paracellular Barrier and Channel Functions of TJ Claudins in Organizing Biological Systems: Advances in the Field of Barriology Revealed in Knockout Mice.” *Seminars in Cell and Developmental Biology* 36: 177–85.

Ter-Minassian, Monica, Jennifer A. Chan, Susanne M. Hooshmand, Lauren K. Brais, Anastassia Daskalova, Rachel Heafield, Laurie Buchanan, et al. 2013. “Clinical Presentation, Recurrence, and Survival in Patients with Neuroendocrine Tumors: Results from a Prospective Institutional Database.” *Endocrine-Related Cancer* 20 (2): 187–96.

V

Valastyan & Weinberg. 2011. “Tumor Metastasis: Molecular Insights and Evolving Paradigms.” *Cell*.

W

Wang, Xiaoze, Atsushi Enomoto, Naoya Asai, Takuya Kato, and Masahide Takahashi. 2016. “Collective Invasion of Cancer: Perspectives from Pathology and Development.” *Pathology International* 66 (4): 183–92.

Y

Yamaguchi, Naoya, Takeomi Mizutani, Kazushige Kawabata, and Hisashi Haga. 2015. “Leader Cells Regulate Collective Cell Migration via Rac Activation in the Downstream Signaling of Integrin B1 and PI3K.” *Scientific Reports* 5: 1–8.

Yao, James C., Manal Hassan, Alexandria Phan, Cecile Dagohoy, Colleen Leary, Jeannette E. Mares, Eddie K. Abdalla, et al. 2008. “One Hundred Years after ‘Carcinoid’: Epidemiology of and Prognostic Factors for Neuroendocrine Tumors in 35,825 Cases in the United States.” *Journal of Clinical Oncology* 26 (18): 3063–72.

Z

Zeisberg, Michael, and Eric G. Neilson. 2009. “Biomarkers for Epithelial-Mesenchymal Transitions.” *Journal of Clinical Investigation* 119 (6): 1429–37.

Zuazo-Gaztelu, Iratxe, and Oriol Casanovas. 2018. “Unraveling the Role of Angiogenesis in Cancer Ecosystems.” *Frontiers in Oncology* 8 (July): 1–13.